University of Bremen

Deutsches Zentrum für Luft- und Raumfahrt
German Aerospace Center

Hilmi Dogu Kücüker

Design and Simulation of an Attitude Control System for a Microsatellite

Master Thesis

to achieve the university degree of

Master of Science

Master's degree programme: Space Sciences and Technologies

submitted to

University of Bremen

Supervisor: Dr. Stephan Theil

Evaluator: Prof. Dr. Meike List

DLR Institute of Space Systems

Bremen, February 2024

Abstract

This thesis offers an open-source alternative tool for the implementation and assessment of various attitude control systems for microsatellites. *Spacecraft GNC Toolbox*, a software toolbox written in Scilab environment was created for that purpose. The toolbox provides an Application Programming Interface (API) and simulation block palette to be used in Xcos environment. Spacecraft dynamics, sensors, actuators, external disturbances, and controllers were modeled as Xcos blocks and their source code was written in Scilab from the ground up. Owing to the fact that Scilab provides an interface for code blocks in Fortran and C languages, the source code of environmental models could be conveniently imported into the toolbox. The disturbance analysis was carried out to estimate the worst environmental conditions for the Attitude and Orbital Control System (AOCS). Attitude control modes were determined according to the reference mission requirements. Considering control modes and disturbance analysis results, adequate sensors (Gyroscope, magnetometer, and star tracker) and actuators (reaction wheels and magnetorquers) for AOCS were selected. Quaternion-based attitude controllers were developed using Linear Quadratic Regulator (LQR) technique and its integral controller augmented form. The robustness of these controllers was examined with Monte-Carlo simulations and worst-case analyses. After obtaining the robust controllers, mode transition scenarios were conducted, in order to deduce whether the designed controllers were practical and accurate. In the end, *Spacecraft GNC Toolbox*, which was developed in Scilab/Xcos environment, was proven to be sufficient for AOCS design since it allows engineers to develop controllers from the ground up and evaluate them.

Contents

List of Figures

List of Tables

Acronyms

ACS Attitude Control System.
AMR Anisotropic Magnetoresistive.
AOCS Attitude and Orbital Control System.

BCRS Barycentric Celestial Reference System.
BF Body Frame.

CAM Coarse Acquisition Mode.
CCMC NASA Community Coordinated Modeling Center.
CMOS Complementary Metal-Oxide Semiconductor.

DCM Direction Cosine Matrix.
DTM De-Tumbling Mode.
DTM2013 Drag Temperature Model 2013.

ECF Earth Centered Fixed Frame.
ECI Earth Centered Inertial Frame.
ECSS European Cooperation for Space Standardization.

FAM Fine Acquisition Mode.

GCRS Geocentric Celestial Reference System.
GMAT General Mission Analysis Tool.
GNC Guidance Navigation and Control.

IAU International Astonomical Union.
ICRF Inertial Celestial Reference Frame.
ICRS Inertial Celestial Reference System.
IGRF The International Geomagnetic Reference Field.
INIT Initialization Mode.
IPM Inertial Pointing Mode.

JB2008 Jacchia-Bowman 2008.
JGM-2 Joint Gravity Model-2.

LQI Linear Quadratic Integral Compensator.
LQR Linear Quadratic Regulator.
LTAN Local Time of the Ascending Node.
LTI Linear Time Invariant.
LVLH Local Vertical Local Horizontal Frame.

NASA National Aeronautics and Space Act.
NRLMSISE-00 US Naval Research Laboratory Mass Spectrometer and Incoherent Scatter Radar 2000.

OBC On-Board Computer.

PVT Position Velocity and Time.

RAAN Right Ascension of the Ascending Node.

SAFE Safe Mode.
SCAN Scan Mode.
SUSP Suspend Mode.

TAI International Atomic Time.
TCB Barycentric Coordinate Time.
TCG Geocentric Coordinate Time.
TT Terrestrial Time.

US76 US Standard Atmosphere 1976.
UTC Universal Time Coordinated.

VLBI Very Long Baseline Interferometry.

1. Introduction

1.1. Prologue

During the Cold War era, there was a space race between the U.S. and the Soviet Union. After the Soviets sent the first astronaut (Yuri Gagarin) and the first satellite (Sputnik-1) to the space and National Aeronautics and Space Administration (NASA) successfully operated Human Landing on the Moon in 1969 space agencies gained more public interest [1]. Space agencies started to develop and enhance their space vehicles at their own best until the co-assembling International Space Station in 1993. Then, the space race became the "race with collaboration" [2].

In the 1990s, semi-automatic and robotic space missions have become more common and developments in space technology were channeled towards those fields. Especially after navigation satellites became public and sending the first CubeSats paved the way for enhancements of satellite technology. As of 17th January 2024, there are 17483 artificial space objects orbiting around the Earth [3].

The developments in semi-automatic and robotic missions increased the need for attitude and orbital control systems (AOCS) because, in current technology, onboard operation of attitude stabilization and maneuvers is a more efficient method than operating them from Ground Station. Advances in computation technologies, sensor fusion, and control algorithms enabled engineers and scientists to implement more accurate and complex observation and control strategies for a satellite.

As of January 2024, satellite attitude control systems may be simulated via the most common writing software blocks, like Fortran, C/C++, Python, and so on. In the 1980s, Matlab, a programming and numeric computation environment was developed, which could interactively solve Ordinary Differential Equations and Control Systems [4]. Simulink, which is a model-based dynamics simulation environment tool, was developed for Matlab, in order to have a more intuitive approach to dynamics systems design. Matlab/Simulink is widely used in satellite attitude dynamics simulations. At the beginning of the 1990s, developers of the French National Institute for Research in Digital Science and Technology (INRIA) devised an open-source numeric computation and programming environment, Scilab [5]. Then, Xcos, which corresponds to Simulink in Matlab, was developed as a tool for Scilab.

1.2. Motivation

Today's most numeric computation software tools are not open source and profit-oriented. Therefore, most of their source codes are not published and the development line of source codes is limited to a certain community. Considering today's exponentially growing space community, the need for an open-source software tool for space systems and subsystems has arisen. At this time, in this thesis work, the attitude control system development in Scilab was considered as a starting point.

The main objective of this thesis work is to investigate to which extent and how accurate an attitude control system for a satellite, with predefined mission constraints, could be developed in Scilab framework. For that purpose, *Spacecraft GNC Toolbox* for Xcos platform was created, which contains simulation blocks for the satellite attitude control system. Blocks of the toolbox mainly model satellite attitude dynamics, hardware, and external disturbances on attitude dynamics. This thesis work will explain the development process of these blocks thoroughly.

The second aim of the thesis is to implement and test an attitude control system, which will be ready for further AOCS design phases. A representative reference mission was provided for this thesis work. Considering the reference mission requirements, controller modes and their transitions were designated, in order to construct a state machine inside AOCS, which provides autonomy to the system. Designed controllers and their autonomy will be extensively examined in the thesis work.

1.3. Structure

In order to accomplish objectives given in Section 1.2, this thesis work falls into five chapters and the appendix section. As a brief notation, they are:

- **Chapter 2** explains all the terminologies used in the design and evaluation of an ACS.
- **Chapter 3** describes the methodology employed in the software development of Scilab/Xcos blocks to be used in ACS.
- **Chapter 4** aims for the selection of adequate hardware for ACS. This chapter explains the selection process from the ground up. Starting from the reference mission description, this chapter verifies the generated orbital parameters in Scilab environment, defines controller modes accordingly, performs a disturbance analysis, and then makes the hardware selection.
- **Chapter 5** expresses the development process behind attitude controllers for all modes defined in Chapter 4. The test methodology of these controllers is described there as well.
- **Chapter 6** comments on the results of the thesis work, investigates whether the results meet the thesis objectives, and makes a conclusion to it.
- **Appendix** contains the solar cycle graph, *Spacecraft GNC Toolbox* blocks on Xcos palette, additional plots obtained from the controller development phase, and Xcos simulation diagrams.

2. Background

2.1. Coordinate Frames and Time Scales

In physics, reference frames are used for explaining laws of motion. There are two types of reference frames: Inertial and non-inertial. Inertial reference frames are reference frames, that comply with Newton's first law of motion, which states: "*Every particle continues in its state of rest or uniform motion in a straight line relative to an inertial reference frame, unless it is compelled to change that state by forces acting upon it*" [6]. In other words, the magnitude and the direction of the motion of the inertial reference frame should not change. According to Einstein's Equivalence Principle, all physical laws have the same form in inertial reference frames [7].

International Astonomical Union (IAU) is an international organization that defines universal reference systems, which constitute Inertial reference frames. Examples of inertial reference frames are the Geocentric Celestial Reference System (GCRS) and the Barycentric Reference System (BCRS). While BCRS has the origin at Solar System Barycenter, GCRS has the origin at Earth's center of gravity [8]. They are both bound to the same general relativity framework with specified metric tensors and have the same orientation. For practical purposes, the International Celestial Reference System (ICRS) is defined, which is identical to BCRS [8].

As for time scales, BCRS comes with Barycentric Coordinate Time (TCB) and GCRS comes with Geocentric Coordinate Time (TCG). International Atomic Time (TAI) is the time scale that originated from Cesium 133 transition measurements taken from various regions on Earth [8]. Other time scales are using Earth rotation, which is subject to perturbations over time. Therefore the Earth's rotation is continuously observed by Very Long Baseline Interferometry (VLBI) [8]. Since TCG runs slightly faster than SI seconds on Earth's surface, Terrestrial Time (TT) was designated in order to have a clock running at the same rate [8]. TT is 32.184 seconds ahead of TAI [8]. For the convenience for astronomers and scientists, a time epoch named *J2000* was designated, which is equal to January 1 2000 11:58:55.816 UTC+0 and 2451545.0 TT [9].

2.1.1. Earth Centered Inertial Frame

ICRS lies on the true celestial equator and one celestial pole on *J2000* epoch, given through Earth precession and nutation models, with respect to the galaxies [10]. ICRF is a realization of ICRS. *J2000* or *MJ2000* (Mean J2000) defines an inertial reference frame, which has the angular distance of 0.1″ from ICRF [11]. ECI is the Earth centered *J2000* frame, as shown in Figure 2.1. The X axis points towards *vernal equinox*, which is the direction from the center of Earth towards the Sun on the first day of spring. The Z axis is the North Celestial Pole, which is deviated 1 deg from the Pole Star, Polaris, and the Y axis is the orthogonal complementary of above-defined X and Y axes [12]. For astronomical purposes, any stars or galaxies are shown in *J2000* frame by azimuthal Right Ascension and elevational Declination angles from the Celestial Equatorial Plane, making the slant range component excluded due to infinitesimal distance of those space objects. In this thesis work, ECI is useful in defining Earth satellite orbits because those types of orbits are independent of Earth rotation and any other acceleration and it enables us to have Cartesian coordinates for each given timestamp.

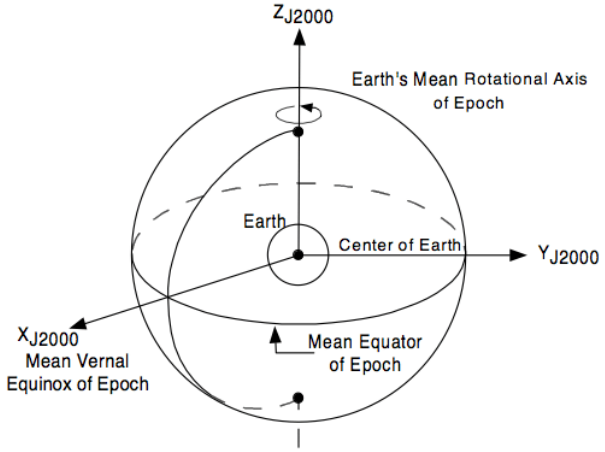

Source: researchgate.net

Figure 2.1.: Earth Centered Inertial Frame

2.1.2. Local Vertical Local Horizontal Frame

When a coordinate system with one of its axes pointing towards Earth's center of gravity (Nadir), the other one showing the velocity vector LVLH frame is used. According to the frame definition, the Y-axis is the negative orbital angular momentum vector, the Z-axis is the Nadir vector, and the X-axis is the right-hand orthogonal complement of the Y and Z axes. When the satellite has a circular orbit, the X-axis becomes the tangent vector. In this thesis work, this frame is used for Nadir and Zenith pointing mode controllers defined for AOCS.

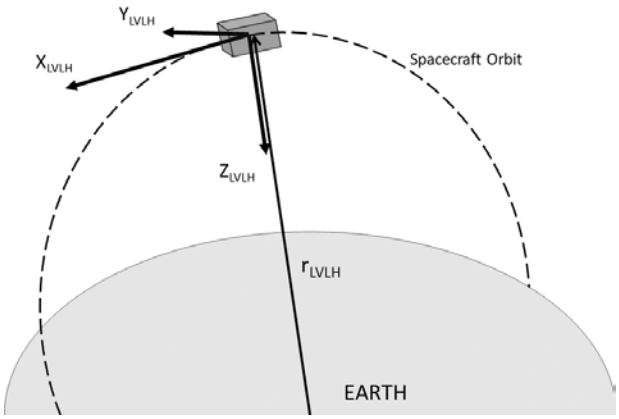

Source: Biose et. al, 2017

Figure 2.2.: LVLH Frame

2.1.3. Satellite Body Frame

The satellite body frame is a frame fixed in the spacecraft. Body frames are used in expressing physical laws of motion with respect to the satellite structure and AOCS hardware [12]. In general, the origin of the Body Frame is selected as the center of gravity of the satellite. The X, Y, and Z axes can be selected arbitrarily. However, they are selected regarding mission requirements and payload activities. In this thesis work, the body frame definition is given in Section 4.1.

2.2. Orbital Mechanics

According to Kepler Laws of orbital motion, the orbital motion equation is given in Equation 2.1, where r is the distance from the focal point, h is the magnitude of angular momentum, μ is the Earth gravitational constant, e and θ are the eccentricity and true anomaly, respectively, that will be explained in detail [13].

$$r = \frac{h^2}{\mu} \frac{1}{1 + e\cos\theta} \tag{2.1}$$

According to Curtis [13], Keplerian and their derived elements can be calculated by using Equation 2.1, which are given below:

Perigee: The point on the orbit having the minimum distance to the Earth. On Figure 2.3, it can be shown as $r_P = |EP|$.

Apogee: The point on the orbit having the maximum distance to the Earth. On Figure 2.3, it can be shown as $r_A = |AE|$.

Semi-major axis: The point on the orbit having the maximum distance with the orbital center point. It can be found in Equation 2.2.

$$a = \frac{r_A + r_P}{2} \tag{2.2}$$

Eccentricity: The ratio for definition and parametrization of conic sections. Equation 2.3 gives the eccentricity of the orbit. If e equals to zero, that means the current trajectory (conic) that the satellite follows, is the perfect circular orbit. When the eccentricity is in between 0 and 1, the conic is defined as an elliptical orbit. When it gets higher than or equal to 1, the conic does not constitute an orbit (parabola and hyperbola).

$$e = \frac{r_A - r_P}{r_A + r_P} \tag{2.3}$$

True anomaly: The angle measured at the Earth between the perigee passage and the current position of the satellite. On Figure 2.3, it can be shown as θ.

Eccentric anomaly: The angle measured at the orbit center between perigee passage and the projection of the satellite positon to a virtual circular orbit. On Figure 2.3, it can be pointed out as E. It can be derived from true anomaly with Equation 2.4.

$$\tan\left(\frac{E}{2}\right) = \tan\left(\frac{\theta}{2}\right)\sqrt{\frac{1-e}{1+e}} \tag{2.4}$$

Mean anomaly: Dividing the time since perigee passage to the orbital period and converting the result to radians or degrees give the mean anomaly. It may be derived from eccentric anomaly with Equation 2.5.

$$M = E - e \sin E \tag{2.5}$$

Inclination: The angle between the orbital and reference plane. It is shown as i on Figure 2.4, when the Earth's equatorial plane is shown as gray plane, whereas the orbital plane is yellow.

Ascending node: The point on the satellite orbit around the Earth, where the satellite orbits from south to the north side of the equatorial plane.

Right Ascension of the Ascending Node (RAAN): The angle at the Earth from Vernal Equinox vector to the ascending node eastward, when the ECI is taken as the frame of reference. On Figure 2.4, it is pointed out as Ω.

Argument of perigee: The angle at the Earth from ascending node to perigee vector with the direction of satellite motion. On Figure 2.4, it is defined as ω.

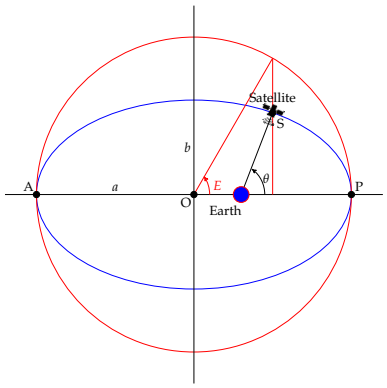

Source: Satellite Icon: flaticon.com

Figure 2.3.: Orbital plane representation

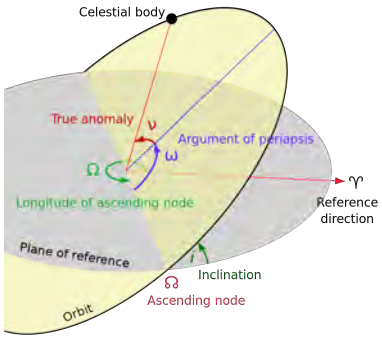

Source: en.wikipedia.com

Figure 2.4.: Orbital parameters in three dimensions

2.2.1. J_2 Perturbation

According to Wertz [12], if a satellite has an altitude of several hundreds of kilometers, the major source of orbital perturbation is sourced from having an oblate spheroid shape causing non-homogeneous (non-spherical) mass distribution of Earth. By intuition, due to being conservative of gravitational force, the total energy, mean semi-major axis and eccentricity of the satellite orbit do not change with the oblateness of Earth. However, due to the secular variations, the average of other orbital parameters grows monotonically [12].

As an analytical solution, the zonal variation of Earth's gravitational force is modeled as Φ in Equation 2.6. Then, Φ is written as an infinite series given in Equation 2.7, where r is the distance from the center of Earth, μ is the Earth gravitational constant, ϕ is the polar angle from $+Z$ axis to the radial, J_k are the zonal harmonics of the Earth, R is the Earth equatorial radius, and P_k are Legendre Polynomials. It is observed from Earth zonal harmonics that the second harmonic (J_2) is the dominant harmonic with respect to the others. Therefore, Equation 2.7 simplifies to Equation 2.8 [14].

$$V(r,\phi) = -\frac{\mu}{r} + \Phi(r,\phi) \tag{2.6}$$

$$\Phi(r,\phi) = \frac{\mu}{r}\sum_{k=2}^{\infty} J_k \left(\frac{R}{r}\right)^k P_k \cos\phi \tag{2.7}$$

$$\Phi(r,\phi) = \frac{J_2}{2}\frac{\mu}{r}\left(\frac{R}{r}\right)^2 (3\cos^2\phi - 1) \tag{2.8}$$

Gauss planetary equations are a set of equations that give the time derivative of six Keplerian parameters of any given orbit when the force of the perturbation source is known [14]. After achieving the force model from Equation 2.8, the time change of average osculating Keplerian elements are given below [14].

$$\frac{d\overline{a}}{dt} = 0 \tag{2.9}$$

$$\frac{d\overline{e}}{dt} = 0 \tag{2.10}$$

$$\frac{d\overline{i}}{dt} = 0 \tag{2.11}$$

$$\frac{d\overline{\Omega}}{dt} = -\left(\frac{3}{2}\frac{J_2\sqrt{\mu}R^2}{a^{7/2}(1-e^2)^2}\right)\cos i \tag{2.12}$$

$$\frac{d\overline{\omega}}{dt} = -\left(\frac{3}{2}\frac{J_2\sqrt{\mu}R^2}{a^{7/2}(1-e^2)^2}\right)\left(\frac{5}{2}\sin^2 i - 2\right) \tag{2.13}$$

$$\frac{d\overline{\theta}}{dt} = \sqrt{\frac{\mu}{a^3}} - \left(\frac{3}{2}\frac{J_2\sqrt{\mu}R^2}{a^{7/2}(1-e^2)^2}\right)\left(1 - \frac{3}{2}\sin^2 i\right) \tag{2.14}$$

2.2.2. Sun-Synchronous Orbits

In Equation 2.12, when semi-major axis, eccentricity, and the inclination of the orbit are adjusted so that the rate of RAAN equals to one rotation per year (0.9856 deg/day), the orbit is defined as Sun-Synchronous Orbit since the orbit stays the same with respect to the Sun, as Earth orbits around it [12]. This is advantageous for satellites surveying the Earth's surface or tracking surface changes, which requires constant illumination on pre-defined specific portion of the Earth's surface at the same local time over a given latitude [12].

Hour Angle is the angular difference between the celestial meridian of the observer and the object westwards [12]. Since Earth completes its rotation in 24 h, 15 deg hour angle means 1 hour in time. The local hour angle of the Sun is called apparent solar time, which adds 12 hours more [12]. Due to the variations in Earth's rotational and translational speed with respect to the Sun, the length of Solar day is not constant [12]. In order to ease the usage of Solar time, the mean Sun, an artificial point moving along Earth's equator with a constant rate, was defined. Mean Solar time or Local Mean Time is the hour angle value of the mean Sun [12]. *Local Time of Ascending Node* (LTAN) is the mean Solar time of the ascending node of the satellite orbit, which is supposed to be constant at Sun-Synchronous Orbits [15].

2.3. Rotational Kinematics

The orientation of one frame with respect to another may be represented in four ways: Direction Cosine Matrix, Euler Angles, Quaternions, and Rodrigues Parameters. In the thesis work, quaternions are the most common method for the representation because:

- Direction Cosine Matrices (DCM) consists of nine parameters for the representation and in time, numeric errors accumulate with every multiplication operation. In this thesis work, they will be used as an intermediate step to achieve orbital frame conversions.
- Euler Angles are intuitive and therefore, they might be used for visualization purposes. Nevertheless, it has singularities for large angle rotations, which might be quite detrimental for the simulation [16].
- Quaternions require only four parameters. It is not intuitive like Euler angles. However, it is the common method for computations.
- Modified Rodrigues Parameters require one less parameter from quaternions but it is not widespread like quaternions and it has not yet been introduced in CelestLab.

2.3.1. Direction Cosine Matrix

A and B are reference frames consisting of right hand set of three orthogonal vectors $\{\vec{a_1}, \vec{a_2}, \vec{a_3}\}$ and $\{\vec{b_1}, \vec{b_2}, \vec{b_3}\}$, respectively. Every $\vec{b_i}$ can be written as a linear combination of $\vec{a_j}$, which is shown in Equation 2.15. In this equation, C_{ij} are the direction cosines giving $\vec{b_i} \cdot \vec{a_j}$ and $C^{B/A}$ is the DCM, which will be called as from A to B coordinate transformation or rotation matrix in following sections and chapters [17].

$$\begin{bmatrix} \vec{b_1} \\ \vec{b_2} \\ \vec{b_3} \end{bmatrix} = \begin{bmatrix} C_{11} & C_{12} & C_{13} \\ C_{21} & C_{22} & C_{23} \\ C_{31} & C_{32} & C_{33} \end{bmatrix} \begin{bmatrix} \vec{a_1} \\ \vec{a_2} \\ \vec{a_3} \end{bmatrix} = C^{B/A} \begin{bmatrix} \vec{a_1} \\ \vec{a_2} \\ \vec{a_3} \end{bmatrix} \tag{2.15}$$

2.3.2. Quaternions

According to *Euler's Eigenaxis Rotation Theorem*, the orientation of a frame related to another can be changed by rotating the frame around inertial frame [17]. If the axis of rotation remains unchanged for both frames, this is called Euler axis [17]. That means every combination of the set of rotations can be expressed as a single rotation axis and

the angle of rotation (θ) in overall, like Equation 2.16 [17].

$$\mathbf{e} = \begin{bmatrix} e_1 \\ e_2 \\ e_3 \end{bmatrix} = \frac{1}{2\sin\theta} \begin{bmatrix} C_{23} - C_{32} \\ C_{31} - C_{13} \\ C_{12} - C_{21} \end{bmatrix}, \; e_1^2 + e_2^2 + e_3^2 = 1 \tag{2.16}$$

Without loss of generality, four Euler parameters are defined, like in Equations 2.17a-2.17d. Later on, those Euler parameters are called quaternions.

$$q_1 = \cos\left(\frac{\theta}{2}\right) \tag{2.17a}$$

$$q_2 = e_1 \sin\left(\frac{\theta}{2}\right) \tag{2.17b}$$

$$q_3 = e_2 \sin\left(\frac{\theta}{2}\right) \tag{2.17c}$$

$$q_4 = e_3 \sin\left(\frac{\theta}{2}\right) \tag{2.17d}$$

The time derivative of quaternions can be expressed in Equation 2.18 and 2.19 [17].

$$\begin{bmatrix} \dot{q_1} \\ \dot{q_2} \\ \dot{q_3} \\ \dot{q_4} \end{bmatrix} = \frac{1}{2} \begin{bmatrix} q_1 & -q_2 & -q_3 & -q_4 \\ q_2 & q_1 & -q_4 & q_3 \\ q_3 & q_4 & q_1 & -q_2 \\ q_4 & -q_3 & q_2 & q_1 \end{bmatrix} \begin{bmatrix} 0 \\ \omega_1 \\ \omega_2 \\ \omega_3 \end{bmatrix} \tag{2.18}$$

$$\dot{\boldsymbol{q}^B} = \frac{1}{2}\boldsymbol{q^B} * \boldsymbol{w^B} \tag{2.19}$$

2.3.3. Temporal Changes in Rotating Frames

$\boldsymbol{\omega}$ is the angular velocity vector of the body frame with respect to the inertial frame and $\boldsymbol{e}$ is an arbitrary unit vector fixed in the Body Frame. The vector $\boldsymbol{V}$ is defined, whcih is fixed to the body frame, as a linear combination of arbitrary $\boldsymbol{e_1}$, $\boldsymbol{e_2}$, and $\boldsymbol{e_3}$ vectors [18]. Then:

$$\frac{d\boldsymbol{e}}{dt} = \boldsymbol{\omega} \times \boldsymbol{e} \tag{2.20}$$

$$\boldsymbol{V} = V_1\boldsymbol{e_1} + V_2\boldsymbol{e_2} + V_3\boldsymbol{e_3} = \sum_{i=1}^{3} V_i\boldsymbol{e_i} \tag{2.21}$$

$$\frac{d\boldsymbol{V}}{dt} = \sum_{i=1}^{3} \frac{dV_i}{dt}\boldsymbol{e_i} + \sum_{i=1}^{3} V_i\frac{d\boldsymbol{e_i}}{dt} \tag{2.22}$$

Since $\boldsymbol{e_i}$ vectors are attached to the body frame, the left summation in Equation 2.22 gives the time derivative of the vector with respect to the body frame. Applying Equation 2.20 to the latter summation of Equation 2.22 gives the cross product of $\boldsymbol{\omega}$ and $\boldsymbol{V}$.

The relation between changes in the vector related to inertial and body frame can be explained in Equation 2.23 [18].

$$\left(\frac{d\boldsymbol{V}}{dt}\right)_I = \left(\frac{d\boldsymbol{V}}{dt}\right)_B + \boldsymbol{\omega} \times \boldsymbol{V} \tag{2.23}$$

2.4. Control Systems

In this thesis work, an attitude control system will be implemented in Scilab and several control methods will be applied in Chapter 5. At first glance, it is evident that the dynamics of the attitude control system are nonlinear since the state transitions contain angular variables and functions, which are nonlinear and may contain singularities. Solving nonlinear systems requires the utilization of complex functions and optimization methods, which do not apply to onboard software. Therefore, after verification of controllability, the theoretical deduction to linearization and stability analysis of the system will be conducted. At the end of this section, Linear Quadratic Regulator (LQR) controller is to be briefly discussed.

2.4.1. Linear Time Invariant Systems and Controllability

Linear Time Invariant (LTI) system state space representation is given in Equation 2.24, where $\boldsymbol{x}$ is the state vector, $\boldsymbol{u}$ is the input vector, A is the system matrix, and B is the input matrix. Wie states that the system is controllable if from any state to any state change is possible through inputs [17]. Mathematically, the system in Equation 2.24 is called controllable if it satisfies Equation 2.25, where n is the number of rows of B matrix [17].

$$\dot{\boldsymbol{x}} = A\boldsymbol{x} + B\boldsymbol{u} \tag{2.24}$$

$$n = rank(\begin{bmatrix}\begin{bmatrix}B & AB & A^2B & ... & A^{n-1}B\end{bmatrix}\end{bmatrix}) \tag{2.25}$$

2.4.2. Stability

According to Wie [17], a nonlinear system is defined in Equation 2.26 and its equilibrium point is the point, where the system propagates zero state change for all of its states, as in Equation 2.27. If this system has a bounded state vector, all of its states approaching the equilibrium point are also bounded, like Equation 2.28, the system is defined as Lyapunov stable. If the system is Lyapunov stable and every possible initial condition results in reaching the equilibrium point, as in Equation 2.29, the system is called globally asymptotically stable [17].

$$\dot{\boldsymbol{x}} = \boldsymbol{f}(\boldsymbol{x}, t) \tag{2.26}$$

$$\boldsymbol{f}(\boldsymbol{x}^*, t) = 0 \tag{2.27}$$

$$\delta \geq \|\boldsymbol{x}(t_0) - \boldsymbol{x}^*\| \rightarrow \epsilon \geq \|\boldsymbol{x}(t) - \boldsymbol{x}^*\|, \forall t \geq t_0 \text{ and } \delta, \epsilon > 0 \tag{2.28}$$

$$\delta \geq \|\boldsymbol{x}(t_0) - \boldsymbol{x}^*\| \rightarrow \lim_{t\to\infty} \boldsymbol{x}(t) = \boldsymbol{x}^*, \forall \boldsymbol{x}(t_0) \tag{2.29}$$

If the perturbation $\boldsymbol{z}$ was introduced to $\boldsymbol{x}$, like in Equation 2.30, the transformation in Equation 2.31 might be made. If $\boldsymbol{z}$ is assumed to be small enough, the linearization with

Jacobian matrix in Equation 2.32 becomes possible [17].

$$\boldsymbol{x} = \boldsymbol{x}^* + \boldsymbol{z} \tag{2.30}$$
$$\dot{\boldsymbol{z}} = \boldsymbol{f}(\boldsymbol{x}^* + \boldsymbol{z}, t) \tag{2.31}$$
$$\dot{\boldsymbol{z}} = \left(\frac{\partial \boldsymbol{f}}{\partial \boldsymbol{x}}\right)_{\boldsymbol{x}^*} \boldsymbol{z} = A\boldsymbol{z} \tag{2.32}$$

After the linearization in Equation 2.32, the stability analysis can be made by only analyzing the eigenvalues of the linearized system matrix A. If the real part of all eigenvalues is negative, the system is to be declared asymptotically stable. Lyapunov stability for such a system means having eigenvalues with non-positive real parts and non-repetitive imaginary parts [17].

2.4.3. Linear Quadratic Regulator

Wise and Lavretsky express that Linear Quadratic Regulator (LQR) is a commonly used control design method in aerospace because it has excellent performance, robustness, and the minimize control usage [19]. Considering LTI system in Equation 2.33, the infinite time LQR problem formulation is given in Equation 2.34, where J is named as the cost function or quadratic performance index. Q and R are state and output cost weighting matrices; they are positive semi-definite and positive definite, respectively. It should be noted that (A, B) pair should be controllable, at least detectable and $(A, Q^{1/2})$ should be observable, at least detectable, in order for LQR algorithm to operate properly [19].

$$\dot{\boldsymbol{x}} = A\boldsymbol{x} + B\boldsymbol{u} \tag{2.33}$$
$$J = \int_0^\infty \left(\boldsymbol{x}^T Q \boldsymbol{x} + \boldsymbol{u}^T R \boldsymbol{u}\right) dt \tag{2.34}$$
$$\tag{2.35}$$

In this method, engineers try to find Q and R matrices giving the least value of J, by trial-and-error process. After that, P matrix in Equation 2.36 has to be found to achieve the optimal control feedback gain matrix, K in Equation 2.37. As a result, Equation 2.33 becomes Equation 2.38.

$$0 = PA + A^T P + PBR^{-1}B^T P + Q \tag{2.36}$$
$$\boldsymbol{u} = -R^{-1}B^T P\boldsymbol{x} = -K\boldsymbol{x} \tag{2.37}$$
$$\dot{\boldsymbol{x}} = (A - BK)\,\boldsymbol{x} \tag{2.38}$$

2.4.4. Linear Quadratic Regulator with Integral Action

According to Jaen et.al. [20], although LQR controllers offer an optimal response at the output, it does not guarantee the elimination of zero order steady-state error. Thus, introducing integral action to LQR controller will help remove the zero-order errors due to step references and disturbances [20]. Then, Equation 2.38 becomes 2.39, where $\boldsymbol{v}$ is the time integral of $\boldsymbol{x}$, K_i is the integral gain, and K_{LQR} is the gain matrix calculated in LQR method.

$$\dot{\boldsymbol{x}} = \left(A - BK_{LQR}\right)\boldsymbol{x} + K_i\boldsymbol{v} \tag{2.39}$$

3. Modeling

This chapter is dedicated to the modeling process of spacecraft attitude dynamics, hardware, and external disturbances as Scilab/Xcos simulation blocks under *Spacecraft GNC Toolbox*. The software development of the toolbox blocks was performed with the API of Scicos, which is the predecessor of Xcos discontinued in 2016 [21]. The Xcos palette view of the toolbox is shown in Figure A.2.

Scicos simulation blocks might be implemented by writing interface and computational files to each of them in Scilab language [22]. In the interface file, input-output vectors/-matrices, state variables, and parameters of a Scicos block are declared and the block activation source is set [22]. The output and state vectors' computation time might depend on external event trigger input or being "always active", in which the Scilab block generates its own calculation requests when needed [22]. Scilab blocks compute their state vector transitions or output vectors in computational files. Computational files could be written in Scilab, C, and Fortran languages [22]. As a notice, this thesis work ensures the consistency of *Spacecraft GNC Toolbox* until February 2024. Since the toolbox is open source, these blocks are open for development and their properties are changeable.

3.1. Rigid Body

In the context of the thesis work, the satellite is to be modeled as a pure rigid body. In other words, the elasticity of materials and the structure, slosh movement due to the liquid content in thrusters are ignored. According to Hughes [23], enables at most six degrees of freedom for attitude computations.

The angular momentum of the rigid body rotating around a fixed point is given in Equation 3.1. After the utilization of three-dimensional Cartesian coordinates into Equation 3.1, Equations 3.2a-3.2f are achieved, where I is the moment of inertia tensor of the body. Then, Equation 3.1 becomes 3.4 [24].

$$\boldsymbol{H} = \int [\boldsymbol{r} \times (\boldsymbol{\omega} \times \boldsymbol{r})]\, dm \tag{3.1}$$

$$I_{xx} = \int \left(y^2 + z^2\right) dm \tag{3.2a}$$

$$I_{yy} = \int \left(x^2 + z^2\right) dm \tag{3.2b}$$

$$I_{zz} = \int \left(x^2 + y^2\right) dm \tag{3.2c}$$

$$I_{xy} = I_{yx} = \int xydm \tag{3.2d}$$

$$I_{xz} = I_{zx} = \int xzdm \tag{3.2e}$$

$$I_{yz} = I_{zy} = \int yzdm \tag{3.2f}$$

$$\begin{bmatrix} H_x \\ H_y \\ H_z \end{bmatrix} = \begin{bmatrix} I_{xx} & -I_{xy} & -I_{xz} \\ -I_{xy} & I_{yy} & -I_{yz} \\ -I_{xz} & -I_{yz} & I_{zz} \end{bmatrix} \begin{bmatrix} \omega_x \\ \omega_y \\ \omega_z \end{bmatrix} \tag{3.3}$$

$$\boldsymbol{H} = I\boldsymbol{\omega} \tag{3.4}$$

$\boldsymbol{V}$ in Equation 2.23 is to be replaced with the angular momentum vector of the satellite rigid body, $\boldsymbol{H}$. The resultant equation, given below as Equation 3.5, is called Euler's equation [17].

$$\left(\frac{d\boldsymbol{H}}{dt}\right)_I = \left(\frac{d\boldsymbol{H}}{dt}\right)_B + \boldsymbol{\omega^B} \times \boldsymbol{H^B_{tot}} \tag{3.5}$$

In Equation 3.5, the angular momentum stays constant in the inertial frame, when external torques are absent. That means angular momentum change in the inertial frame is replaced with external torque $\boldsymbol{T}$. In the rigid body model, external disturbances and actuator output torques are the only possible external torque sources. $\boldsymbol{H^B_{tot}}$ is the overall angular momentum vector of the satellite with respect to the Body Frame, which consists of the angular momentum of the rigid body and reaction wheels, as shown in 3.6.

$$\boldsymbol{H^B_{tot}} = \boldsymbol{H^B} + \sum_i \boldsymbol{H^B_{wh_i}} \tag{3.6}$$

$$\left(\frac{d\boldsymbol{H}}{dt}\right)_B = \boldsymbol{T} - \boldsymbol{\omega^B} \times \boldsymbol{H^B_{tot}} \tag{3.7}$$

In the simulation, Rigid Body block employs Equation 2.19, 3.4, and 3.7 to make the time transition of those states. The Xcos block representation of Rigid Body model is depicted in Figure 3.1 and the overall parameter and input-output table for Rigid Body block is given in Table 3.1. The block is an "always-active" block, which means the calculation of state transition and output vectors are independent of external events and external calculation requests.

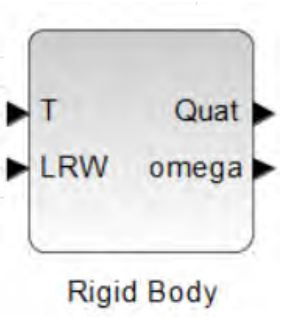

Figure 3.1.: Rigid Body block implemented in Xcos

Name	Type	Variable Type
Moment of Inertia of the overall body	Parameter	3x3 Double
Initial Attitude Quaternion	Parameter	4x1 Double
Initial Angular Velocity	Parameter	3x1 Double
Total External Torque	Input	3x1 Double
Total Reaction Wheel Angular Momentum	Input	3x1 Double
Current Quaternion Attitude	Output	4x1 Double
Current Angular Velocity	Output	3x1 Double
Angular Quaternion	State	4x1 Double
Attitude Velocity	State	3x1 Double

Table 3.1.: Rigid Body Block I/O Table

3.2. Disturbance Torques

In Wertz's opinion [12], the dominant disturbance torque sources are atmospheric drag, Earth's magnetic field, gravity gradient, solar radiation pressure, and micrometeorites. The reference mission of this thesis work states that the possible altitude values of the satellite lie between 500km and 650km. Thus, Solar radiation pressure, which is effective on interplanetary missions, and micrometeorites, which have no model are excluded from simulation dynamics [12].

3.2.1. Gravity Gradient

In the space environment, the gravitational field is not uniform and therefore, the gravitational force may display position-specific variations in both magnitude and directions. This variation results in gravitational torque applied on space objects around their center of mass. This phenomenon is used by Lagrange to explain why the Moon has always the same face toward Earth [23].

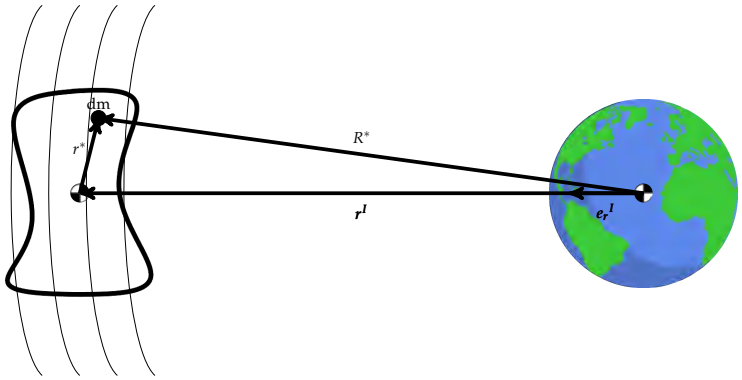

Source: Redrawn from Hughes, Figure 8.2 [23]
Earth Icon: wikipedia.com

Figure 3.2.: Gravitational field demonstration of Earth on a space object

Figure 3.2 depicts the Earth's gravitational field on any space object. Referencing Figure 3.2, Equation 3.8 was formed [23], in order to find the total gravity gradient torque on a spacecraft in an inertial frame, T^I_{gg}. Then, Equation 3.8 becomes Equation 3.9, where μ_E is the gravitational constant of Earth, $\boldsymbol{r^I}$ is the position vector of the spacecraft from Earth's center of mass, $\boldsymbol{e_r{}^I}$ is the position unit vector of the spacecraft, and I^I is the moment of inertia tensor of the spacecraft with respect to the inertial frame. This equation assumes that only one celestial body (Earth) applies the gravitational field, the mass distribution of Earth is spherically symmetrical, the spacecraft constitutes a single body, and the mass of the spacecraft is negligibly small [23]. If the moment of inertia

tensor is only given in the body frame, Equation 3.10 can be utilized. If the resultant gravity gradient torque is desired in body frame, Equation 3.11 may be used.

$$\boldsymbol{T_{gg}^{I}} = -\mu_E \int_M \frac{\boldsymbol{r^*} \times \boldsymbol{R^*}}{R^{*3}} dm \tag{3.8}$$

$$\boldsymbol{T_{gg}^{I}} = \frac{3\mu_E}{(r^I)^3} \left(\boldsymbol{e_r^I} \times I^I \boldsymbol{e_r^I} \right) \tag{3.9}$$

$$I^I = C^{B/I^T} \, I^B \, C^{B/I} \tag{3.10}$$

$$\boldsymbol{T_{gg}^{B}} = C^{B/I} \, \boldsymbol{T_{gg}^{I}} \tag{3.11}$$

As discussed in Section 2.2.1, the gravitational field of Earth shows zonal variations, which are approximated by the second degree of harmonics, called J_2. The implementation of J_2 perturbation on gravity gradient torque is shown in Equation 3.12 [25]. In this equation, J_2 is the second harmonics coefficient, R_E is the equatorial radius of Earth, and other parameters are shown in Equation 3.13 and 3.14 [25].

$$\begin{aligned} \boldsymbol{T_{ggj2}^{I}} = & \boldsymbol{T_{gg}^{I}} - \frac{3\mu_E R_E^2}{(r^I)^5} J_2 \begin{bmatrix} I_{yz} \\ -I_{xz} \\ 0 \end{bmatrix} + \frac{15\mu_E R_E^2 J_2}{2(r^I)^7} \left(\begin{bmatrix} r_x \\ r_y \\ 3r_z \end{bmatrix} \times (\widetilde{I}\boldsymbol{r^I}) \right) - \\ & \frac{15\mu_E R_E^2 J_2 r_z}{2(r^I)^7} \left(\boldsymbol{r^I} \times \begin{bmatrix} 2I_{xz} \\ 2I_{yz} \\ I_{xx} + I_{yy} + I_{zz} \end{bmatrix} \right) - \\ & \frac{105\mu_E R_E^2 J_2 r_z^2}{2(r^I)^9} \left(\boldsymbol{r^I} \times (I^I \boldsymbol{r^I}) \right) \end{aligned} \tag{3.12}$$

, where

$$\widetilde{I} = \begin{bmatrix} 0.5(I_{xx} - I_{yy} - I_{zz}) & -I_{xy} & -I_{xz} \\ -I_{xy} & 0.5(I_{yy} - I_{xx} - I_{zz}) & -I_{yz} \\ -I_{xz} & -I_{yz} & 0.5(I_{zz} - I_{xx} - I_{yy}) \end{bmatrix} \tag{3.13}$$

$$\boldsymbol{r^I} = \begin{bmatrix} r_x \\ r_y \\ r_z \end{bmatrix}, \; I^I = \begin{bmatrix} I_{xx} & I_{xy} & I_{xz} \\ I_{xy} & I_{yy} & I_{yz} \\ I_{xz} & I_{yz} & I_{zz} \end{bmatrix} \tag{3.14}$$

In the simulation, depending on J_2 variation enable/disable control from block parameters, Gravity Gradient block employs Equation 3.9 or 3.12 to calculate resultant gravity gradient torque output, without making any state transitions. The *Spacecraft GNC Toolbox* block representation of Gravity Gradient block is given in Figure 3.3. The overall parameter and input-output table for Gravity Gradient block is given in Table 3.2. The block is an "event-based" block, in terms of Xcos/Scicos environment, which means the calculation time of outputs is external event dependent.

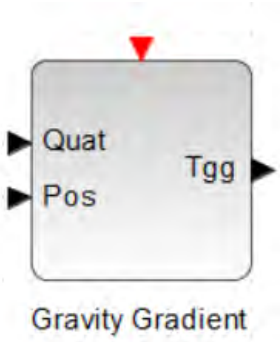

Figure 3.3.: Gravity Gradient block implemented in Xcos

Name	Type	Variable Type
Moment of Inertia of the overall body	Parameter	3x3 Double
J2 variation enable/disable	Parameter	1x1 Integer
Current Attitude Quaternion	Input	4x1 Double
Current Inertial Position	Input	3x1 Double
Gravity Gradient Torque	Output	3x1 Double

Table 3.2.: Gravity Gradient Block I/O Table

3.2.2. Atmospheric Drag

Spacecrafts orbiting around the Earth can dissipate their energy by atmospheric drag and then, they tend to descend towards Earth. This is a significant issue that affects the lifetime of space missions for altitudes, where the atmosphere can be perceived [23]. For some altitudes, the lifetime of the mission can be enough but aerodynamic torques become in-negligible, and therefore, atmospheric drag needs to be taken into account for modeling space environment [23].

The precise modeling of the atmospheric drag requires the employment of molecular momentum transfer analysis and a probabilistic approach. For simplicity purposes, the momentum transfer from molecules to the spacecraft surfaces is assumed to be perfectly inelastic, the mean motion of the atmosphere is much smaller than the speed of the spacecraft, and the relative motion between surface elements is much smaller than the speed of the center of the mass for rotating spacecraft [23]. As a result, Equation 3.15 gives the atmospheric drag torque on the spacecraft, where $H(x)$ is the Heaviside function of x, $\boldsymbol{r}$ is the position vector of dA with respect to the center of mass, ρ is the atmospheric density, C_D is the drag coefficient, which is found empirically [26], $\boldsymbol{V_R^B}$ is the atmospheric velocity related to the Earth's surface, and α is the angle of attack [23]. The angle of attack may be found in Equation 3.16, where $\boldsymbol{n_A}$ is the surface normal [23].

$$\boldsymbol{T_{atm}^B} = \oiint H(\cos\alpha)\,\rho C_D V_R^B \cos\alpha \boldsymbol{r} dA \times \boldsymbol{V_R^B} \tag{3.15}$$

$$\cos\alpha = \hat{\boldsymbol{V}}_{\boldsymbol{R}}^{\boldsymbol{B}} \cdot \boldsymbol{n_A} \tag{3.16}$$

Equation 3.17 gives the velocity of the satellite with respect to the Earth's atmosphere, where $\boldsymbol{V^I}$ is the velocity of the spacecraft, $\boldsymbol{R^I}$ is the position of the spacecraft, and $\boldsymbol{\omega_E^I}$ is the Earth rotation vector, all of them being related to the inertial frame [26]. Equation 3.17 simplifies to 3.18 [26].

$$\boldsymbol{V_R^I} = \boldsymbol{V^I} + \boldsymbol{\omega_E^I} \times \boldsymbol{R^I} \tag{3.17}$$

$$\boldsymbol{V_R^B} = C^{B/I} \begin{bmatrix} \dot{x} + \omega_E y \\ \dot{y} - \omega_E x \\ \dot{z} \end{bmatrix} \tag{3.18}$$

In the reference mission description, it is defined that the satellite is designed to have a cube shape, which has six different perpendicular surfaces. As a result, Equation 3.15 becomes Equation 3.19.

$$\boldsymbol{T_{atm}^B} = \sum_{i=1}^{6} H(\cos\alpha_i)\,\rho C_D V_{R_i}^B \cos\alpha_i A_i \boldsymbol{r_i} \times \boldsymbol{V_{R_i}^B} \tag{3.19}$$

The atmospheric density ρ is estimated via position-dependent atmospheric models. The most common atmospheric models are US Standard Atmosphere 1976 (US76), US Naval Research Laboratory Mass Spectrometer and Incoherent Scatter Radar 2000 (NRLMSISE-00), Drag Temperature Model 2013 (DTM2013), and Jacchia-Bowman 2008 (JB2008) [27]. US76 is a static atmospheric density model, in which the atmospheric density depends on only the satellite's altitude [28]. The remaining atmospheric models are categorized as empirical. The atmospheric density depends on the position and time of the satellite, in order to take the effect of diurnal and Solar cycles on the atmosphere into account. NRLMSISE-00 gives the density of N_2, O_2, Ar, He, O, H, N, anomalous oxygen, and their total by employing harmonic equations for each element and it depends on the solar flux at the wavelength of 10.7 cm ($F10.7$) [27]. JB2008 adds the extreme ultraviolet index ($S10.7$), Mg II index ($M10.7$), and Lyman-α and X-Ray weighted index ($Y10$) to $F10.7$ in order to calculate thermospheric heating more accurately [27]. DTM2013 employs the similar harmonic equations with NRLMSISE-00 but with $F30$ index instead of $F10.7$ [27].

As of January 2024, the Fortran source codes of the above-mentioned atmospheric density models are available at NASA Community Coordinated Modeling Center (CCMC) website [29]. Since Scilab allows users to call Fortran routines, all of these models can be used in Xcos simulations [30]. CelestLab v3.4.2 library under Scilab 2023.1.0 contains US76 and NRLMSISE-00 models. NRLMSISE-00 was selected as the atmospheric density model, due to its higher accuracy than US76. In earlier versions of Scilab (5.5.2) and CelestLab (v3.2.1), there were only US76 available and therefore, NRLMSISE-00 Fortran source code was downloaded from CCMC website and Scilab was calling its proper subroutines successfully.

The selection of the atmospheric density model of Atmospheric Drag block in Xcos is parameterized in between US76 and NRLMSISE-00. This block uses Equation 3.16, 3.18, and 3.19 to calculate aerodynamic torque on the satellite. The Xcos implementation of Atmospheric Drag torque block is given in Figure 3.4 and the overall parameter and input-output table for Atmospheric Drag block are given in Table 3.3. The block is an "event-based" block, in terms of Xcos/Scicos environment, which means the calculation time of outputs is external event dependent.

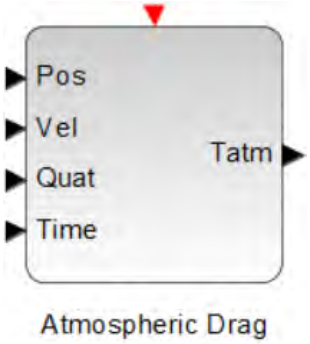

Figure 3.4.: Atmospheric Drag torque block implemented in Xcos

Name	Type	Variable Type
Atmospheric Mass Density Model	Parameter	1x1 Integer
81 Day Avg. of F10.7 Flux	Parameter	1x1 Double
Daily F10.7 Flux Avg. for the previous day	Parameter	1x1 Double
Drag Coefficient of the Satellite	Parameter	1x1 Double
Alignment of the cube e eee.r.t. Body Frame (RPY Angles)	Parameter	3x1 Double
Cube Length of the Satellite	Parameter	1x1 Double
Geometric Center Coordinates w.r.t. Body Frame	Parameter	3x1 Double
Current Position w.r.t. Inertial Frame	Input	3x1 Double
Current Velocity w.r.t. Inertial Frame	Input	3x1 Double
Current Attitude Quaternion	Input	4x1 Double
Current Time in Modified Julian Date	Input	1x1 Double
Aerodynamic Torque	Output	3x1 Double

Table 3.3.: Atmospheric Drag Block I/O Table

3.2.3. Earth Magnetic Field

In early nineteenth century, German mathematician Karl Gauss started a systematical study on Earth Magnetic field. The strength of Earth magnetic dipole is around $7.96 \times 10^{15} Wb.m$, which annually drifts westward [12]. The magnetic field is the weakest at magnetic equator, which is around $3 \times 10^{-5} T$ at the surface. After utilization of Maxwell equations with well-known Earth magnetic field anomalies, the scalar magnetic potential at any point near Earth can be given as the sum of spherical harmonics, like in Equation 3.20 [12]. In Equation 3.20, V is the scalar magnetic potential, a is the Earth equatorial radius, g_n^m and h_n^m are Gaussian coefficients, r is the distance from the center of Earth, θ is co-elevation, ϕ is the East longitude, and $P_n^m(\theta)$ are Legendre functions [12].

$$V(r,\theta,\phi) = a \sum_{n=1}^{N} \sum_{m=0}^{n} \left(\frac{a}{r}\right)^{n+1} \left(g_n^m \cos m\phi + h_n^m \sin m\phi\right) P_n^m(\theta) \tag{3.20}$$

The set of Gaussian coefficients that models Earth magnetic field is named as The International Geomagnetic Reference Field (IGRF). The first IGRF model, IGRF-1 was published in 1968. Depending on Earth magnetic field measurements and predictions, IGRF coefficients are revised generally every five years. The latest model is IGRF-13 published in 2019, whose validity period is from 1900 to 2025 and can give predictions until 2030 [31]. Scilab offers IGRF-12, the previous version of IGRF-13, which can give predictions until 2025. Since the mission timeline is planned between 2028 and 2030, the utilization of IGRF-13 was necessary and therefore, the Fortran source code of IGRF-13 was downloaded from the website [32] and imported to Magnetic Field block of *Spacecraft GNC Toolbox*.

For Attitude Control System (ACS), the magnetic field vector is being used in the estimation of magnetic field disturbance due to satellite residual magnetic dipole moment and torque generation by the help of magnetorquers, will be mentioned in Section 3.3.5. Depending on the input parameter, the block runs the IGRF-13 Fortran subroutine or Scilab IGRF-12 function to get the magnetic field vector at a given position and time with respect to the Earth Centered Fixed Frame (ECF), which rotates with

Earth. The block simply multiplies the magnetic field in a fixed frame with a rotational transformation matrix, as in Equation 3.21, to get the magnetic field vector in ECI frame. For simplicity purposes, the magnetic field disturbance torque is calculated inside magnetorquer block.

$$\boldsymbol{B^I} = C^{I/F}\boldsymbol{B^F} \tag{3.21}$$

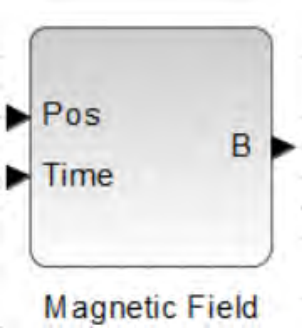

Figure 3.5.: Magnetic Field propagator block implemented in Xcos

Name	Type	Variable Type
Magnetic Field Model	Parameter	1x1 Integer
Current Position w.r.t. Inertial Frame	Input	3x1 Double
Current Time in Modified Julian Date	Input	1x1 Double
Magnetic Field Vector w.r.t. Inertial Frame	Output	3x1 Double

Table 3.4.: Magnetic Field Propagator Block I/O Table

3.3. Hardware

AOCS systems use digital hardware for executing attitude determination and control tasks. In the space technology of 2023, gyroscopes, accelerometers, magnetometers, sun sensors, Earth sensors, and star trackers are used in attitude determination-related operations, and reaction wheels, momentum wheels, control moment gyroscopes, magnetorquers, attitude thrusters are used as attitude control actuators [33]. In this thesis work, star tracker, gyroscope, and magnetometer were selected as attitude determination sensors. The selected actuators are reaction wheel and magnetorquer. In addition, the on-board computing unit is also explained in detail.

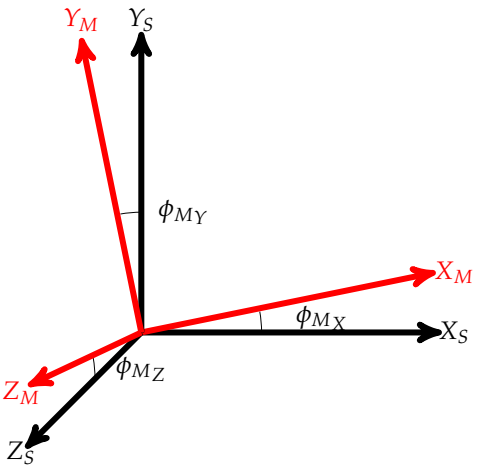

Figure 3.6.: Misalignment error demonstration

All of ACS sensors and actuators are subjected to misalignment error, which defines a constant attitude error related to the sensor frame . Misalignment errors might be represented as Euler angles or quaternions. The illustration of misalignment error is shown in Figure 3.6, where (X_S, Y_S, Z_S) comprises the sensor frame, (X_M, Y_M, Z_M) is the sensor frame with the misalignment error, and $\phi_{MX}, \phi_{MY}, \phi_{MZ}$ are misalignment errors as Roll-Pitch-Yaw angles, respectively.

3.3.1. Star Tracker

Stars are inertially fixed objects in space and therefore, they constitute the most accurate attitude determination source. Star trackers give arc-second level attitude output by using the star catalog, which gives the magnitude, spectrum, and coordinates of stars with respect to the ECI frame. Despite the high attitude accuracy of star trackers, they have high complexity and relatively expensive hardware [33].

Star trackers simply consist of a digital camera with either Charge-Coupled Device or

CMOS sensors. In operation, star trackers have two modes: Attitude acquisition mode and tracking mode. In attitude acquisition mode, the sensor has no knowledge about its attitude and tries to estimate its attitude by matching stars in the Field of View with its star catalog [26]. In tracking mode, the attitude acquisition process was finished. The main error sources of pixels on Star trackers are Shot Noise, Dark Current, and Hot Pixels [26]. In order to eliminate those errors, high integration time is required, which limits the angular rate at which it can operate [26]. The accuracy of two axes perpendicular to the boresight (cross) of star tracker output is larger than roll (about) axis accuracy, due to the root-mean-square distance of starts from the boresight [26]. Figure 3.7 illustrates the boresight and roll axes with respect to the star tracker.

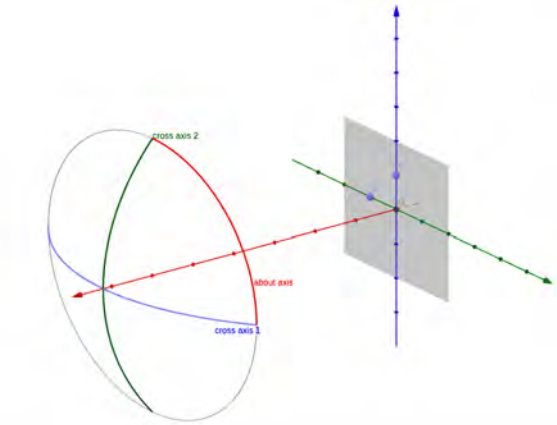

Source: https://space.stackexchange.com

Figure 3.7.: Star Tracker boresight (cross) and roll (about) axes demonstration

$$q_{meas}^{I/S} = q_{true}^{I/S} * q^M * q^N \tag{3.22}$$

In the simulation, Star Tracker block employs Equation 3.22, where $q_{meas}^{I/S}$ is the sensor attitude output in quaternions, $q_{true}^{I/S}$ is the true value of the sensor attitude, q^M is the misalignment error in quaternion, as shown in Figure 3.6, and q^N is the measurement noise. The difference in accuracy values cross and about axis was taken into account in the calculation of q^N. This block also takes the angular rate of the rigid body with respect to the inertial frame, in order to detect the event of angular limit excess. The Xcos implementation of Star Tracker block is given in Figure 3.8 and the overall parameter and input-output table for Star Tracker block is given in Table 3.5. The block is event-triggered, in terms of Xcos/Scicos environment, which means the calculation of state transitions and outputs are dependent on external events.

Figure 3.8.: Star Tracker block implemented in Xcos

Name	Type	Variable Type
The attitude of Star Tracker frame w.r.t. Body Frame Quaternion	Parameter	4x1 Double
Noise standard deviation in Cross and About axes	Parameter	2x1 Double
Misalignment error in Euler Angles (X-Y-Z)	Parameter	3x1 Double
Angular rate limit for the measurement	Parameter	1x1 Double
Current Quaternion Attitude w.r.t. BF	Input	4x1 Double
Current Angular Rate of BF w.r.t.	Input	3x1 Double
Attitude Measurement w.r.t. Star Tracker frame BF	Output	4x1 Double
Status Flag (0: OK, 1: Angular rate limit exceeded)	Output	1x1 Double

Table 3.5.: Star Tracker Block I/O Table

3.3.2. Gyroscope

Gyroscopes give the angular rate of gyroscope frame with respect to the inertial frame. They fall into two categories: Rate gyros giving the angular rate and rate integrating gyros giving the angular displacement as output [26]. Gyroscope technologies up to now are, Ring Laser Gyroscopes (RLG), Dynamically Tuned Gyroscopes (DTG), Hemispherical Resonant Gyroscopes (HRG), Interferometric Fiber Optic Gyroscopes (IFOG), and MEMS Gyroscopes.

$$\boldsymbol{\omega}_{\boldsymbol{meas}}^{\boldsymbol{I/G}} = \boldsymbol{\omega}_{\boldsymbol{true}}^{\boldsymbol{I/G}} + \boldsymbol{b}_{\boldsymbol{gy}} + \boldsymbol{s}_{\boldsymbol{gy}} + \boldsymbol{o}_{\boldsymbol{gy}} + \boldsymbol{n}_{\boldsymbol{gy}} \tag{3.23}$$

Gyroscope measurement output formula is given in Equation 3.23, where $\boldsymbol{\omega}_{\boldsymbol{meas}}^{\boldsymbol{I/G}}$ is the angular rate of Gyroscope frame related to inertial frame measurement output, $\boldsymbol{\omega}_{\boldsymbol{true}}^{\boldsymbol{I/G}}$ is the actual angular rate value, $\boldsymbol{b}_{\boldsymbol{gy}}$ is the sensor bias, $\boldsymbol{s}_{\boldsymbol{gy}}$ is the gyroscope scale error, $\boldsymbol{o}_{\boldsymbol{gy}}$ is the non-orthogonality error, and $\boldsymbol{n}_{\boldsymbol{gy}}$ is the sensor noise [34]. In the simulation, Gyroscope block employs Equation 3.23. In *Spacecraft GNC Toolbox*, Gyroscope block has the capability of multiple axes gyroscope measurements. As of February 2024, the Xcos implementation of Gyroscope block is given in Figure 3.9, and the overall parameter and input-output table for Gyroscope block is given in Table 3.6. The block

is event-triggered, in terms of Xcos/Scicos environment, which means the calculation of state transitions and outputs are dependent on external events.

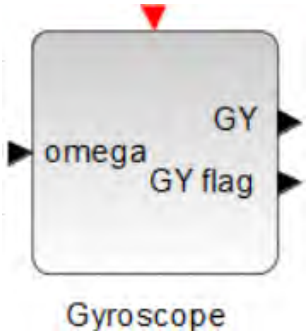

Figure 3.9.: Gyroscope block implemented in Xcos

Name	Type	Variable Type
The gyroscope measurement axes unit vectors	Parameter	nx3 Double
Measurement noise mean	Parameter	1x1 Double
Measurement noise standard deviation	Parameter	1x1 Double
Measurement scale error	Parameter	1x1 Double
Misalignment error in Euler Angles (X-Y)	Parameter	2x1 Double
Angular Random Walk	Parameter	1x1 Double
Angular Rate Measurement Limit	Parameter	1x1 Double
The number of quantization bits	Parameter	1x1 Integer
Current Angular Rate of BF w.r.t. ECI	Input	3x1 Double
Attitude Measurement w.r.t. Gyroscope frame	Output	nx1 Double
Status Flag (0: OK, 1: Positive Saturation, 2:Negative Saturation)	Output	nx1 Double

Table 3.6.: Gyroscope Block I/O Table

3.3.3. Magnetometer

Magnetometers are the sensors that give the direction and the magnitude of the magnetic field vector. These sensors are lightweight and require low power but they are not precise due to the uncertainties in magnetic field [12]. Since Earth's magnetic field is inversely proportional to the distance from the center of Earth, the region of interest of magnetometers is the sphere around the Earth with an altitude below 1000 km [12].

Anisotropic Magnetoresistive (AMR), Fluxgate, and MEMS are commonly used types of magnetometers in microsatellite applications. Due to having the highest detectivity at low frequencies, producing bipolar output, and being anisotropic, AMR magnetometers gained popularity [35]. Fluxgate magnetometers consist of two different coils. The primary coil produces a magnetic field, which will cause an ambient magnetic field to appear at the second coil as a second harmonic [12]. MEMS-based magnetometers use

Lorentz Force and Hall effect for magnetic field measurement [36].

$$\boldsymbol{B}_{\boldsymbol{meas}}^{\boldsymbol{MM}} = C^{M/B} C^{B/I} \boldsymbol{B}_{\boldsymbol{true}}^{\boldsymbol{I}} + \boldsymbol{n}_{\boldsymbol{mm}} \tag{3.24}$$

Equation 3.24 gives the Magnetometer measurement output, where $\boldsymbol{B}_{\boldsymbol{meas}}^{\boldsymbol{MM}}$ is the magnetic field measurement related to magnetometer frame, $\boldsymbol{B}_{\boldsymbol{true}}^{\boldsymbol{I}}$ is the actual magnetic field vector with respect to the inertial frame, $C^{B/I}$ is the rotation matrix from inertial to body frame, $C^{M/B}$ is the rotation matrix from body to magnetometer frame, and $\boldsymbol{n}_{\boldsymbol{mm}}$ is the sensor noise. In the toolbox, Magnetometer block employs Equation 3.24. This block takes the magnetic field in inertial frame from Magnetic Field propagator block, which was explained in Section 3.2.3. The Xcos implementation of Magnetometer block is given in Figure 3.10 and the overall parameter and input-output table for Magnetometer block is given in Table 3.7. The block is event-triggered.

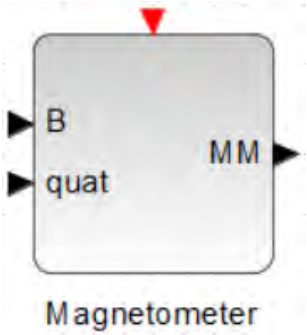

Figure 3.10.: Magnetometer block implemented in Xcos

Name	Type	Variable Type
Quaternion Attitude of magnetometer w.r.t. Body Frame	Parameter	4x1 Double
Measurement noise mean	Parameter	3x1 Double
Measurement noise standard deviation	Parameter	3x1 Double
Magnetic Field vector w.r.t. ECI	Input	3x1 Double
Current Quatertnion Attitude w.r.t. ECI	Input	4x1 Double
Magnetometer Measurement w.r.t. Magnetometer frame	Output	3x1 Double

Table 3.7.: Magnetometer Block I/O Table

3.3.4. Reaction Wheel

Momentum exchange devices help ACS distribute the angular momentum inside the spacecraft. They consist of an electrical motor. Reaction wheels provide torque and angular momentum to the spacecraft with its motor and zero momentum bias, unlike momentum wheels. Nevertheless, the overall angular momentum of the satellite does not change during their operation [33].

According to Sidi [33], there is a dynamic torque-momentum limitation for momentum exchange wheels due to their output power capacity. In other words, as shown in

Figure 3.11, the wheels cannot exert their maximum torque after reaching the angular momentum threshold while conserving the power output. This is a significant aspect of the wheels that was considered during the development of the Reaction Wheel block on Scilab.

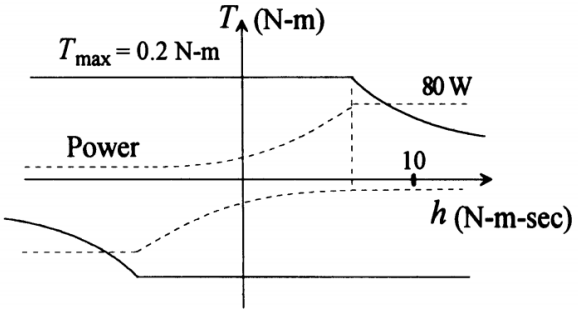

Source: Sidi, Spacecraft Dynamics and Control (1997) [33]

Figure 3.11.: Reaction wheel Torque-Angular Momentum plot

The Reaction Wheel block of *Spacecraft GNC Toolbox* applies the torque with Gaussian noise in its nominal operation and integrates it to obtain angular momentum, which is expressed in Equation 3.25. In this equation, L_{rw_i} is the angular momentum of each wheel, T_{rw_i} is the torque exerted from the wheel, and n is the actuator noise.

$$\frac{dL_{rw_i}}{dt} = T_{rw_i} + n \rightarrow L_{rwi} = \int T_{rw_i} + n dt \tag{3.25}$$

The inertia and friction of reaction wheels cause transient behavior in between current and target rotation speed and torque of reaction wheels in their nominal operation region. This transient is modeled as PT1 (First Order) Delay and explained in Equation 3.26 [37], where τ_{PT1} is the time constant of PT1 delay.

$$\frac{dT_{rw_i}}{dt} = -\frac{T_{rw_i} - T_{cmd_{rw_i}}}{\tau_{PT1}} \tag{3.26}$$

Sidi expresses that the reaction wheel reaches its power capacity before reaching its angular momentum capacity [33]. For the region in between nominal operation and angular momentum saturation, Equation 3.27 could be written where P_{rw_i} is the instantaneous power, I_{rw} is the moment of inertia of the wheel. By taking the partial derivatives of reaction wheel rotational power from Equation 3.27, Equation 3.30 may

be obtained.

$$P_{rw_i} = T_{rw_i}(t)\frac{L_{rw_i}(t)}{I_{rw}} \text{ and } \frac{dP_{rw_i}}{dt} = 0 \tag{3.27}$$

$$\frac{\partial P_{rw_i}}{\partial T_{rw_i}} = \frac{L_{rw_i}}{I_{rw}} \text{ and } \frac{\partial P_{rw_i}}{\partial L_{rw_i}} = \frac{T_{rw_i}}{I_{rw}} \tag{3.28}$$

$$\frac{dP_{rw_i}}{dt} = \frac{\partial P_{rw_i}}{\partial L_{rw_i}}\frac{dL_{rw_i}}{dt} + \frac{\partial P_{rw_i}}{\partial T_{rw_i}}\frac{dT_{rw_i}}{dt} = 0 \tag{3.29}$$

$$\frac{dT_{rw_i}}{dt} = -\frac{T_{rw_i}}{L_{rw_i}}\frac{dL_{rw_i}}{dt} \tag{3.30}$$

The Xcos implementation of the reaction wheel block is given in Figure 3.12 and the power capacity test diagram is given in Figure 3.13 and the resultant plot is Figure 3.14. The diagram has a single reaction wheel, whose maximum angular momentum value is $0.1N.m.s$ and maximum torque is $6 \times 10^{-3}N.m$, and the input is $T_{cmd}(t) = u(t) - 2u(t-50) + 2u(t-100)$, where $u(t)$ is the step function. According to the resultant plot, when the angular momentum of the wheel exceeds the linear region threshold ($0.5N.m.s$) in both signs and the sign of the torque is the same as the sign of the angular momentum, the power output of the wheel is saturated. Hence, asymptotic curves at the right-top and left-bottom side of Figure 3.14 occur. To notice, the reason for jumps at left-top and right-bottom is the above-mentioned PT1 delay. The zero lines at the leftmost and rightmost sides of Figure 3.14 are caused by the deliberate implementation of zero torque at the No-Load case, when the angular momentum capacity is reached. As a result, the torque-angular momentum relation of the reaction wheel block of *Spacecraft GNC Toolbox* is approximated to the reality, as it might be seen in Figure 3.11 and 3.14.

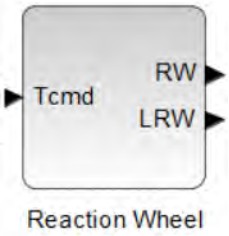

Figure 3.12.: Reaction Wheel block implemented in Xcos

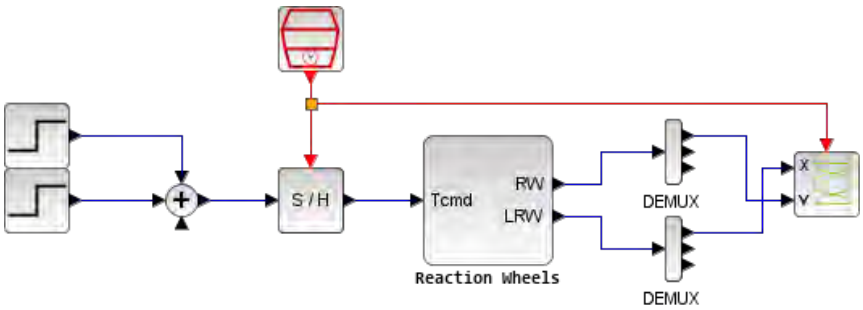

Figure 3.13.: Reaction wheel power capacity test diagram

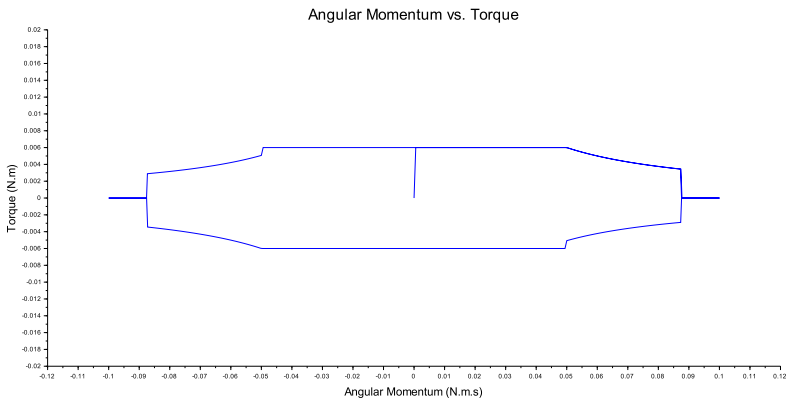

Figure 3.14.: Reaction wheel torque-angular momentum relation

Reaction wheel block of the toolbox has the capability to contain multiple wheels. Note that, the block interface file allows for the inclusion of four reaction wheels, only three wheel cases (without redundant wheels) were tested throughout the thesis work, however. Outside this block, Equation 3.6 and 3.7 give the Rigid Body angular momentum state transition with reaction wheels. The overall parameter and input-output table for the reaction wheel block are given in Table 3.8. The block is not an always-active and not event-triggered block, in terms of Xcos/Scicos environment, which means the calculation of state transitions and outputs are dependent on calculation requests only. Therefore, the Sample/Hold block is utilized before the reaction wheel block, for the purpose of discretization.

Name	Type	Variable Type
Single Reaction Wheel Moment of Inertia Matrix (Reserved)	Parameter	3x3 Double
Spin axes of wheels w.r.t. BF	Parameter	nx3 Double
Misalignment error in Euler Angles (X-Y-Z)	Parameter	3x1 Double
Single wheel angular momentum capacity	Parameter	1x1 Double
Single wheel momentum margin before saturation	Parameter	1x1 Double
Output torque noise mean	Parameter	1x1 Double
Output torque noise standard deviation	Parameter	1x1 Double
Wheel PT1 Delay Time constant	Parameter	1x1 Double
Torque Output (PT1 Delay)	State	nx1 Double
Angular Momentum Output	State	nx1 Double
Torque Command	Input	nx1 Double
Overall Torque Output w.r.t. BF	Output	3x1 Double
Overall Angular Momentum Output w.r.t. BF	Output	3x1 Double

Table 3.8.: Reaction Wheel Block I/O Table

3.3.5. Magnetic Torquer

According to Sidi [33], magnetorquers generate torques on a spacecraft by generating magnetic dipole moments for the purposes of momentum dumping and active nutation control. Thanks to being lightweight, they are feasible alternatives to attitude thrusters [33].

The torque generated on an energized magnetorquer is given in Equation 3.31, where $\boldsymbol{T_{mt}^B}$ is the torque generated due to magnetorquers in BF, $\boldsymbol{m_{mt}^B}$ is the magnetic dipole of torquers, which depends on input command, and $\boldsymbol{B^B}$ is the Earth magnetic field vector coming from Magnetic Field block, mentioned in Section 3.2.3. As seen from Equation 3.31, the torque created on magnetorquers is dependent on Earth's magnetic field strength, which changes with the position of the spacecraft and the distance from the center of Earth. Therefore, for higher altitudes, the torque output drops to lower levels [33]. Moreover, since magnetorquers generate a magnetic field around coils, including electronic components inside the spacecraft like magnetometers, the operation of magnetorquers can disrupt magnetometer measurements [33].

$$\boldsymbol{T_{mt}^B} = \boldsymbol{m_{mt}^B} \times \boldsymbol{B^B} \tag{3.31}$$

$$\boldsymbol{T_{mt}^B} = \left(\boldsymbol{m_{sv}^B} + \sum_{i=1}^{N} \boldsymbol{m_{mt_i}^B} \right) \times \left(C^{B/I} \boldsymbol{B^I} \right) + \boldsymbol{n_{mt}} \tag{3.32}$$

In order to calculate the overall magnetic torque on the spacecraft, The magnetic torque equation should contain all components having magnetic dipole moment, which are the residual dipole moment of the spacecraft and magnetorquer rods. Thus, Equation 3.31 becomes Equation 3.32, taking the Earth magnetic field input vector's being defined in the inertial frame into account. In Equation 3.32, $\boldsymbol{T_{mt}^B}$ is the resultant overall magnetic torque, $\boldsymbol{m_{sv}^B}$ is the residual magnetic dipole moment of the spacecraft, $\boldsymbol{m_{mt_i}^B}$ is the magnetic dipole moment of each magnetorquer rod, $\boldsymbol{B^I}$ is the Earth magnetic field vector in the inertial frame, N is the number of magnetorquer rods, $C^{B/I}$ is the rotation matrix from inertial to body frame, and $\boldsymbol{n_{mt}}$ is the actuator noise. Magnetorquer block takes the magnetic field in the inertial frame from magnetic Field propagator block from Section 3.2.3. The Xcos implementation of magnetorquer block is given in Figure 3.15 and the overall parameter and input-output table for magnetorquer block is given in Table 3.9. The block is designed to be event-triggered.

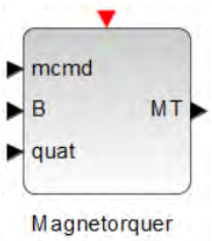

Figure 3.15.: Magnetorquer block implemented in Xcos

Name	Type	Variable Type
Residual magnetic dipole moment of the spacecraft w.r.t. BF	Parameter	3x1 Double
Unit vectors of torquers w.r.t. BF	Parameter	nx3 Double
Torquer dipole moment positive saturation	Parameter	nx1 Double
Torquer dipole moment negative saturation	Parameter	nx1 Double
Single wheel momentum margin before saturation	Parameter	1x1 Double
Output torque noise mean in X-Y-Z axes of BF	Parameter	3x1 Double
Output torque noise standard deviation in X-Y-Z axes of BF	Parameter	3x1 Double
Magnetic Dipole Moment Command	Input	nx1 Double
Earth Magnetic Field vector w.r.t. ECI	Input	3x1 Double
Current Quatertnion Attitude w.r.t. ECI	Input	4x1 Double
Overall Magnetic Torquer Output w.r.t. BF	Output	3x1 Double

Table 3.9.: Magnetorquer Block I/O Table

3.3.6. On Board Computer

The onboard computers (OBC) perform the onboard attitude control via combining onboard sensors and torquers through control laws and control strategies, according to Wertz [12]. Since human interaction in space missions is limited to remote communication ACS, there is a need to onboard computers, in order to automate sensor readings, run Guidance Navigation and Control algorithms, check the status of the spacecraft, and conduct controller mode transitions.

In this thesis work, OBC is modeled as a single block named "Attitude Controller" for Xcos simulations. This block employs attitude control equations stated in Chapter 5. It constructs a map between control laws and the controller mode and executes the control law depending on the mode. Mode definitions are given in Section 4.2 and the control law selection with corresponding control modes is declared in Table 5.1. As an early statement, since the attitude observer is out of the scope of this thesis work, the sensor readings from star trackers and gyroscopes were assumed as attitude observer outputs. Therefore sensors, actuators, and attitude controller block could have the same clock input for time synchronization. Hence, the block was designed as event-triggered. The Xcos implementation of attitude controller block in *Spacecraft GNC Toolbox* is given in Figure 3.16 and the overall parameter and input-output table for the block is given in Table 3.10.

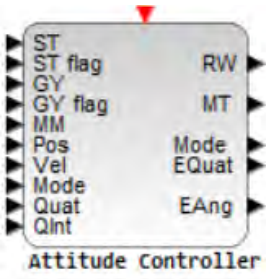

Figure 3.16.: Attitude Controller block implemented in Xcos

Name	Type	Variable Type
Nadir Pointing mode accuracy conditions	Parameter	2x1 Double
Zenith Pointing mode accuracy conditions	Parameter	2x1 Double
Inertial Pointing mode accuracy conditions	Parameter	2x1 Double
Moment of Inertia matrix w.r.t. BF	Parameter	3x3 Double
Gyroscope measurement axes w.r.t. BF (Reserved)	Parameter	nx3 Double
Reaction wheel actuation axes w.r.t. BF (Reserved)	Parameter	nx3 Double
Magnetorquer actuation axes w.r.t. BF (Reserved)	Parameter	nx3 Double
Quaternion integral gain	Parameter	3x1 Double
Slew mode quaternion control gain	Parameter	3x1 Double
Slew mode angular rate control gain	Parameter	3x1 Double
De-Tumbling mode technique	Parameter	3x1 Double
De-Tumbling mode actuator gains	Parameter	2x1 Double
Nadir pointing mode Q matrix	Parameter	6x6 Double
Nadir pointing mode R matrix	Parameter	3x3 Double
Zenith pointing mode Q matrix	Parameter	6x6 Double
Zenith pointing mode R matrix	Parameter	3x3 Double
Inertial pointing mode Q matrix	Parameter	6x6 Double
Inertial pointing mode R matrix	Parameter	3x3 Double
Star Tracker measurement output quaternion	Input	4x1 Double
Star Tracker output status	Input	1x1 Double
Gyroscope measurement output	Input	nx1 Double
Gyroscope output status	Input	nx1 Double
Magnetometer measurement output	Input	3x1 Double
Current position w.r.t. inertial frame	Input	3x1 Double
Current velocity w.r.t. inertial frame	Input	3x1 Double
Control mode selection	Input	1x1 Double
Inertial mode target attitude quaternion	Input	4x1 Double
Attitude error integral quaternion	Input	4x1 Double
Reaction wheel input torque command	Output	nx1 Double
Magnetorquer input torque command	Output	nx1 Double
Current control mode	Output	1x1 Double
Current attitude error quaternion	Output	4x1 Double
Current angular rate error	Output	3x1 Double

Table 3.10.: Attitude Controller Block I/O Table

4. Design

4.1. Reference Mission Description

The figurative reference mission scenario suggests that the satellite will have a scientific telescope that makes observations on space objects while orbiting the Earth. The main aim of ACS is to meet the attitude stability and accuracy requirements, which are dependent on mission phases. The mission orbit is selected as a Sun-Synchronous Orbit to provide constant illumination. The minimum and maximum values of the desired orbit parameters of the mission are given in Table 4.1.

Name	Minimum Value	Maximum Value	Unit
ACS Operational Start Date	01 Jan 2028	31 Dec 2030	Calendar Date
Altitude	500	650	km
Eccentricity	0	0.01	Unitless
Inclination[1]	-	-	deg
Right Ascension of Ascending Node[2]	-	-	deg
Argument of Perigee	0	360	deg
Start Mean Anomaly	0	360	deg

Table 4.1.: Mission Orbit Parameters

Section 2.2.2 suggests that eccentricity, semi-major axis, and inclination parameters of the satellite orbit should be adjusted, in order to propagate a Sun-Synchronous orbit. In this thesis work, this adjustment was made with "CL_op_ssoJ2" function of CelestLab library, which gives the required inclination value, once the semi-major axis and eccentricity were given as inputs. The verification of being Sun-Synchronous was made through NASA General Mission Analysis Tool (GMAT) R2022a software. The Keplerian elements of the orbit, given in Table 4.1 are provided as inputs to the software. The mission start date was arbitrarily given as "01 Jan 2028", and the altitude was selected as $500km$. The resultant RAAN plot generated in GMAT software was given in Figure 4.1. After the extraction of the RAAN plot to a file, the slope of the line in

[1] Inclination is calculated using Eq. 2.12 to keep having Sun-Synchronous orbit.
[2] Desired Local Time of Ascending Node is 06:00 a.m. See Section 2.2.2

Figure 4.1 was calculated as $0.9926 deg/s$, which is approximate to the value found in Section 2.2.2, $0.9856 deg/s$. This slight difference is sourced from having different gravity models. Celestlab was using the Keplerian orbit propagator with J_2 perturbation, while GMAT uses Joint Gravity Model-2 (JGM-2), which has more orders/degrees than the CelestLab's model. Therefore, despite such deviation, it is proven that the calculated inclination value for having a Sun-Synchronous orbit, was correct and the mission orbit was approved to be Sun-Synchronous.

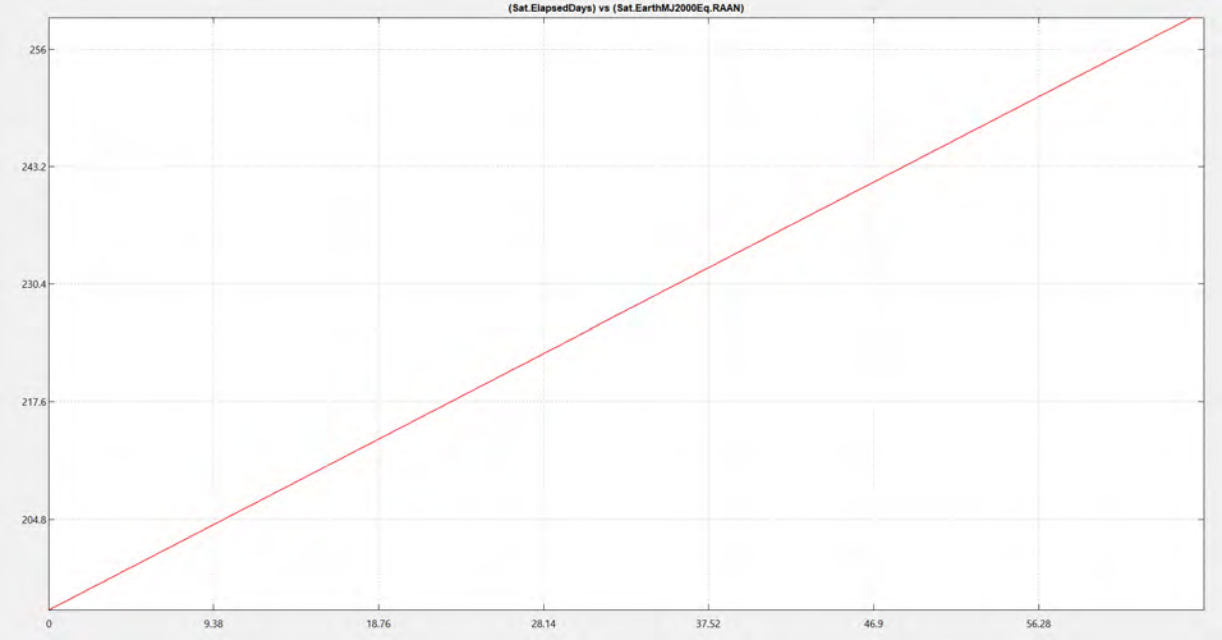

Figure 4.1.: Elapsed days since mission start date vs. RAAN plot

Figure 4.2 illustrates the orbit in ICRF throughout 2028, which intuitively verifies that the orbit is Sun-Synchronous. In Figures 4.2a to 4.2d, X, Y, and Z lines are vectors of ICRF and the S line shown in yellow is the vector from the center of the Earth to the Sun. From these figures, it can be deduced that the Sun vector has approximately the right angle against the orbital plane and throughout the year, it does not deviate. This also meets the LTAN requirement of being 06.00 a.m.

As suggested in Section 2.1.3, the body frame of the satellite has the origin located at its center of mass point. The scientific telescope points towards $+Z$ axis. X and Y axis share two perpendicular lateral axes, being orthogonal with Z axis as well. Apart from body frame, the mechanical frame is defined inside the mission scenario, in order to provide more understanding of operations with respect to the launch adapter of the satellite. The mechanical frame origin is defined at the geometric center of the bottom side of the satellite, which is also the geometric center of proposed launch adapter. The illustrations of satellite body and mechanical frames are given in Figure 4.3 and the mechanical properties of the satellite are given in Table 4.2.

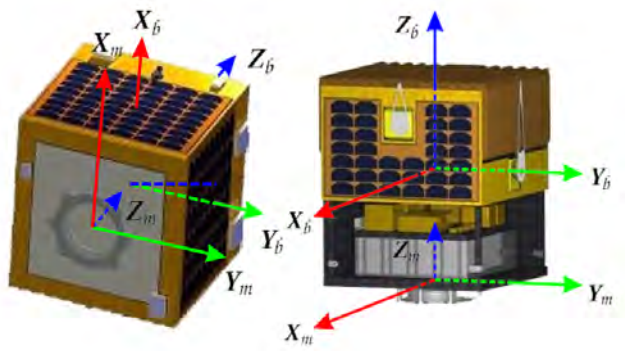

Source: https://www.dlr.de/irs/desktopdefault.aspx/tabid-12525/21846_read-49985/

Figure 4.3.: Satellite body and mechanical frame definitions

Name	Value
Shape Model	Cube with $0.6m$ edge length
Weight	$25.8kg$
Center of Mass w.r.t. Geometric Center	$\begin{bmatrix} 0.02 \\ 0.03 \\ -0.05 \end{bmatrix}$ m
Moment of Inertia[3]	$\begin{bmatrix} 1.67 & 0 & 0 \\ 0 & 1.6 & 0 \\ 0 & 0 & 1.57 \end{bmatrix}$ $kg.m^2$
Maximum Residual Magnetic Dipole Magnitude	$1A.m^2$

Table 4.2.: Satellite mechanical properties

[3]Off-diagonal elements can be 10 percent large as diagonal elements

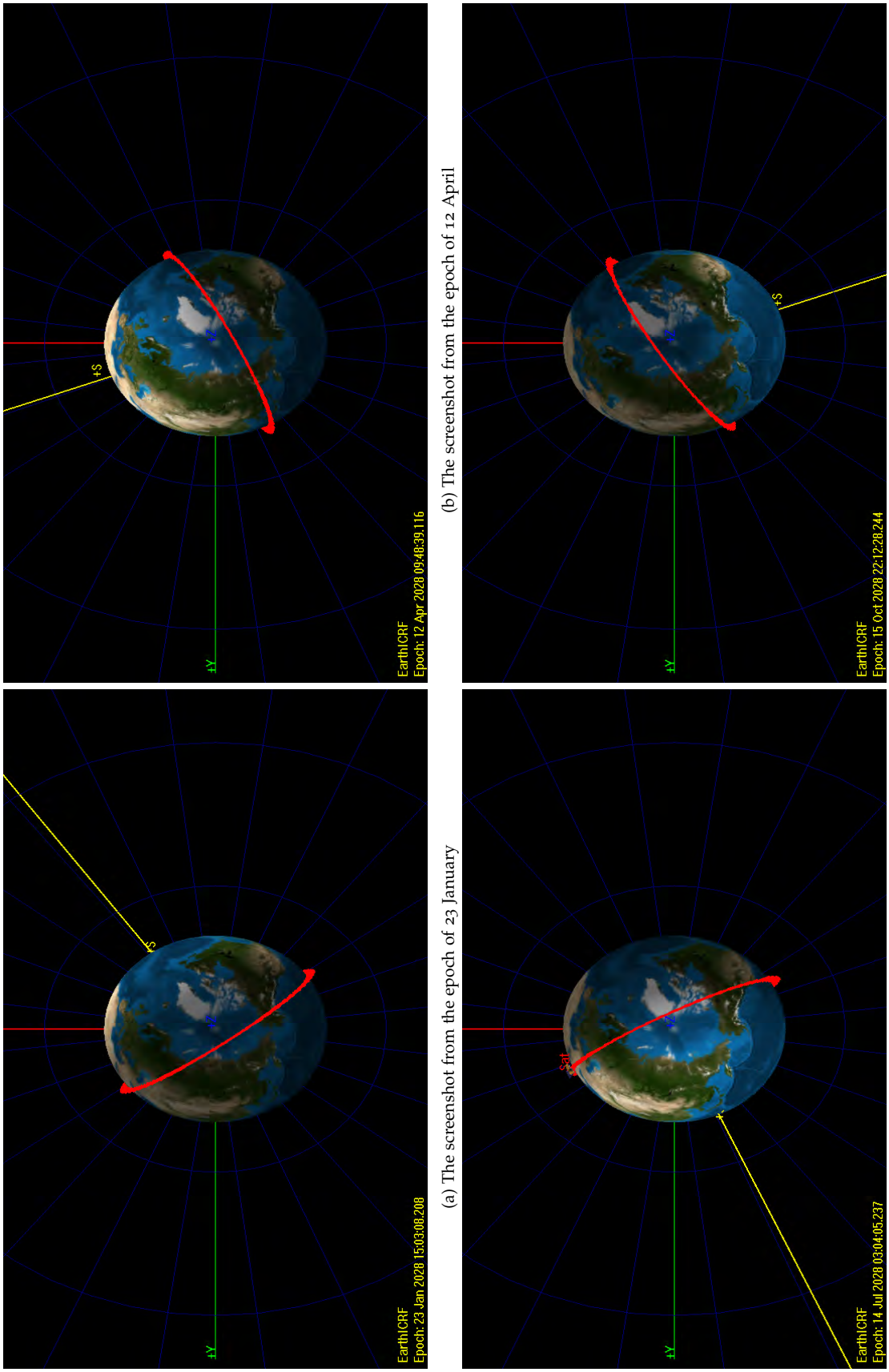

(a) The screenshot from the epoch of 23 January

(b) The screenshot from the epoch of 12 April

(c) The screenshot from the epoch of 14 July

(d) The screenshot from the epoch of 15 October

Figure 4.2.: The mission orbit vs. Sun vector illustration throughout 2028 related to ICRF, implemented in GMAT R2022a

4.2. Mode Definitions

In the lifetime of the mission, the satellite will take scientific recordings through the scientific telescope. In order to handle every situation that could occur during the mission, the operation of ACS has to be analyzed phase by phase. In the figurative reference mission, there are three pre-defined nominal operational modes. They are:

- **Safe Mode (SAFE):** When there is no requirement of scientific activity, the satellite is supposed to point towards Nadir direction to protect the telescope.
- **Scan Mode (SCAN):** When space observation is initiated, the space telescope should point towards Zenith direction.
- **Inertial Pointing Mode (IPM):** If any of the desired space objects is found in space, the satellite should stay stationary with respect to the inertial frame to observe the space object and take proper recordings on the scientific telescope.

From the controller design perspective, those phases are named as *controller modes* to make a distinction in the state machine, which is developed in OBC. OBC is responsible for triggering and controlling mode transitions. According to European Cooperation for Space Standardization (ECSS) [38], AOCS should be able to:

- Provide a safe state of satellite for emergency and anomaly situations,
- Make the transition from initial attitude and angular rate to final mission pointing mode,
- Ensure the attitude for mission requirements like inertial pointing to scientific targets,
- Define special attitude modes for the overall system, like attitudes for enabling communication and power input from solar panels,
- Provide intermediate attitude modes between mission phases,
- Execute orbit control maneuvers,
- Reach safe attitude and angular rate mode autonomously, in the events of anomalies,
- Trigger mode transitions by Telecommand, autonomously onboard, and failure occasions.

For this thesis work, only the attitude control system is analyzed and therefore, the orbit control system is excluded. In addition, special attitudes for communication and solar panels are excluded since there is no specification for them yet. In order to meet the remaining requirements mentioned in the list above, ACS control algorithm defines seven different modes, which are Initialization Mode, De-Tumbling Mode, Coarse Acquisition Mode, Safe Mode, Scan Mode, Inertial Pointing Mode, Fine Acquisition Mode, and Suspend Mode.

Initialization Mode (INIT): This is the mode that ACS goes in after or short before the separation from the Launch Vehicle (LV). In that mode, sensors and actuators are initialized and tested. Any problem that occurs in this state will cause ACS, and then mission failure. The state machine makes a transition to De-Tumbling Mode automatically on success.

De-Tumbling Mode (DTM): If the satellite has an angular velocity larger than the desired mode boundaries, the satellite should first damp the rotation itself and then change its mode to any other desired one. In De-Tumbling Mode, ACS system makes the transition from INIT mode to CAM mode by de-tumbling the satellite. The state machine then switches the state automatically to CAM on success conditions. Any error that occurs in this mode causes Suspend Mode entering, since if any error that cannot be handled in DTM means ACS has nothing else to recover the satellite and extraordinary measures need to be taken in fault recovery modes, which is outside the scope of the work.

Safe Mode (SAFE): The ACS needs to have Safe Mode, in which the satellite can enter and stay in it easily than other modes, for the purpose of keeping the satellite attitude under control more easily and robustly. The ACS enters SAFE from CAM, in order to align the Z-axis of Body Frame of the satellite (where the Telescope is located) to the Nadir direction. If a Telecommand with mode change command arrives, the ACS exits from Safe Mode to other nominal modes. Any error that occurs in Safe Mode results in switching back to DTM.

Scan Mode (SCAN): The ACS enters Scan Mode from Fine Acquisition Mode to have Body Frame Z-axis of the satellite is on Zenith direction. Like Safe Mode, the Telecommand can cause the exit from SCAN to SAFE or FAM mode, while an error can set it back to SAFE.

Inertial Pointing Mode (IPM): When the telescope on the satellite detects one of its target space objects in the sky, the ACS should lock itself through that object in Inertial Frame, which is defined as Inertial Pointing Mode. Like SAFE and SCAN modes, the Telecommand can cause the exit from IPM to SAFE, while any error in this mode means Safe Mode entering.

Coarse Acquisition Mode (CAM): Coarse Acquisition Mode is a transient mode of ACS. This mode can be automatically entered, when the attitude is in controllable boundaries (outside DTM boundaries) or after a Telecommand with the mode change command arrives.

Fine Acquisition Mode (FAM): ACS makes transition between IPM, SCAN, and SAFE modes with FAM. Slew mode is another nomenclature for FAM. ACS cannot automatically enter this mode and therefore, it can be entered with a Telecommand with the mode change command.

Suspend Mode (SUSP): In space missions, there might be situations that ACS cannot

handle, like low power, large angular rate, lost-in space, and so forth. These cases should be handled in Suspend Mode, in which the satellite certainly executes no control algorithms on the attitude and angular rate and simply tries to break free from the error source with debugging and collecting energy from the Sun. All the precautions and detailed analysis through spacecraft design are made, in order to avoid entering this mode during operation in space.

The Table 4.3, is the summary of ACS mode enter conditions, desired attitude control accuracy values, and components used in these modes, where magnetometer is abbreviated as MAG, gyroscope is GY, star tracker is ST, reaction wheels are RW, and magnetorquers are MT. Components to be used explicitly for momentum dumping controller, discussed in Section 5.5, were declared in the table. Figure 4.4 depicts the satellite attitude control state machine, where A stands for Autonomous onboard transition, TC is for changing state by Telecommand from the Ground Station, and E means the state change is sourced from an error that occurred.

Mode [o.5ex]	Entry Condition	Attitude Control	Components Used				
			MAG	GY	ST	RW	MT
DTM	$-$ deg 2 deg /s	$-$ deg 0.2 deg /s	X	X	-	-	X
CAM	$-$ deg 0.2 deg /s	10 deg 0.2 deg /s	MD	X	X	X	MD
FAM	5 deg 0.1 deg /s	0.2 deg 0.02 deg /s	MD	X	X	X	MD
SAFE	10 deg 0.2 deg /s	5 deg 0.1 deg /s	MD	X	X	X	MD
SCAN	2 deg 0.1 deg /s	1 deg 0.05 deg /s	MD	X	X	X	MD
IPM	0.2 deg 0.02 deg /s	0.1 deg 0.01 deg /s	MD	X	X	X	MD

Table 4.3.: Controller mode definitions (X: active usage, MD: momentum dumping)

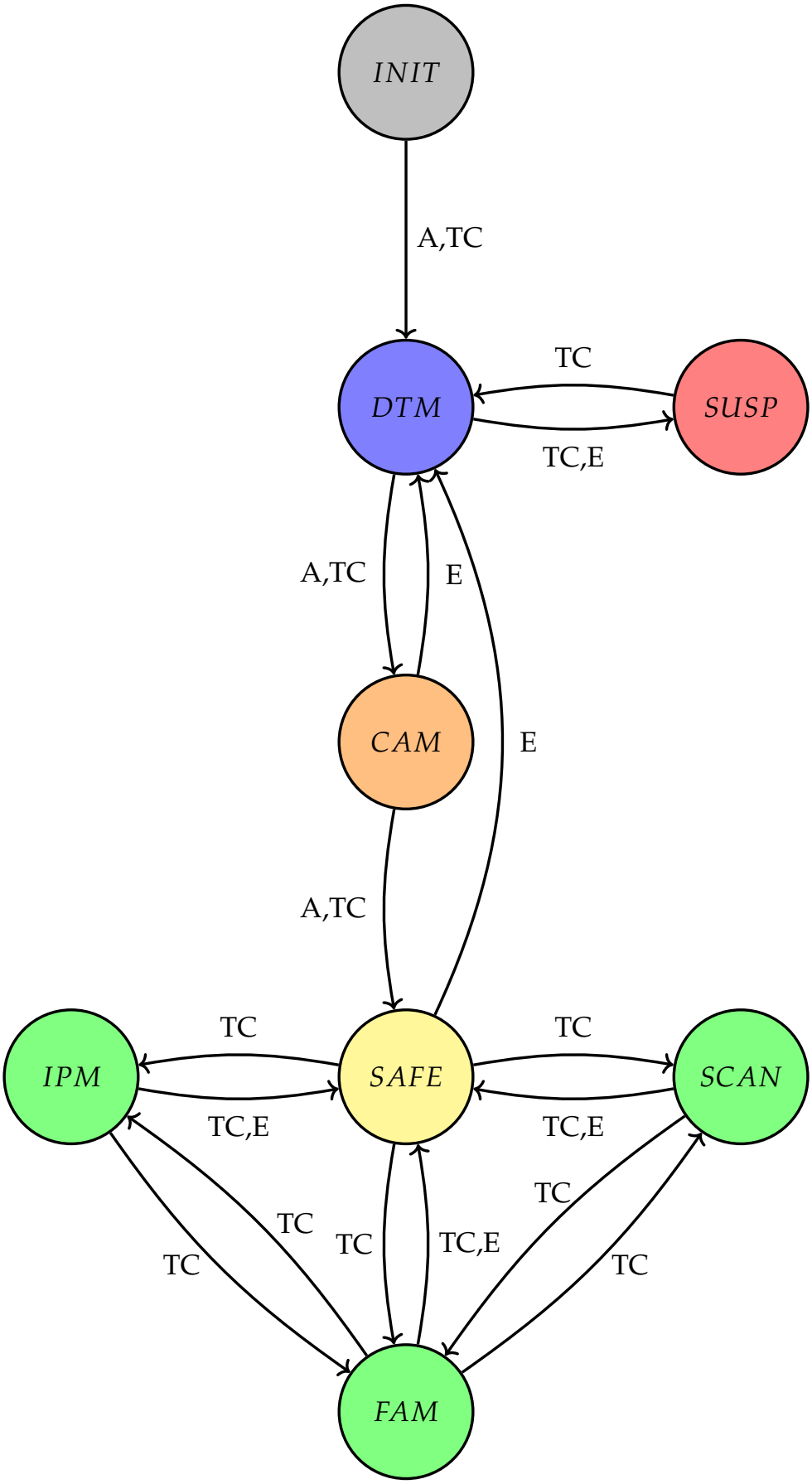

Figure 4.4.: The attitude control modes flow chart

4.3. Disturbance Analysis

The main goal of this section is to find the maximum torque and then accumulated angular momentum on each satellite body frame axis, in order to attribute causality to the selection of actuators. Wrong selection of ACS components may cause insufficient torque generation for attitude maneuvers or stabilization, reaction wheel angular momentum saturation while the satellite is operating. After the disturbance analysis, ACS actuators are selected in Section 4.4.

The disturbance torque analysis simulations are set up in Xcos environment. These simulations require Position Velocity and Time (PVT) propagator, gravity gradient, atmospheric drag, magnetic field, and magnetorquer blocks from *Spacecraft GNC Toolbox*, and attitude propagator, which generates the attitude from PVT and controller mode information.

4.3.1. Preparation

PVT Propagation

The Xcos diagram in Figure 4.5 is established for PVT propagation. This schematic is set up in Scilab 5.5.2 instead of Scilab 2023 since *Aerospace Toolbox* is incompatible with Scilab 6.0.0 onward. As a result, for orbit propagation, the generated files from the simulation are used in disturbance analysis and for the rest of the thesis work.

As seen from Equations 3.9 and 3.20, and the intuitive deduction that atmospheric density gets lower with higher altitudes, the disturbance torque generated is inversely proportional with the altitude. Thus, the minimum altitude value possible from Table 4.1, 500km selected as the mission altitude. From 2.3, in order to have the perigee point of the orbit smallest to have the worst case in disturbances, the eccentricity is taken as 0.01, the highest value on Table 4.1. Thus, using Equations 2.2 and 2.3, the perigee point of the orbit is found as 6809.3549km and the apogee point is 6946.9177km. The inclination value is calculated to make the orbit Sun-Synchronous. The starting date of the mission is arbitrarily given as 01 January 2028 00:00:01 UTC and the RAAN is calculated, to make the LTAN value at 06:00 a.m. The argument of perigee is arbitrarily zero degrees and the mean anomaly is zero degrees to start at the perigee point of the orbit.

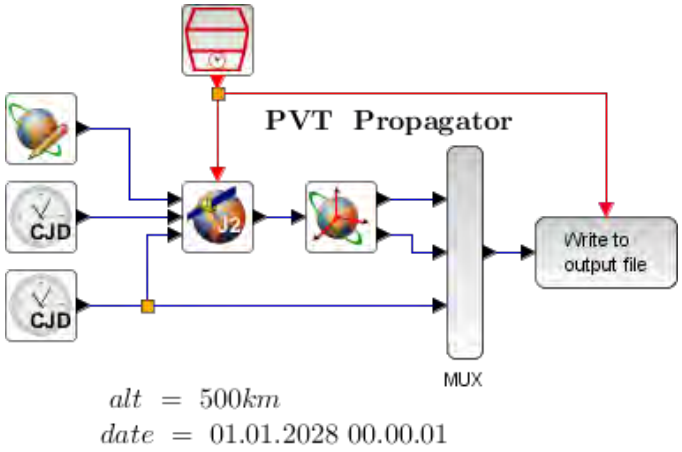

Figure 4.5.: PVT propagator block diagram

It is to be observed about PVT propagators that, the output file generated after simulating Figure 4.5 replicates the first PVT entry at the beginning. In other words, according to the generated output PVT files, the satellite starts moving along its orbit at $t = 1s$ instead of $t = 0$. This discrepancy was sourced from the Keplerian J_2 orbit propagator block of Aerospace Toolbox, which generates zero position and velocity data at the start. All of the blocks under *Spacecraft GNC Toolbox* are aware of that error and an error-handling mechanism was written for each of them. However, for the rest of this thesis work, jumps at $t = 1s$ on simulation result graphs may appear.

Attitude Propagation

For this section, a new block named "Target Attitude" was implemented, in order to generate the desired attitude, depending on the controller mode selection. The block takes ECI position, velocity vectors, selected mode, and target attitude for IPM mode as inputs, and gives the target quaternion attitude as the output. The block has no internal state and no parameter space. Inside the block, for SAFE mode, the block returns LVLH attitude related to ECI. SCAN mode simply returns the 180-degree rotation around the X axis of LVLH attitude, and IPM mode selection results in forwarding the input quaternion attitude to the output. The attitude propagator block of *Spacecraft GNC Toolbox* is shown in Figure 4.6.

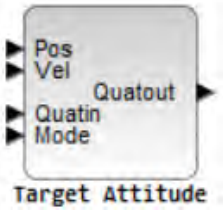

Figure 4.6.: Attitude propagator block implemented in Xcos

4.3.2. Orientation Analysis

According to Section 4.2, there are three nominal controller modes that ACS will operate: SAFE, SCAN, and IPM. This section aims to find the orientation of the satellite with respect to the ECI frame, which gives the highest overall disturbance torque. Since the target attitude of the satellite in SAFE and SCAN modes are determined by satellite position and velocity (orbital frame), the use case of orientation analysis is IPM mode. The resultant attitude of the analysis is to be used in all IPM mode worst case simulations.

The orientation analysis simulation diagram was formed in Scilab 5.5.2 and the simulation scheme is displayed in Figure 4.7. Gravity gradient and atmospheric drag blocks of *Spacecraft GNC Toolbox* are included in the simulation. However, the magnetic disturbance torque is not included because the attitude dependence of magnetic disturbances can be adjusted by adjusting the residual magnetic dipole parameter of the satellite. Intuitively, for gravity gradient torque, it might be deduced from Equation 3.9 that 45 deg deviation from nadir direction gives the maximum torque. As for atmospheric drag torque, the output torque is dependent on the vector from geometric center to the center of mass of the satellite.

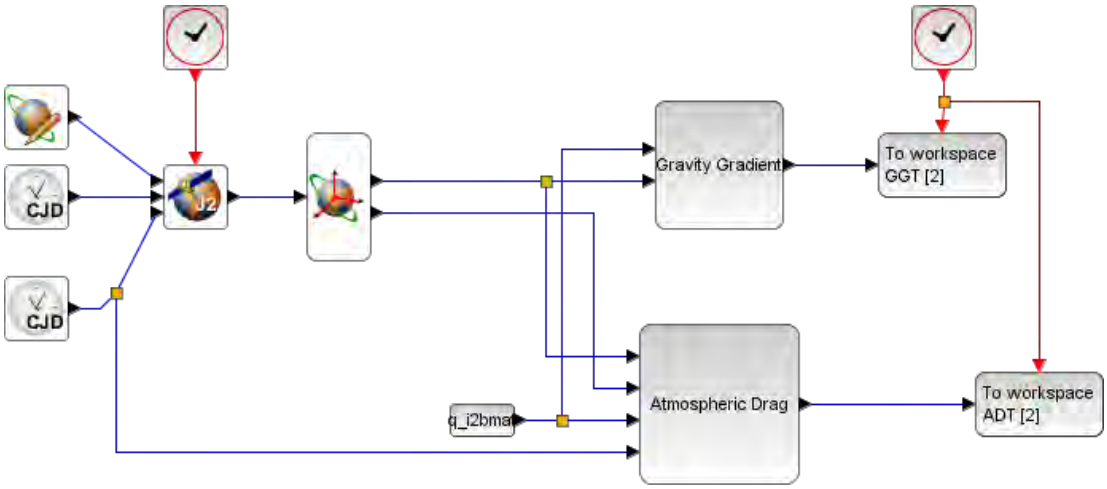

Figure 4.7.: Orientation analysis simulation block diagram

The orientation input of gravity gradient and atmospheric drag blocks are calculated by conversion from Roll-Pitch angle to quaternions. Roll angles vary from -90 deg to 90 deg by 1 deg increments and the pitch angles vary from -180 deg to 180 deg by 1 deg iterations. The moment of inertia matrix has no off-diagonal elements. Results of the simulation at Figure 4.7 are given in Figure 4.8. The orientation values that giving maximum and minimum aerodynamic and gravitational disturbance torques are given in Table 4.4.

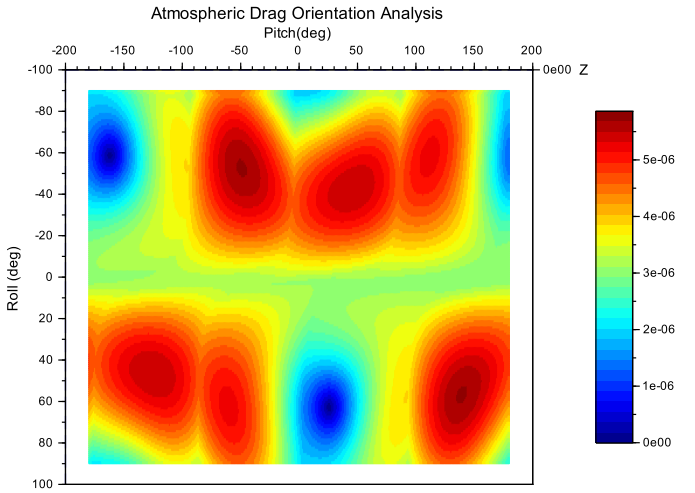

(a) Aerodynamic torque

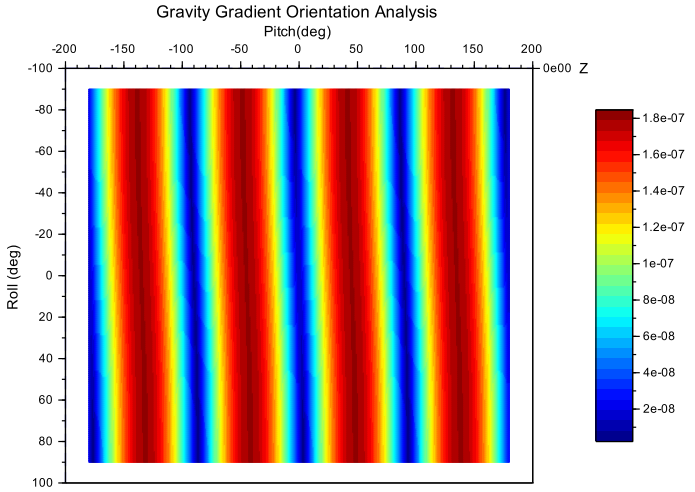

(b) Gravitational torque

Figure 4.8.: Surface plot for all Roll-Pitch attitude variations of 1 degree

Disturbance	Roll (deg)	Pitch (deg)	Torque (N.m)
Atmospheric Drag	-53 53	-49 131	5.8477×10^{-6}
Gravity Gradient	$-90, 90$	$-138, -48, 42, 132$	1.8427×10^{-7}

Table 4.4.: The orientation values w.r.t. inertial frame giving maximum disturbance torques

4.3.3. Time Analysis

According to Table 4.1, the mission start date may vary from 1st January 2028 to 31th December 2030. In order to have the worst-case disturbance values for ensuring robustness, in this section, the set of timestamps that gives the highest disturbance torque values is to be determined.

The simulation timeline can be narrowed down to the interval between 01 Jan 2028 to 01 Jan 2029, since NRLMSISE-00 is an annually periodic model and therefore, the year input is ignored in this model [4]. As for the magnetic field model, it can be considered as daily periodic, since the IGRF model gives the magnetic field vector output with respect to the ECF. That means the magnetic field of Earth daily varies related to the ECI, due to the Earth's rotation. However, this is not the case for NRLMSISE-00, since this is an empirical model and the day of the year affects the atmospheric density due to the season changes. Thus, the simulation spans the timeline from 01 Jan 2028 to 01 Jan 2029.

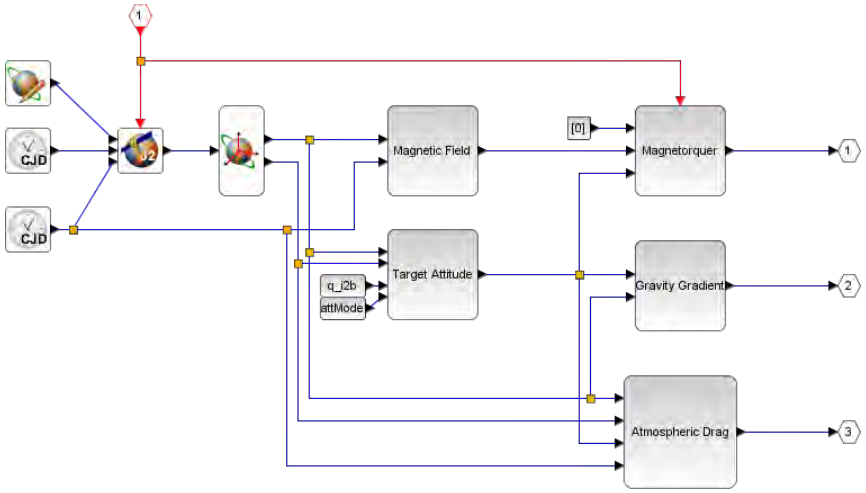

Figure 4.9.: The simulation diagram for time analysis

The yearly disturbance torque simulation was performed on Scilab 5.5.2 and the simulation layout is given in Figure 4.9. To notice, this is the layout of a superblock. The start date of the simulation is 1st January 2028 00:00:01. The time step of the simulation was 15 minutes and outside of the superblock, the norm of outputs was read and logged. The simulation diagram was run for SAFE and SCAN modes to achieve the time of year giving the maximum disturbances. As a remark, due to being independent of time, gravity gradient torque is excluded from total disturbance torque calculations of Figure 4.10 and 4.11.

The resultant plots for SAFE mode are given in Figure 4.10. As seen from Figure 4.10b

[4]For further information, please see: `https://map.nrl.navy.mil/map/pub/nrl/NRLMSIS/NRLMSISE-00/NRLMSISE-00.FOR`

and 4.10c, the magnetic disturbance is highly dominant over aerodynamic disturbances. Since magnetic disturbance is daily periodic, the result of magnetic disturbance shown in Figure 4.10c is zoomed down to have approximately 7200 minutes time span to show this periodicity. This is not the case for atmospheric drag torque. Therefore, the yearly plot is displayed. Figure 4.10b suggests three occurrences of maximum torque (one is global, two are local maximum) values that should be taken into account. These three timestamps from aerodynamic torque data are decisive in selecting timestamps for further work.

The resultant plots for SCAN mode are given in Figure 4.11. Since the SCAN mode suggests Zenith pointing Z axis of the body frame, which is the opposite direction of SAFE mode, aerodynamic and magnetic disturbance values should not differ in magnitude but direction. As a result, there is no significant difference between plots of Figure 4.10a and 4.11a, Figure 4.10c and 4.11c, and Figure 4.10b and 4.11b.

The timestamps giving the maximum overall disturbance torques as a result of the above-mentioned annual simulation are shown in Table 4.5. From this table, it can be deduced that the resultant disturbance torque values in between SAFE and SCAN mode simulations start to differ at $10^{-8} N.m$ level. These timestamps will be taken into account by selecting the mission start date of SAFE, SCAN, and IPM mode simulations.

Mode	Timestamp (UTC)	Disturbance Torque (N.m)
SAFE	9th April 2028 08:20:00	3.70044×10^{-5}
SAFE	26th September 2028 08:15:00	3.68025×10^{-5}
SAFE	9th November 2028 07:35:00	3.68757×10^{-5}
SCAN	9th April 2028 08:20:00	3.70061×10^{-5}
SCAN	26th September 2028 08:15:00	3.68027×10^{-5}
SCAN	9th November 2028 07:35:00	3.68794×10^{-5}

Table 4.5.: Timestamps giving maximum disturbance torque values

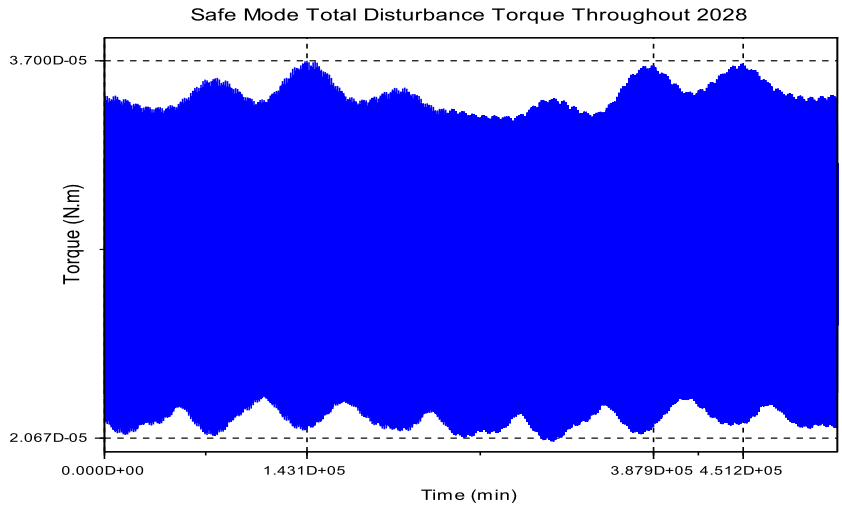

(a) Total disturbance

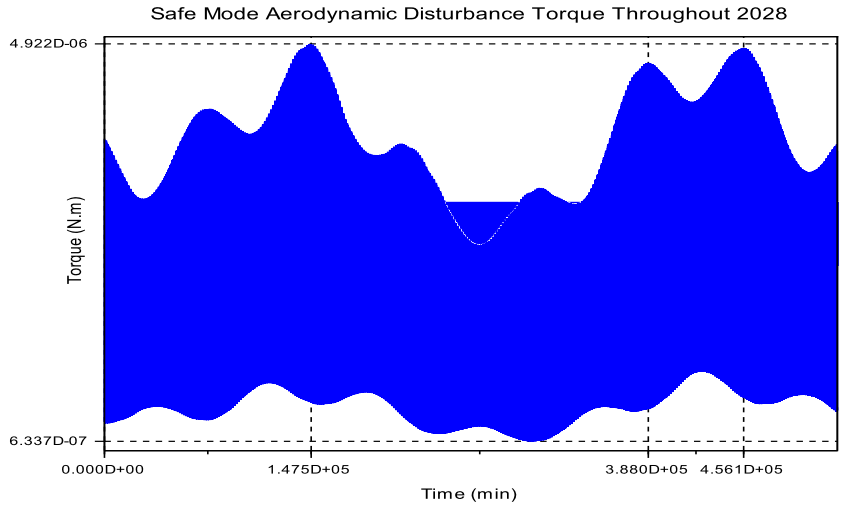

(b) Aerodynamic disturbance

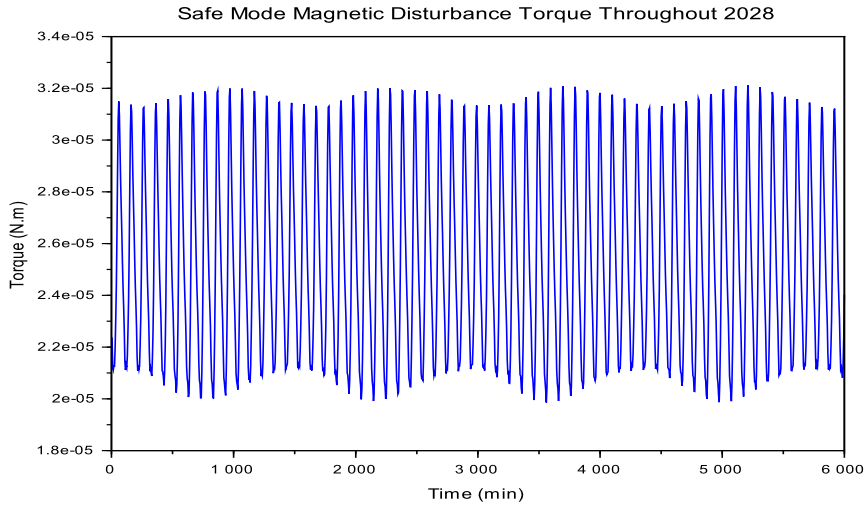

(c) Magnetic disturbance

Figure 4.10.: SAFE mode disturbance torque magnitude plots throughout 2028

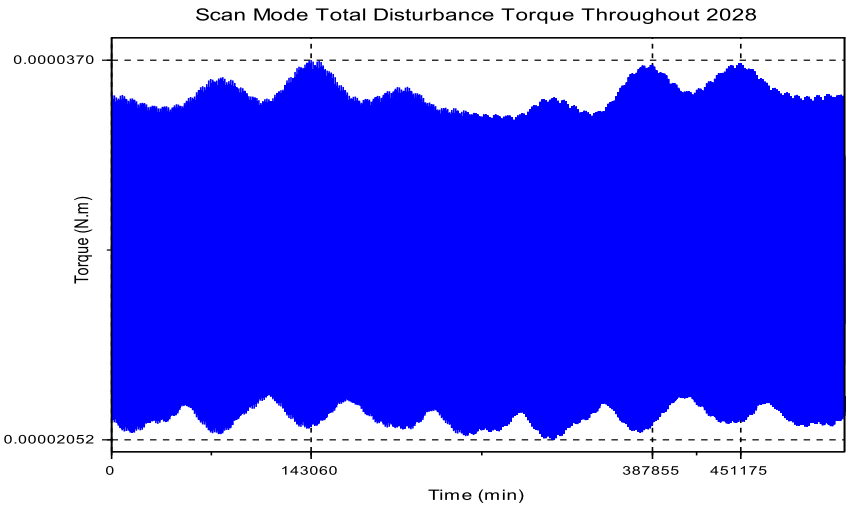

(a) Total disturbance

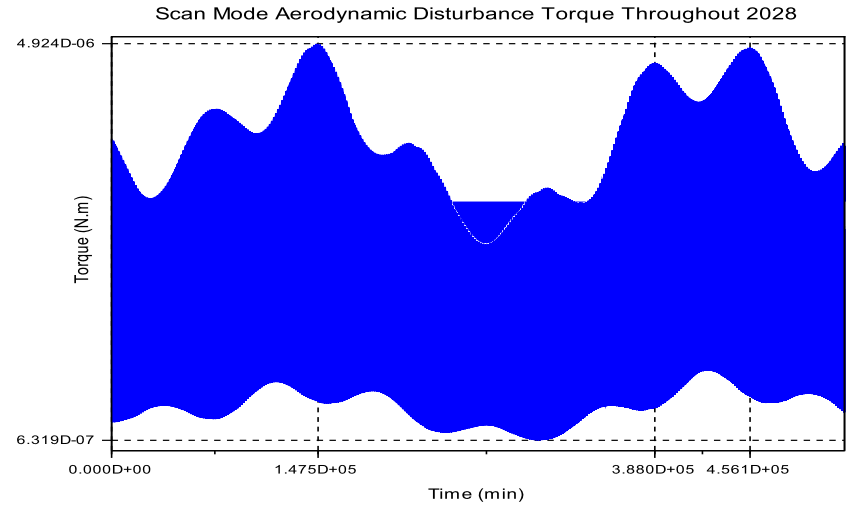

(b) Aerodynamic disturbance

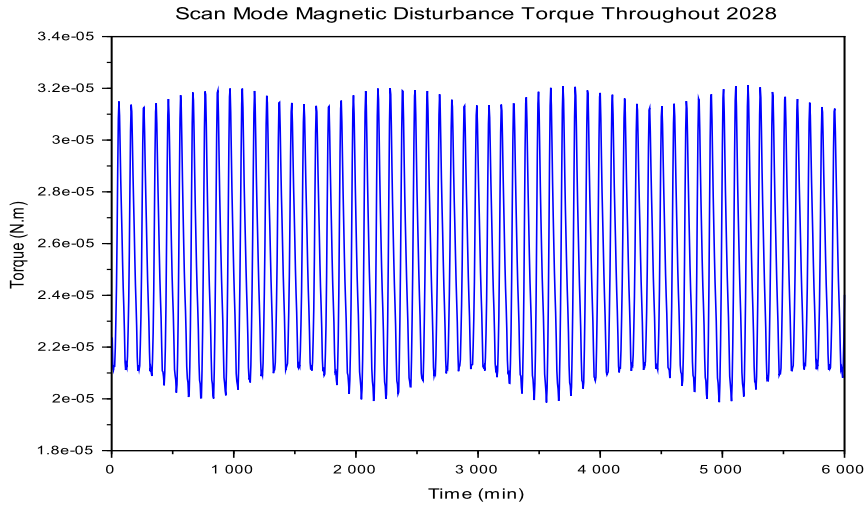

(c) Magnetic disturbance

Figure 4.11.: SCAN mode disturbance torque magnitude plots throughout 2028

4.3.4. Orbit Analysis

The Xcos diagram in Figure 4.12 was formed, in order to estimate the maximum disturbance torque and accumulated angular momentum throughout a single orbit for three nominal controller modes, SAFE, SCAN, and IPM. This diagram utilizes PVT and attitude propagators mentioned in Section 4.3.1. The input file at the leftmost block is taken from the output of the diagram at Figure 4.5 to obtain PVT information of the satellite. The accumulated angular momentum on each axis on the Body Frame is calculated by taking the integral of total disturbance torque. The simulation parameters of the simulation at Figure 4.12 for all three modes (SAFE, SCAN, and IPM) are given in Table 4.6.

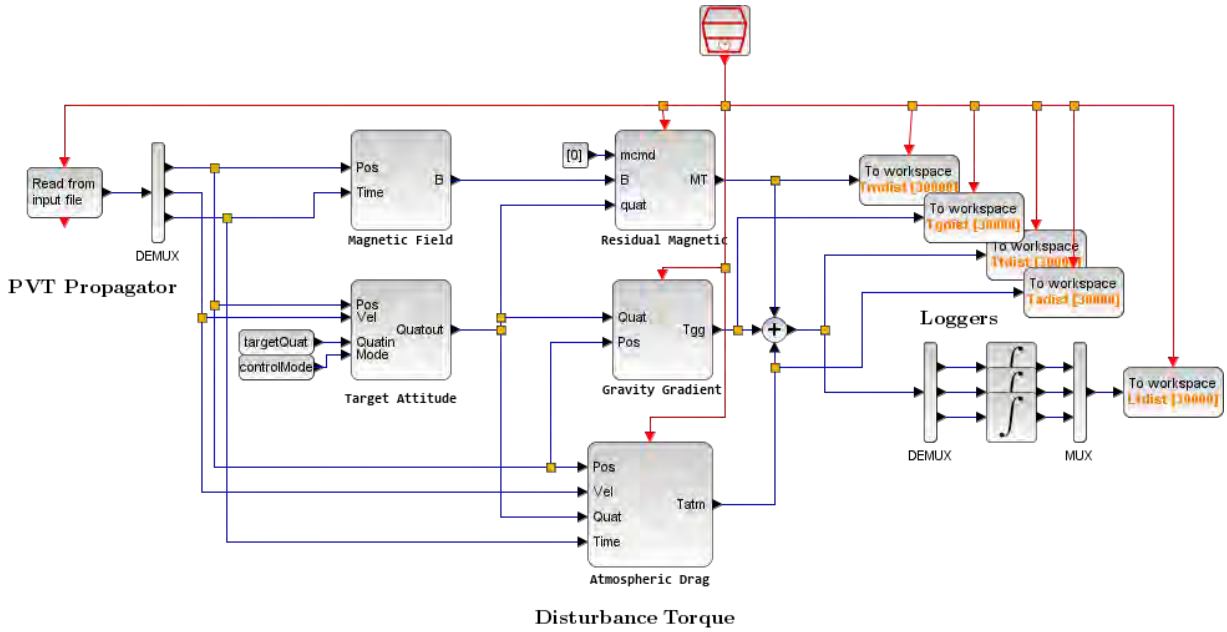

Figure 4.12.: Disturbance torque generator block diagram

The mission start date value in Table 4.6 was selected regarding the time in 2028 giving maximum disturbance torque, found in Table 4.5. As Equations 3.9 and 3.20 suggest, gravitational and magnetic disturbances decrease with increasing altitude. Hence, the minimum altitude possible in Table 4.1 was selected, $500km$. The simulation frequency was selected arbitrarily while trying to reduce the simulation time elapsed as much as possible without sacrificing the output accuracy and sanity. The moment of inertia matrix was selected non-diagonal so that the gravity gradient torque will not give zero output in SAFE and SCAN modes, since the target attitude of both modes has Z-axis aligned to the Earth Nadir-Zenith line. J_2 effect on gravity gradient torque was disabled, for the reasons mentioned in Section 4.3.5.

As for atmospheric drag block, all satellite-related parameters were taken from Table 4.2, and the atmospheric density model was selected as NRLMSISE-00. Apart from position

and time information, this model requires the Solar radio flux at 10.7 cm wavelength and magnetic index values [39]. Since magnetic index (AP) is not significant for heights above 80km [39], the default value was assigned to this parameter. However, F10.7 and its average F10.7A parameters are very decisive on the resultant density value. Therefore, these parameters have to be taken from NOAA Space Weather Prediction Center website [5]. Figure A.1 displays the graph, which was directly downloaded from the website and it has the prediction value of Solar cycle F10.7 cm Radio Flux between 2028 and 2030. In order to make the controller more robust against changes in atmospheric drag torque, the highest value from A.1 with margin, 200, was assigned to the atmospheric drag block F107 and F107A parameters.

Block Name	Parameter	Value	Unit
-	Start Date	9th April 2028 08:00:00	UTC+00
-	Altitude	500	km
-	Simulation Frequency	1	Hz
-	Target Attitude Input for IPM (targetQuat in Figure 4.12)	$\begin{bmatrix} 0.8159672 \\ -0.4068262 \\ -0.3675664 \\ 0.1832619 \end{bmatrix}$	Quaternion (real part first)
Gravity Gradient	Moment of Inertia	$\begin{bmatrix} 1.67 & 0.16 & 0.16 \\ 0.16 & 1.6 & 0.16 \\ 0.16 & 0.16 & 1.57 \end{bmatrix}$	$kg.m^2$
Gravity Gradient	J_2 Enable	No	-
Residual Magnetic	Satellite Residual Magnetic Dipole Moment	$\begin{bmatrix} 0 & 0 & 1 \end{bmatrix}^T$	$A.m^2$
Magnetic Field	Density Model	IGRF-13	-
Atmospheric Drag	Density Model	NRLMSISE-00	-
Atmospheric Drag	81 Day Avg. F10.7 Flux (F107A)	200	m^2Hz
Atmospheric Drag	Daily F10.7 Flux for the Previous Day (F107)	200	m^2Hz
Atmospheric Drag	Satellite Drag Coefficient	2.4	-
Atmospheric Drag	Satellite Cube Edge Length	60	cm
Atmospheric Drag	Satellite Geometric Center Coordinates w.r.t. Body Frame	$\begin{bmatrix} 2 & 3 & -5 \end{bmatrix}^T$	cm

Table 4.6.: Disturbance analysis simulation parameters

The resultant disturbance torque plots are shown in Figure 4.13a, 4.13b, 4.13c, and 4.13d. Figure 4.13b, 4.13c, and 4.13d imply that magnetic disturbance torque dominates aerodynamic and gravitational torque and it is the biggest at the IPM simulation. The highest aerodynamic torque observed in Figure 4.13c belongs to IPM. This is an expected result because the attitude giving the maximum aerodynamic torque was determined in Section 4.3.2 and the attitude was taken from 4.4. The gravity gradient torque is at the highest in SAFE and SCAN modes, since the deviation from principal moment of inertia becomes the most apparent in Nadir or Zenith pointing modes. From those figures, it might be inferred that all disturbance torques are periodical within the orbital period.

[5]Please refer: `https://www.swpc.noaa.gov/products/solar-cycle-progression`

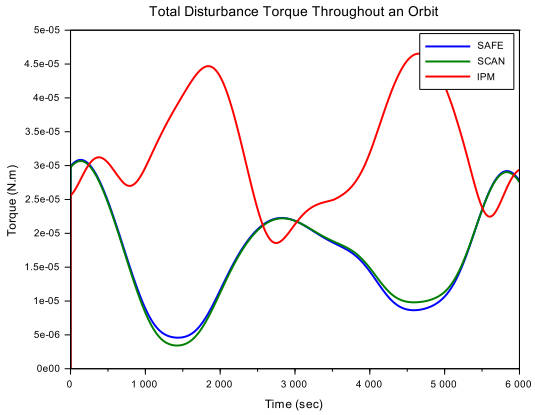

(a) Overall disturbance torque

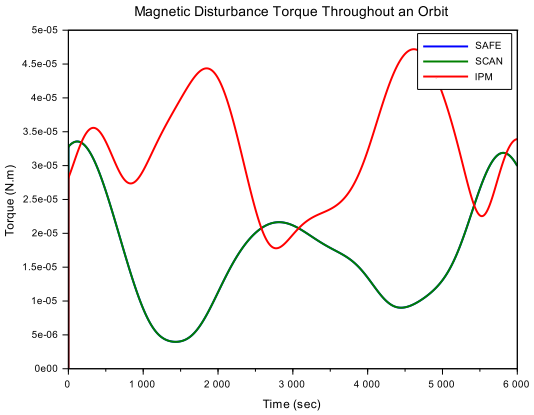

(b) Magnetic disturbance torque

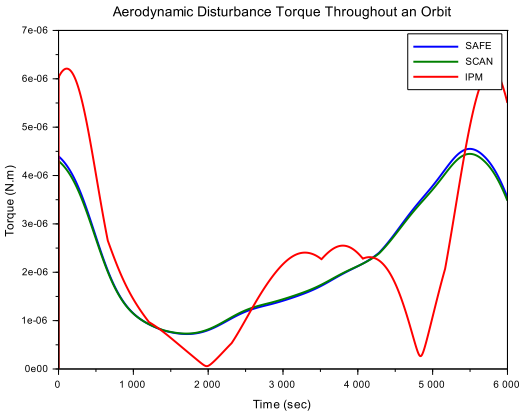

(c) Aerodynamic disturbance torque

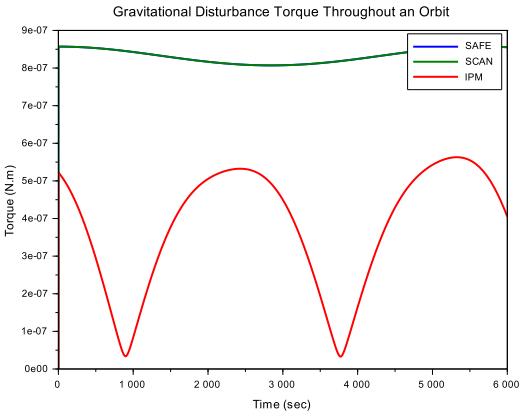

(d) Gravitational disturbance torque

Figure 4.13.: Disturbance torque breakdown of the satellite throughout an orbit for three nominal controller modes

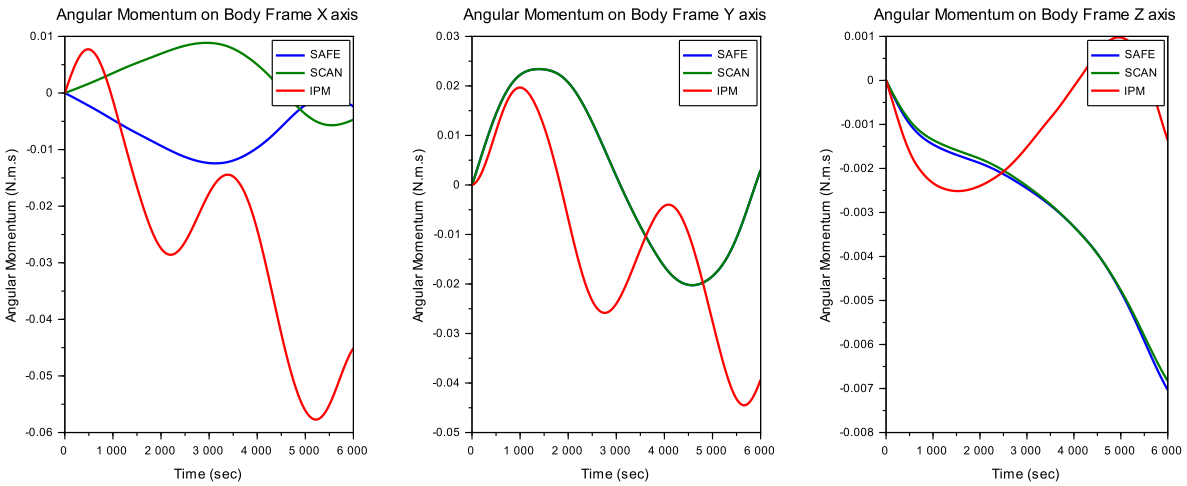

Figure 4.14.: Accumulated angular momentum on Body Frame axes

The resultant accumulated angular momentum on three Body Frame axes can be seen in Figure 4.14. Figure 4.14 implies that the angular momentum value of SAFE mode has the opposite sign from SCAN mode since the Zenith pointing frame was generated the $180deg$ rotation on X axis of Nadir pointing frame. From these figures, the highest angular momentum accumulated appears at IPM mode X axis.

To conclude this section, the maximum disturbance torque and accumulated angular momentum on a single axis values are given in Table 4.7 analyzing Figure 4.13a and 4.14. These values will be helpful in the selection of ACS actuators.

Symbol	Name	Maximum Value
$T_{d_{max}}$	Maximum Torque	$4.653 \times 10^{-5} N.m$
$H_{d_{max}}$	Maximum Accumulated Angular Momentum	$5.770 \times 10^{-2} N.m.s$

Table 4.7.: The maximum disturbance torque and accumulated angular values

4.3.5. Effect of Non-Principal Moment of Inertia and J_2 Perturbation over Disturbances

During disturbance analysis simulations, the effect of the non-principal moment of inertia and J_2 perturbation on the simulation were investigated as well. The analysis was made on SAFE mode only, since the effect of these factors becomes apparent as gravitational disturbance analysis, which is zero when the symmetry axis is showing Nadir or Zenith direction. Because Nadir and Zenith are on the same line with opposite directions, only the Nadir pointing mode, which is SAFE mode is to be analyzed.

The resultant plots are given in Figure 4.15. In Figure 4.15b, it can be seen that having a principal moment of inertia resulted in zero gravity gradient torque, since at the SAFE mode, the satellite Z axis points towards Nadir direction. Making moment of inertia non-primary introduced disturbance, since in that case the primary Z axis no longer points Nadir direction. Adding J_2 perturbation to the non-primary moment of inertia case made a slight difference. According to Figure 4.15c, having a non-primary moment of inertia increased the accumulated angular momentum in all axes and introduced nonzero angular momentum on the Z axis. Introducing J_2 had very little effect. As a result, as Equation 3.12 has a certain computational cost and makes very slight differences, the J_2 effect is disabled for this thesis work.

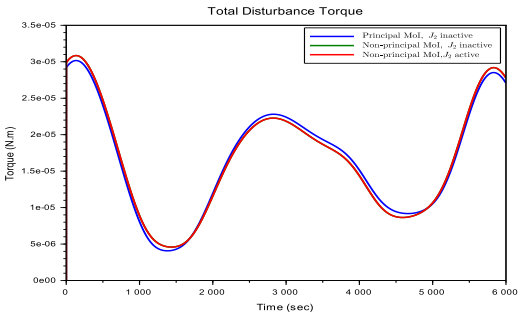

(a) Total disturbance torque

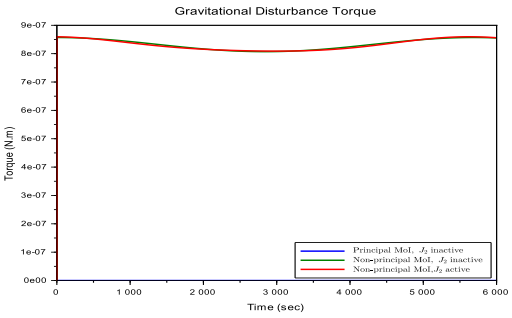

(b) Gravity gradient disturbance torque

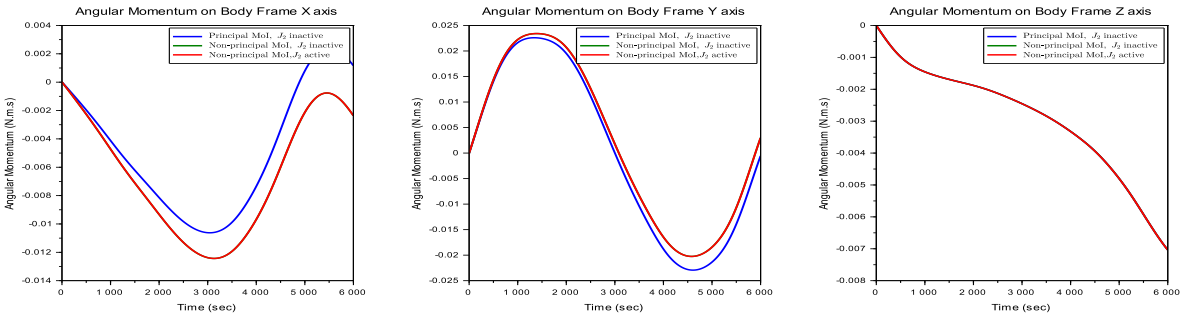

(c) Accumulated angular momentum on Body Frame axes

Figure 4.15.: Disturbance plots for the demonstration of non-principal moment of inertia and J_2 perturbation effects

4.4. Component Selection

4.4.1. Satellite Dispenser

In the INIT mode definition under Section 4.2, it is stated that ACS should perform initial tests, calibrations, and hardware configurations, before the separation from the Launch Vehicle. The separation is executed securely, with the help of specialized satellite dispenser hardware. Due to unexpected imbalances of the satellite and the separation unit, the separation may impose nondeterministic angular velocity to satellite ACS, at the beginning of its operation, which is named as tip-off rate, The maximum tip-off rate is provided by the dispenser manufacturers as a specification. For this thesis work, by taking the physical and mechanical properties of the satellite given in Table 4.2 into account, Carbonix of ExoLaunch was found to be suitable for the application, especially due to having relatively low tip-off velocity ($2 deg/s$) [40]. As a tiny notice, the inner diameter of the dispenser is $54.5 cm$ [40], which is below the edge length of the cube shape of the satellite ($60 cm$), according to Table 4.2. Thus, instead of the off-the-shelf Carbonix separator, its tailored versions could be utilized. One example of Carbonix-24 was shown in Figure 4.16.

Source: https://exolaunch.com

Figure 4.16.: CARBONIX-24 of Exolaunch

4.4.2. Magnetometer

The role of magnetometer in ACS is de-tumbling the satellite after triggering DTM mode and momentum dumping, as Table 4.3 suggests. As discussed in Section 4.2, in De-Tumbling Mode, the satellite has an angular velocity exceeding the star tracker's maximum angular rate for measurement threshold, and therefore, star trackers are disabled. Then gyroscopes and magnetometers are the remaining sensors for the determination of the angular speed vector and the magnetic field vector to counteract the angular speed vector. As for momentum unloading, after measuring angular momentum on reaction wheels, the magnetometer is used to determine the counteracting vector for magnetorquers. Under these circumstances, the sensor accuracy and noise are the most significant factors, when selecting the magnetometer. More inaccuracy on magnetometers may lead to late de-tumbling of the satellite in DTM mode and larger steady-state error in momentum dumping.

Table 4.8 lists off-the-shelf magnetometers on the market. Fluxgate magnetometers have higher accuracy than AMR ones, nevertheless, accuracy at this level is not required for the satellite. Moreover, fluxgate magnetometers draw more weight budget than other alternatives and require additional circuitry for analog to digital conversion. From Figure 4.10c and 4.11c, the maximum magnetic disturbance torque magnitude measured is $3.2 \times 10^{-5} \mu T$, with the magnetic dipole of $1 A.m^2$. In light of this information, among magnetometer models in Table 4.8, AMR magnetometer of Zarm Technik AG is selected for the design since it is lightweight, has enough accuracy to operate in the simulated magnetic field, and output rate is suitable for de-tumbling the satellite [41]. The line in Table 4.8 having this magnetometer was filled with green.

Brand	Model	Type	Accuracy (μT)	Range (μT)	Output Rate (Hz)	Weight (g)
AAC Clyde [6]	MAG-3	Fluxgate	Analog	100	Analog	100
AAC Clyde [7]	MM200	Classical	-	800	500	12
Astrofein [8]	ACM	Classical	2.28×10^{-4}	60	-	280
CubeSpace [9]	Gen2 CubeMag	Classical	0.05	-[10]	5	16
NSS [11]	NMRM-Bn250485	AMR	0.008	60	25	85
ZARM Technik AG [41]	FGM	Fluxgate	64	10^{-4}	[12] 50	250
ZARM Technik AG [41]	AMR	AMR	0.01	250	240	55

Table 4.8.: Magnetometers on the market

[6] Please see: https://www.aac-clyde.space/what-we-do/space-products-components/adcs/mag-3

[7] Please see: https://www.aac-clyde.space/what-we-do/space-products-components/adcs/mm200

[8] Please see: https://www.astrofein.com/astrofein-acm-magnetometer/

[9] Please see: https://www.cubespace.co.za/products/gen-2/sensors/cubemag/

[10] Strong assumption: The range of the sensor encompasses Earth magnetic field.

[11] Please see: https://www.newspacesystems.com/wp-content/uploads/2022/07/NewSpace-Magnetometer_V11.2.pdf

[12] $3dB$ cut-off frequency

4.4.3. Gyroscope

Table 4.3 shows that Gyroscope is used in all operational controller modes of ACS. The main necessity of a gyroscope is to measure the angular rate in operation without reaching the saturation region. According to Table 4.3, the maximum rotation speed is caused by tip-off rotation speed in DTM. As for other modes, the IPM has the most precise angular rate control requirement, which equals to $0.01\,\mathrm{deg} = 36 arcsec/s$, and therefore, the desired gyroscope should have higher accuracy than it. Note that, most inertial measurement units come with switchable measurement range and accuracy at the runtime.

Table 4.9 is filled with off-the-shelf gyroscopes on the market. Instead of accuracy, the bias instability parameter is put as a merit of quality because this sensor will output angular rate to attitude determination block and bias instability parameter is the measure of how accurate the attitude determination can estimate the bias of the gyroscope [42]. In other words, the angular rate measurement might not have more accuracy than the bias instability value [42].

According to the above-mentioned requirements and Table 4.9, CRH03-010 of Silicon Sensing is selected for the design because of its high accuracy parameters [43]. If other factors prevail over the accuracy, like Technology Readiness Level (TRL) or radiation endurability, SAFRAN STIM277H might be considered as an alternative to it, while trading off accuracy [44]. The selected gyroscope was filled with green and the alternative was filled with yellow in Table 4.9.

Brand	Model	Type	Bias Instability (deg /h, 1σ)	ARW (deg /h)	Range (deg /s)	Bandwidth (Hz)	Weight (g)	Power (W)
SAFRAN [13]	STIM202	MEMS	0.4	0.17	400	262	55	1.2
SAFRAN [44]	STIM277H	MEMS	0.3	0.15	400	262	52	1.2
Silicon Sensing [14]	CRS43-02	MEMS	12	-	100	24	26	0.13
Silicon Sensing [15]	CRS09A-02	MEMS	3	0.1	100	30	60	0.5
Silicon Sensing [43]	CRH03-010	MEMS	0.03	0.005	10	50	42	0.02
VectorNav [16]	VN-110 (AHRS)	MEMS	1	5	490	240	125	2

Table 4.9.: Gyroscopes on the market

[13] Please see: https://www.sensonor.com/products/gyro-modules/stim202
[14] Please see: https://www.siliconsensing.com/products/gyroscopes/crs43/
[15] Please see: https://www.siliconsensing.com/products/gyroscopes/crs09a/
[16] Please see: https://www.vectornav.com/products/detail/vn-110

4.4.4. Star Tracker

Star tracker is the only source of attitude measurement in the ACS design. According to Table 4.3, this sensor is activated in all operational controller modes, except DTM mode. As Section 3.3.1 expresses, high angular rates may disrupt measurements and therefore, all star trackers have angular rate limits for taking attitude measurements. ACS waits for the decrease in the angular rate of the satellite until reaching the interval, where star trackers might be activated.

Table 4.3 suggests that IPM is the most precise mode and it requires 0.1 deg $=$ 360 *arcsec* accuracy with 0.01 deg $/s$. Table 4.10 gives the specifications of star trackers on the space market, whose accuracy values are close to 360 *arcsec*. As the table indicates, all star trackers inside the table are suitable for the application, however, in a practical sense, the sensor noise should be less than ten percent of desired accuracy and is preferred to have control algorithms with less fluctuation around the target attitude. Therefore, AAC Clyde ST400 was chosen, due to its high accuracy [45]. The line on Table 4.10 contains AAC Clyde ST400 is filled with green.

Brand	Model	Max. Slew Rate(deg/s)	Cross accuracy (*arcsec*)	Twist accuracy (*arcsec*)	Weight (g)	Power (W)
AAC Clyde [17]	ST200	0.3	30	200	42	0.7
AAC Clyde [45]	ST400	0.5	10	120	280	0.7
CubeSpace [18]	Gen2 CubeStar	0.3	72	216	47	0.165
Vectronic Aerospace [19]	VST-41M	-	18	122	800	2.5

Table 4.10.: Star trackers on the market

[17] Please see: `https://www.aac-clyde.space/what-we-do/space-products-components/adcs/st200`

[18] Please see: `https://www.cubespace.co.za/products/gen-2/sensors/cubestar/`

[19] Please see: `https://www.vectronic-aerospace.com/star-trackers/`

4.4.5. Reaction Wheel

Wertz states that reaction wheels are used for absorbing periodic disturbance torques and executing attitude maneuvers [12]. However, non-cyclic disturbance torques cause accumulation of angular momentum on reaction wheels in time, and therefore, the accumulated momentum is dumped through external torquers, like thrusters or magnetorquers [12]. The main objective of this section is to select reaction wheels so that wheels have the capability of angular momentum accumulation due to disturbances and at the same time, executing attitude slews in an orbital period. The maximum accumulated angular momentum on body frame axes was already calculated in Section 4.3 and the results were collected under Table 4.7. The only missing part for ACS reaction wheel selection is attitude maneuver capability.

The required attitude maneuver competence of reaction wheels is tested in two steps: Bang-Bang and then Bang-Drift-Bang analyses. The former is the harshest maneuver condition that a reaction wheel could experience because the operating point of the wheel is at its physical torque and angular momentum limits, throughout the slew motion. Since this is not physically possible for reaction wheels on the market, a more realistic approach, Bang-Drift-Bang analysis is conducted. As a practical requirement, considering the orbital period around 5500sec, it is feasible for reaction wheels to complete a single 180 deg rotation in 500sec, while accumulating angular momentum because of disturbance torques.

Bang-Bang Analysis

In this analysis, the wheel exerts its positive maximum torque to rotate around its rotation axis, until it reaches 90 degrees rotation from the initial state. Then, it applies negative maximum torque immediately to dampen the angular momentum accumulated due to the slew and complete the rotation at 180 degrees with zero angular velocity. This analysis aims to be the first iteration of analysis to determine at which range of angular momentum and torque parameters of reaction wheels would be searched on the market.

Equation 4.1 gives the relation between the angular velocity and torque, through angular momentum equations, where H_{smax} is the maximum angular momentum required for the slew motion, T_{smax} is the maximum torque required for the slew, I is the moment of inertia matrix of the satellite, and t_1 is the half-slew time. Equation 4.2 gives the rotation angle around single axis, θ. Then, Equations 4.3 and 4.4 might be obtained. The illustration of the Bang-Bang slew of the reaction wheel is displayed in Figure 4.17.

$$H_{smax} = I\omega_{max} = \int_0^{t_1} T_{smax}\, dt = T_{smax} t_1 \tag{4.1}$$

$$\theta = \int_0^{t_1} \omega_{max}\, dt = \frac{1}{2}\frac{T_{smax}}{I} t_1^2 = \frac{\pi}{2} \tag{4.2}$$

$$H_{smax} = \frac{\pi I}{t_1} \tag{4.3}$$

$$T_{smax} = \frac{\pi I}{t_1^2} \tag{4.4}$$

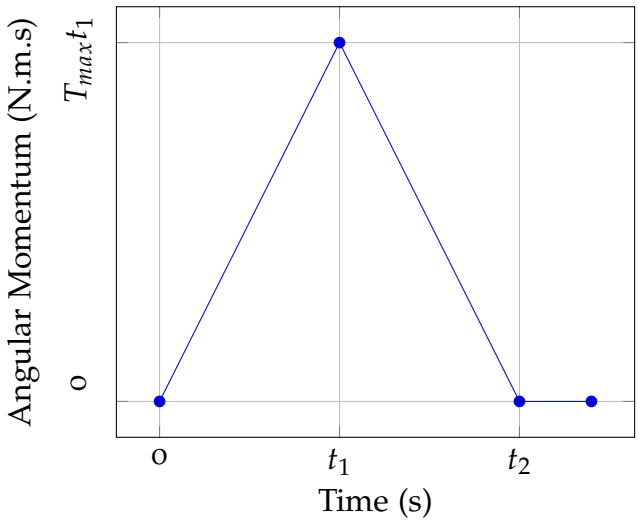

Figure 4.17.: Angular momentum of a single reaction wheel executing Bang-Bang maneuver

From Section 4.1, the maximum diagonal component of the moment of inertia matrix is the $1.67 kg.m^2$. The vector addition of %10 variation sourced from the off-diagonal elements gives $1.678 kg.m^2$. If the desired slew time to complete the 180 deg rotation is $500 sec$, t_1 should be $250 sec$. From Equation 4.3 and 4.4, the required angular momentum and torque for Bang-Bang slew could be found.

$$T_{smax} = 8.434 \times 10^{-5}\ N.m \tag{4.5}$$

$$H_{smax} = 2.108 \times 10^{-2}\ N.m.s \tag{4.6}$$

Then, the maximum disturbance torque, T_{max}, and the maximum accumulated angular momentum along the orbit, H_{max}, might be calculated by importing maximum disturbance torque and angular momentum values from Table 4.7.

$$T_{max} = T_{smax} + T_{d_{max}} = 1.308 \times 10^{-4} N.m \tag{4.7}$$

$$H_{max} = H_{smax} + H_{d_{max}} = 7.878 \times 10^{-2} N.m.s \tag{4.8}$$

Bang-Drift-Bang Analysis and Selection

Using the values from Equation 4.7 and 4.8, the reaction wheel market survey was carried out and Table 4.11 was formed. Although the Bang-Bang analysis gives results for the harshest environment and slew conditions, it does not comply with the reaction wheels on the market. Those wheels reach their angular momentum capacity much earlier than 250*sec*. Therefore, as indicated in Section 3.3.4, wheels may not exert any torque after reaching the angular momentum capacity. This is named drift rotation.

Brand	Model	Max. Torque (mN.m)	Ang. Mom. Cap. (mN.m.s)	Saturation Time (s)	Power (W)	Weight (g)
Astrofein [20]	RW35	5	100	20	2	500
Blue Canyon Tech [46]	RWp100	6	100	16.666	0.81	330
CubeSpace [21]	Gen2 CW1200	20	120	6	4.7	450
Vectronic Aerospace [22]	VRW-B-02	20	200	10	4.5	1

Table 4.11.: Reaction wheels on the market

Figure 4.18 depicts the time plot of angular momentum on a reaction wheel executing bang-drift-bang rotation. In this graph, t_1 is the wheel angular momentum saturation time and t_2 is the half-slew time.

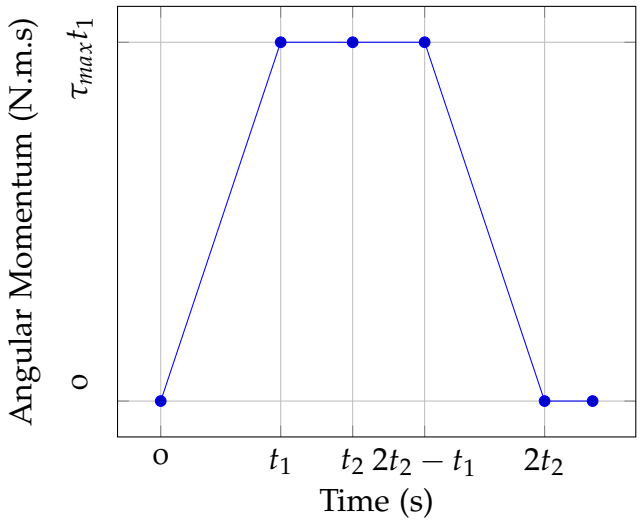

Figure 4.18.: Angular momentum of a single reaction wheel executing Bang-Drift-Bang maneuver

Equation 4.1 might be rewritten as Equation 4.9. Then, the addition of the above-mentioned drift motion to Equation 4.2 brings out Equation 4.10.

[20]Please see: `https://www.astrofein.com/reaktionsraeder/rw35/`
[21]Please see: `https://www.cubespace.co.za/products/gen-2/actuators/cubewheel/`
[22]Please see: `https://www.vectronic-aerospace.com/reaction-wheels/`

$$\omega_{max} = \int_0^{t_1} \frac{T_{smax}}{I} dt = \frac{T_{smax} t_1}{I} \tag{4.9}$$

$$\theta = \int_0^{t_1} \omega \, dt + \int_{t_1}^{t_2} \omega_{max} dt \tag{4.10}$$

The combination of Equation 4.2 and 4.9 gives the inequality at Equation 4.16, which shows the relation between t_1 and H_{smax}.

$$\frac{\pi}{2} = \frac{1}{2}\frac{T_{smax}}{I} t_1^2 + \frac{H_{smax}}{I}(t_2 - t_1) \tag{4.11}$$

$$\pi I = T_{smax} t_1^2 + 2H_{smax}(t_2 - t_1) \tag{4.12}$$

$$\pi I = 2T_{smax} t_1 t_2 - T_{smax} t_1^2 \tag{4.13}$$

$$\pi I = H_{smax}(2t_2 - t_1) \tag{4.14}$$

$$2t_2 = 500sec > \frac{\pi I}{H_{smax}} + t_1 \tag{4.15}$$

$$H_{smax} > \frac{\pi I}{500 - t_1} \tag{4.16}$$

In order to have the worst case angular momentum capacity, the maximum value of t_1 is to be assigned in Equation 4.16. From Table 4.11, the maximum t_1 value is 20 sec (Astrofein RW35). Then, the minimum angular momentum capacity requirement for the slew could be found. The inclusion of maximum disturbance torque and angular momentum values from Table 4.7 gives the minimum value of the angular momentum capacity of the wheel in Equation 4.18.

$$H_{smax} > \frac{\pi I}{500 - 20} = 1.098 \times 10^{-2} \; N.m.s \tag{4.17}$$

$$H_{max} = H_{smax} + H_{dmax} = 6.868 \times 10^{-2} \; N.m.s \tag{4.18}$$

All of the four reaction wheel models in Table 4.11 are capable of enduring disturbances throughout an orbit while executing the harshest slew maneuvers. From Table 4.11, the reaction wheel having the least power consumption and weight, Blue Canyon Tech RWp100, was selected, whose line is painted green in the table. Then, the actual slew time of the selected wheel may be found by giving the parameters of the selected reaction wheel to Equation 4.11, which might be rewritten as Equation 4.19. In Equation 4.20, after importing the maximum disturbance torque and angular momentum values from Table 4.7, the slew time of the wheel under disturbances was found as $118.863sec$. As a result, it might be inferred that the reaction wheel matches the design criteria.

$$\frac{\pi}{2} = \frac{1}{2}\frac{T_{rw} - T_{d_{max}}}{I} t_1^2 + \frac{H_{rw} - H_{d_{max}}}{I}(t_2 - t_1) \tag{4.19}$$

$$\rightarrow t_s = \frac{2I}{H_{rw} - H_{d_{max}}} \left(\frac{\pi}{2} - \frac{1}{2}\frac{T_{rw} - T_{d_{max}}}{I} t_1^2 \right) + 2t_1 = 118.863sec \tag{4.20}$$

4.4.6. Magnetorquer

Table 4.3 suggests that, other than DTM mode, the main function of magnetorquers is momentum dumping. They should reduce the angular momentum accumulated in reaction wheels in a single orbit duration at most. According to Section 4.3.4, the largest portion of disturbance torque is sourced from Earth's magnetic field, in comparison to atmospheric drag and gravity gradient torques. The maximum satellite residual magnetic dipole moment is declared as $1A.m^2$ in Table 4.2. Therefore, the selection of magnetorquers having a maximum dipole moment value of at least $1A.m^2$ provides the system to compensate for the majority of instantaneous disturbance torques almost in a second.

It is to be observed that, magnetorquers need to be deactivated, in order to allocate time slots for magnetometer measurements without disruption. As a result, the minimum value of magnetic dipole moment as a requirement is doubled to $2A.m^2$, which ensures the generation of counter-acting magnetic torque against disturbance torques while enabling at most half-time slots for magnetometer measurements.

Table 4.12 contains information about magnetorquers whose magnetic dipole moment value is close to $2A.m^2$, which will be helpful in the selection for ACS. Considering all the above-mentioned factors, CubeSpace Gen2 CR0020 is selected for the design.

Brand	Model	Max. Dipole Moment ($A.m^2$)	Weight (g)
CubeSpace [47]	Gen2 CR0020	2.0	54
New Space Systems [23]	NCTR-M012	1.19	53
New Space Systems [24]	NCTR-M016	1.6	53
ZARM Technik AG [25]	MTxx-xx	Tailored	Tailored

Table 4.12.: Magnetorquers on the market

[23]Please see: https://www.newspacesystems.com/wp-content/uploads/2021/10/NewSpace-Magnetorquer-Rod_20211018a.pdf

[24]Please see: https://www.newspacesystems.com/wp-content/uploads/2021/10/NewSpace-Magnetorquer-Rod_20211018a.pdf

[25]Please see: https://www.zarm-technik.biz/torquer-contact

4.4.7. Overall

Table 4.13 shows all selected components, after the analysis made in Sections 4.4.2, 4.4.3, 4.4.4, 4.4.5, and 4.4.6, with their mass and power budgets. While creating the table, the following assumptions were made:

- In space systems, these components are utilized with redundancy, in order to prevent single point of failures, in cases of sensor or actuator errors. The current environment set up in Scilab/Xcos allows such redundancy. However, for simplicity and performance purposes, there are no redundant sensors and actuators.
- All single-axis components (gyroscope, reaction wheel, and magnetorquer) were mounted upon Body Frame X-Y-Z axes for the rest of this thesis work, for the purpose of not imposing additional rotation matrices to the simulation blocks, which speeds simulations up.
- The mass budget column in the Table 4.13 is valid. However, the power budget column shows only the case, when all components are open, active, and consuming their maximum power, which is not realistic. For example, from Section 4.4.6, the magnetorquers have to be switched off, in order to allow magnetometers to take proper measurements, which highly reduces the power consumption.
- In Xcos simulations, star tracker block from *Spacecraft GNC Toolbox* gives the output attitude measurement as a single block. However, in practical cases, there is at least two or three star trackers located on the spacecraft, in order to scan more area in space and add redundancy to the ACS. Since the attitude observation is out of the scope of the thesis work, this issue was ignored and single star tracker usage was assumed.

Count	Component	Producer	Model	Power (W)	Weight (g)
1	Satellite Dispenser	Exolaunch	CARBONIX	-[26]	-
1	Magnetometer	ZARM Technik AG	AMR	0.3	60
3	Gyroscope	Silicon Sensing	CRH03-010	0.02	42
1	Star Tracker	AAC Clyde	ST400	0.7	280
3	Reaction Wheel	Blue Canyon Tech	RWp100	0.81	330
3	Magnetorquer	CubeSpace	Gen2 CR0020	2.0	54
-	Overall	-	-	9.49	1618

Table 4.13.: Power and mass budgets of overall selected ACS components

[26]Satellite dispensers are not attached to ACS.

5. Controller Development

5.1. Overview

In this section, the development and verification methodology and results of controller algorithms to be used in ACS are discussed in detail. Table 4.3 requires the implementation of controllers for six different modes, which are DTM, CAM, FAM, SAFE, SCAN, and IPM, remarking that ACS actuators are disabled in INIT and SUSP modes. In addition, Wertz suggests that momentum dumping should be implemented, in order to prevent saturation in the accumulated angular momentum of reaction wheels, due to cyclic and non-cyclic disturbances throughout the mission [12]. Therefore, the momentum dumping functionality works simultaneously with the operation of the one of six above-mentioned modes.

Figure 4.4 points out that SAFE, SCAN, and IPM are nominal operational modes of the ACS, while DTM, CAM, and FAM are transitional modes. In transitional modes, large attitude changes are accepted, which deviates the equilibrium point for the linearization. In other words, linearized attitude system matrix given in Section 5.3 could not apply for transitional modes, due to large attitude changes. Quaternion state feedback controllers were used in CAM, and FAM modes, while LQR controllers were used in SAFE and SCAN modes and LQI controller was used in IPM mode. Based on Table 4.3, Table 5.1 was created, in order to have an overview of controller strategies to be used throughout this section. As a notice, although control requirements of CAM and FAM differ, the usage of the same controller in these modes was aimed.

The sensors and actuators selected in Table 4.13 are digital. In other words, all the data input/output operations should be handled in discrete time, although the real physical world is continuous. Therefore, all the hardware placed in simulations should be run at a pre-determined frequency, in order to prevent disturbance accumulation as angular momentum on the satellite up to the degree of affecting sensor measurements and scientific goals. The other theoretical factor of controller frequency selection is controlling under the maximum angular rate possible throughout the mission, which is tip-off angular velocity defined in Section 4.4.1. From the practical point of view, since the average orbit period is around 95 minutes, having as little control frequency as possible will significantly reduce simulation time, which helps in faster controller development. After the empirical process, the controller frequency of the simulation was set to be $1Hz$. About Xcos simulations, all of the clocks driving ACS hardware

and disturbance blocks were run with the same frequency, $1Hz$, since this thesis work does not contain any attitude observer unit. It was assumed that there was an attitude observer in between sensors and the OBC, which gives the output at the same clock tick. This assumption helps the simulation leave the burden of timing and synchronization of sensor readings.

From the stability perspective, the attitude and angular rate error accumulation due to the disturbances between two samples should be lower than the most precise mode control accuracy. According to Table 5.1, from IPM controller, this value is $0.1\,\text{deg} - 0.01\,\text{deg}/s$. Then, by taking the maximum disturbance torque value from Table 4.7 and applying it to Equation 3.7, the accumulated angular rate and attitude errors might be obtained. Since only angular rate and attitude change due to external torques are the main focus of interests, $\boldsymbol{\omega}$ and $\boldsymbol{H}$ may be zeroed from Equation 5.1, for simplification purposes. In addition, the minimum value on the diagonal of the moment of inertia matrix, $1.57kg.m^2$ was given to I, in this equation. From Equation 5.1 and 5.2, it might be concluded that setting the frequency to $1Hz$ does not become the source of errors in further simulations.

$$\triangle\omega = \frac{\triangle t}{I}\left(T_{d_{max}} - \boldsymbol{\omega} \times \boldsymbol{H}\right) = \frac{T_{d_{max}}}{I} = 1.6982 \times 10^{-3}\,\text{deg}/s \tag{5.1}$$

$$\triangle q = \int_0^1 \triangle\omega t dt = 8.49 \times 10^{-4}\,\text{deg}/s \tag{5.2}$$

For testing robustness and verification of controllers on Table 5.1, worst case analysis and Monte Carlo simulation methods were used. Since nominal modes (SAFE, SCAN, and IPM) require attitude stabilization, the robustness of these modes should be highly examined and therefore, Monte Carlo techniques were used for such purpose. As for transitional modes (DTM, CAM, and FAM), there was no requirement for such stabilization, and therefore, worst-case scenario analysis was used for these modes.

Mode	Entry Condition	Control Requirement	Control Law	Components Used	Verification Method
DTM	– deg 2 deg/s	– deg 0.2 deg/s	Cross Product	MAG, GY, MT	Worst Case Analysis
CAM	– deg 0.2 deg/s	10 deg 0.2 deg/s	Quaternion PD	ST, GY, RW	Worst Case Analysis
FAM	– deg 0.2 deg/s	0.2 deg 0.02 deg/s	Quaternion PID	ST, GY, RW	Worst Case Analysis
SAFE	10 deg 0.2 deg/s	5 deg 0.1 deg/s	LQR	ST, GY, RW	Monte Carlo Simulation
SCAN	2 deg 0.1 deg/s	1 deg 0.05 deg/s	LQR	ST, GY, RW	Monte Carlo Simulation
IPM	0.2 deg 0.02 deg/s	0.1 deg 0.01 deg/s	LQRI	ST, GY, RW	Monte Carlo Simulation
Momentum Dumping	– deg – deg/s	– deg – deg/s	P	MAG, RW, MT	Worst Case Analysis

Table 5.1.: Controller mode definitions and their corresponding control laws

5.2. De-Tumbling Mode

As Section 4.2 suggests, this mode aims to reduce the angular rate of the satellite after the event of separation and recovery of errors due to high angular momentum accumulated on the satellite. The only aim of this mode is to reduce the angular momentum down to the degree that star trackers become operable. Moreover, after de-tumbling the satellite, the angular momentum saturation of one of the reaction wheels before half orbit is not the desired case. For satellite de-tumbling, three main strategies might be applied. They are:

- **Strategy 1:** B-Dot Method
- **Strategy 2:** Cross Product Method
- **Strategy 3:** De-tumbling with reaction wheels only.

The magnetorquer with the maximum magnetic dipole moment of $2A.m^2$ was selected in Section 4.4.6. However, in order to preserve magnetometer measurements from magnetic disruptions due to the magnetorquer actuation, magnetorquers have to be switched off during magnetometer measurement. On the other hand, the higher magnetic torque actuation time means better de-tumbling performance of ACS. Since the magnetometer selected in Section 4.4.2 has up to $300Hz$ sampling rate, it can be assumed that the magnetorquer can be activated 80 percent of the duty cycle, while the remaining 20 percent is allocated for magnetometer measurement. The duty cycle could be favored towards magnetorquers, however, keeping the safety margin highest could make ACS more robust. As a result, the magnetorquer maximum magnetic dipole output is taken as $1.6A.m^2$ for the rest of the thesis work. In Xcos simulations, the time adjustment of clock events connected to the magnetometer and magnetorquer was possible. However, the simulation performance was degraded down to a factor of five, which would make the tuning and the development process much slower.

Table 5.1 suggests worst case analysis was required for DTM. Worst case analysis brings the mission start date of all simulations to be set as 9th April 2028 08:00:00 a.m., as indicated in Table 4.5. Furthermore, the maximum angular rate possible declared in Table 4.3, $2deg/s$, was given as the initial angular rate of the satellite with respect to the Earth Centered Inertial Frame. Although the attitude of the satellite related to the inertial frame was decisive on angular momentum direction on the inertial frame, it has minor effects on the magnitude of the angular momentum, since the moment of inertia matrix from Table 4.2 is almost scalar multiplied identical matrix. Hence, the initial attitude to the inertial frame was selected arbitrarily.

B-Dot and Cross Product methods are the most common de-tumbling strategies utilized in ACS and both of them will be analyzed in this section. As for de-tumbling with reaction wheels only, one can easily deduce from Table 5.1 that having the maximum tip-off rate from the launch vehicle might have resulted in $2deg/s$ angular rate, which equals to $0.0349rad/s$. The maximum value on the diagonal of the moment of inertia matrix is $1.67kg.m^2$. The maximum angular momentum value may be found as $0.0583N.m.s$. The

reaction wheel selected in Section 4.4.5 has the angular momentum capacity of $0.1N.m.s$, and therefore 58.7 percent of the capacity would already be used to de-tumbling. Although this approach was proven to be possible, the remaining angular momentum on reaction wheels might not suffice to counter-act disturbances, which can have values up to $0.06N.m.s$, according to Figure 4.14. As a result, the strategy of de-tumbling with reaction wheels was rejected from the beginning.

5.2.1. B-Dot Method

Markley and Crassidis suggest that [26], the required control torque to de-tumble the satellite depends on only magnetometer readings, especially for the cases if the angular velocity vector is unknown. The required control torque is given in Equation 5.3 [26], where $\boldsymbol{m^B}$ is the required magnetorquer dipole moment command related to BF, $\boldsymbol{B^B}$ is the magnetometer measurement of Earth's magnetic field with respect to BF, and k is a user-defined scalar gain.

$$\boldsymbol{m^B} = -\frac{k}{||\boldsymbol{B^B}||}\boldsymbol{B^B} \tag{5.3}$$

The De-Tumbling Mode mode controller simulation diagram with the B-Dot method is given in Figure A.11. Since the on-board computer block does not contain any state variable, the derivative of the magnetic field measurement should be taken before the OBC and given as input to the OBC.

The tuning process for this mode was made on the magnetorquer actuator gain, which is indicated as k in Equation 5.3. At first, a very high gain value, 10^7, was given, in order to saturate the magnetorquers and convert the controller to a bang-bang mode B-Dot controller. As seen from Figure 5.1, the bang-bang approach gives high torque actuation with late steady-state reach. Then, the gain values were iterated from 1 to 0.25, with a binary search-like method. From this figure, it can be concluded that the B-Dot method gives the best result when the actuator gain was set to 0.5 since it has the least steady-state error while requiring low magnetorquer actuation.

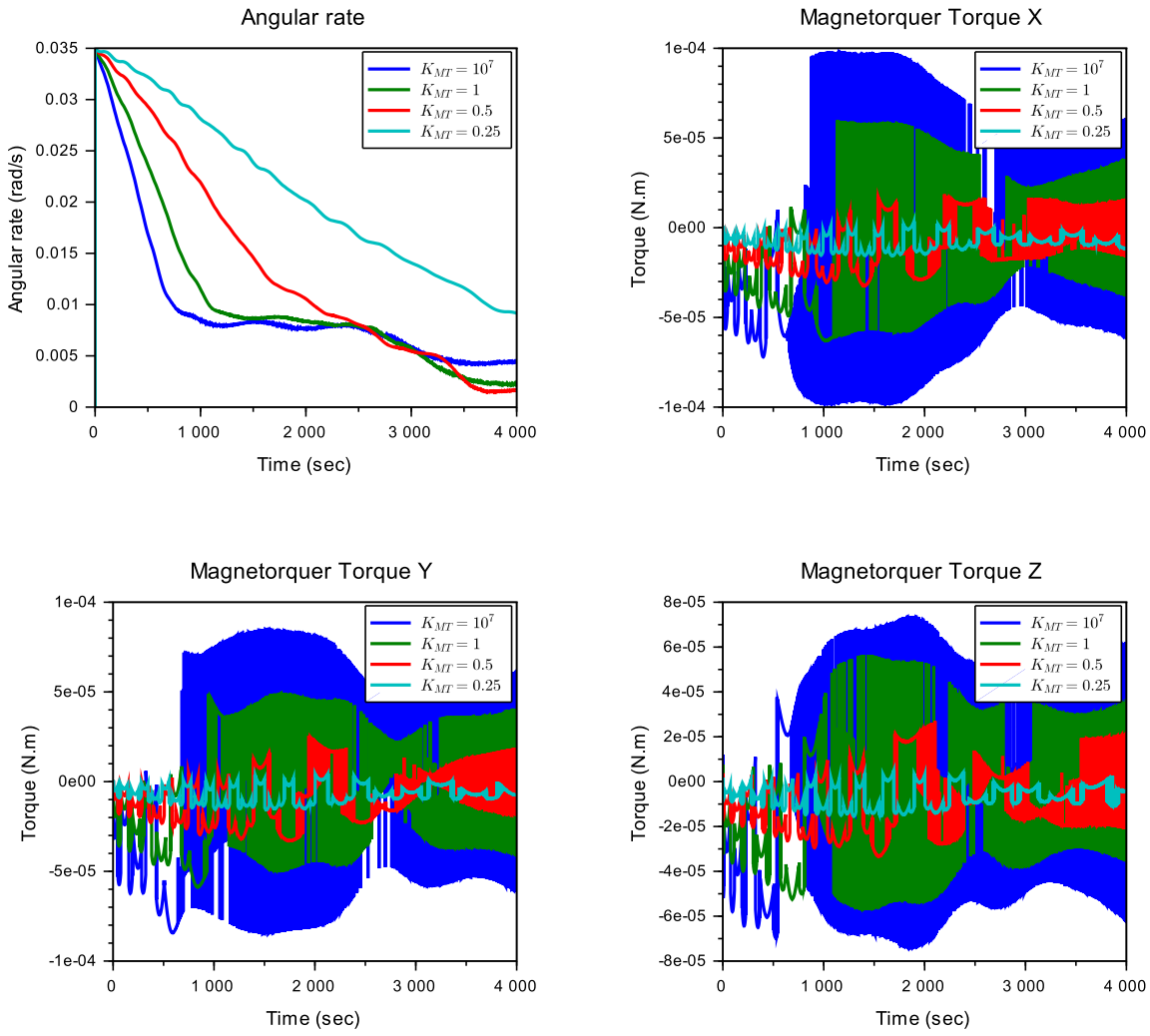

Figure 5.1.: De-Tumbling Mode B-Dot method tuning process results

5.2.2. Cross Product Method

Gordon observes that if the angular rate measurement is added besides magnetometer readings, the De-Tumbling performance becomes better than B-Dot controller [48]. The cross product de-tumbling algorithm is given in Equation 5.4 [48].

$$\boldsymbol{m^B} = -\frac{k}{||\boldsymbol{B^B}||^2}\left(\boldsymbol{\omega^B} \times \boldsymbol{B^B}\right) \tag{5.4}$$

The Xcos simulation diagram is illustrated in Figure A.12. For the tuning process of the magnetorquer gain value, the same gain iteration values with Section 5.2.1 were given. The tuning process results are given in Figure 5.2. Compared with Figure 5.1, Figure 5.2 shows similar behavior with the results of the B-Dot method. This similarity appears in the bang-bang approach results and having the gain value of 0.5 again gives the most feasible result. The only difference is the cross-product gain value of 0.5 gives the angular rate steady-state error, approximately $1.5 \times 10^{-4} rad/s$. According to Figure 5.1, this is evidently smaller than the B-Dot steady-state error.

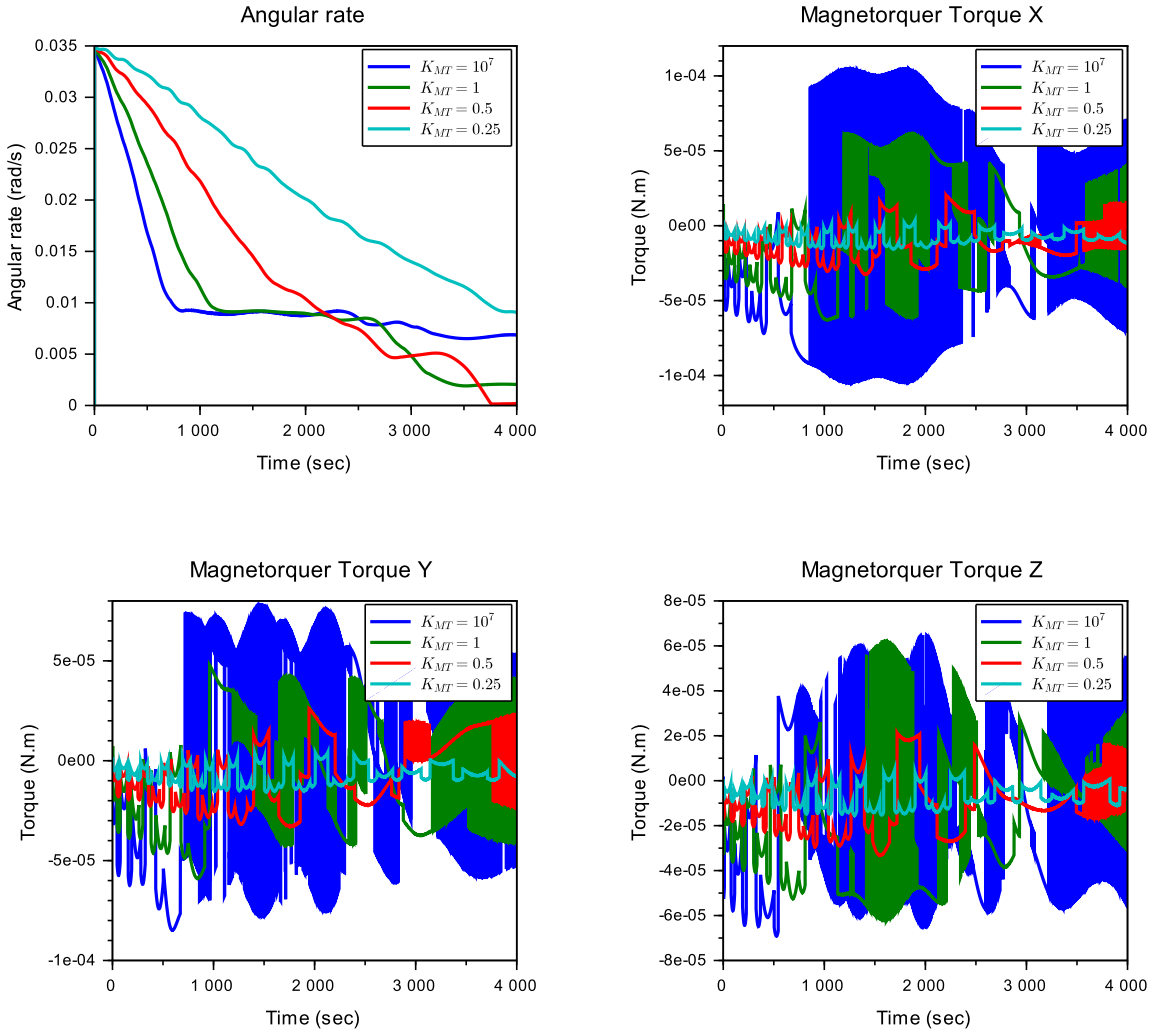

Figure 5.2.: De-Tumbling Mode Cross Product method tuning process results

5.2.3. Comparison

Figure 5.3 was illustrated in order to compare the performance of B-Dot and Cross Product methods. The plots were selected from the cases having the gain value of 0.5. As it might be seen from this figure, although they display very close behavior, Cross Product method resulted in a less steady state angular rate than the B-Dot method. As a result, for the rest of this thesis work, Cross Product method with the gain value of 0.5 is selected.

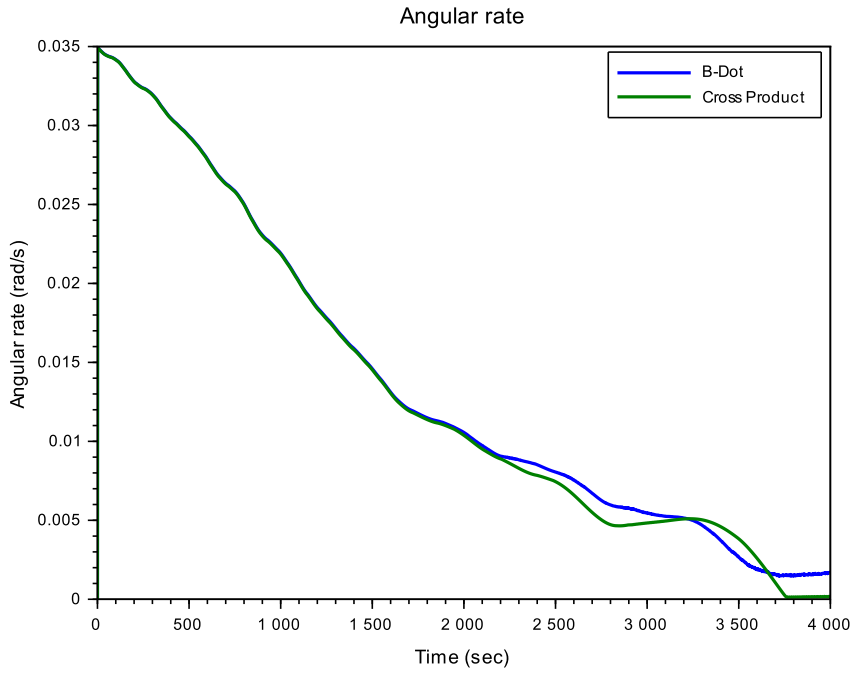

Figure 5.3.: Comparison of B-Dot and Cross Product methods with the 0.5 magnetorquer gain

5.3. Nominal Operation Modes

As Table 5.1 suggests, nominal operation modes, which are SAFE, SCAN, and IPM modes, utilize LQR control for attitude stabilization. The table also states that SAFE mode has the least optimal controller related to other nominal mode controllers because it increases the accessibility of this mode and robustness, while IPM mode controller has the most aggressive one, for the least steady-state error and fastest response. LQR controllers minimize the cost function in Equation 2.34 by employing the Algebraic Riccati equation, given in Equation 2.36. In general, Equation 2.36 might be solved for P matrix, with numerical methods. In Scilab 2023, "lqr(.)" function was provided, for the optimal gain matrix calculation, K_{LQR} and P, with the inputs of Q and R matrices, and the system plant.

The general system state equation, given in Equation 5.5, becomes 5.6 with the combination of rigid body state transition equations of 2.19, 3.4, 3.7, and gravity gradient torque equation of 3.9, and then their linearization around the point $q_i = 0$ and $\omega_i = 0$ for all $i \in \{1,2,3\}$ [49]. About quaternions from Section 2.3.2, the scalar part of quaternions is dependent on imaginary vector values. Therefore, in order to keep the controllability of the system matrix given in 5.6, the scalar part of the quaternion error was excluded from the state vector. The angular momentum values were excluded from Yang's equations, for simplicity purposes [49]. In Equation 5.6, $\begin{bmatrix} u_X & u_Y & u_Z \end{bmatrix}^T$ are reaction wheel control torque values.

$$\dot{\boldsymbol{x}} = A\boldsymbol{x} + B\boldsymbol{u} \tag{5.5}$$

$$\begin{bmatrix} \dot{q_1} \\ \dot{q_2} \\ \dot{q_3} \\ \dot{\omega_1} \\ \dot{\omega_2} \\ \dot{\omega_3} \end{bmatrix} = \begin{bmatrix} 0 & 0 & 0 & 0.5 & 0 & 0 \\ 0 & 0 & 0 & 0 & 0.5 & 0 \\ 0 & 0 & 0 & 0 & 0 & 0.5 \\ \eta_{41} & 0 & 0 & 0 & 0 & \eta_{46} \\ 0 & \eta_{52} & 0 & 0 & 0 & 0 \\ 0 & 0 & \eta_{63} & \eta_{64} & 0 & 0 \end{bmatrix} \begin{bmatrix} q_1 \\ q_2 \\ q_3 \\ \omega_1 \\ \omega_2 \\ \omega_3 \end{bmatrix} + \begin{bmatrix} 0 & 0 & 0 \\ 0 & 0 & 0 \\ 0 & 0 & 0 \\ I_{11}^{-1} & 0 & 0 \\ 0 & I_{22}^{-1} & 0 \\ 0 & 0 & I_{33}^{-1} \end{bmatrix} \begin{bmatrix} u_X \\ u_Y \\ u_Z \end{bmatrix}, \text{where} \tag{5.6}$$

$$\boldsymbol{\omega_0^{I/L}} = \begin{bmatrix} 0 \\ -\omega_0 \\ 0 \end{bmatrix}, \text{ where } \omega_0 = \frac{2\pi}{T} \text{ and T is orbital period.} \tag{5.7}$$

$$\eta_{41} = 8\omega_E^2 \frac{I_{33} - I_{22}}{I_{11}} \tag{5.8}$$

$$\eta_{46} = \omega_0 \frac{-I_{11} + I_{22} - I_{33}}{I_{11}} \tag{5.9}$$

$$\eta_{52} = 6\omega_E^2 \frac{I_{33} - I_{11}}{I_{22}} \tag{5.10}$$

$$\eta_{63} = 2\omega_E^2 \frac{I_{11} - I_{22}}{I_{33}} \tag{5.11}$$

$$\eta_{64} = -\eta_{46} \frac{I_{11}}{I_{33}} \tag{5.12}$$

Equation 5.6 points out an evidently controllable system and its controllability was proven by *ctrl* function of Scilab 2023.1.0. SAFE and SCAN mode controllers are implemented based on Equation 5.6. However, it is given in Section 5.3.3 that, zero-order steady state error occurs in these modes. Therefore, as stated in Section 2.4.4, the augmentation with integral action is required. The attitude state variables are derived from the integral of angular velocity already and hence, only the integral of attitude state variables are required for the augmentation. If the integral of attitude quaternions, q_i are symbolized as Q_i and the augmented matrices and vectors are notated with a tilde symbol, Equation 5.6 becomes 5.14.

$$\dot{\tilde{\boldsymbol{x}}} = \tilde{A}\tilde{\boldsymbol{x}} + \tilde{B}\tilde{\boldsymbol{u}} \tag{5.13}$$

$$\begin{bmatrix} \dot{Q}_1 \\ \dot{Q}_2 \\ \dot{Q}_3 \\ \dot{\boldsymbol{x}} \end{bmatrix} = \begin{bmatrix} 0_{3\times3} & I_{3\times3}\ 0_{3\times3} \\ 0_{6\times3} & A \end{bmatrix} \begin{bmatrix} Q_1 \\ Q_2 \\ Q_3 \\ \boldsymbol{x} \end{bmatrix} + \begin{bmatrix} 0_{3\times3} \\ B \end{bmatrix} \begin{bmatrix} u_X \\ u_Y \\ u_Z \end{bmatrix} \tag{5.14}$$

The Xcos simulation diagram for both controller tuning and Monte Carlo campaigns of nominal modes (SAFE, SCAN, and IPM) might be seen in Figure A.13. Since mechanical properties of the satellite, disturbance torques, sensors, and actuators do not depend on the control mode, the values given to these blocks can be gathered to a single table. The common simulation parameters among modes are given in Table 5.2. For performance purposes, misalignment errors on sensors and actuators are disabled. For the same purpose, single axis components (Gyroscope, Reaction Wheels, Magnetorquers) are placed upon $X-Y-Z$ axes of BF and all ACS components were perfectly aligned with the BF. In order to make a distinction between modes, "cMode" parameter on the diagram was set accordingly.

Block Name	Parameter Name	Value	Unit
-	Simulation Frequency	1	Hz
Rigid Body Gravity Gradient Onboard Computer	Moment of Inertia	$\begin{bmatrix} 1.67 & 0 & 0 \\ 0 & 1.6 & 0 \\ 0 & 0 & 1.57 \end{bmatrix}$	$kg.m^2$
Star Tracker	Noise Standard Deviation	$10,120$	$arcsec$
Star Tracker	Boresight Angular Rate Limit for Measurement	0.5	deg $/s$
Gyroscope	Noise Standard Deviation	8.3×10^{-6}	deg $/s$
Gyroscope	Maximum Angular Rate	10	deg $/s$
Magnetometer	Noise Standard Deviation	8.5	nT
Gravity Gradient	J_2 Enable	No	-
Magnetic Field	Density Model	IGRF-13	-
Atmospheric Drag	Density Model	NRLMSISE-00	-
Atmospheric Drag	81 Day Avg. F10.7 Flux (F107A)	200	m^2Hz
Atmospheric Drag	Daily F10.7 Flux for the Previous Day (F107)	200	m^2Hz
Atmospheric Drag	Satellite Drag Coefficient	2.4	-
Atmospheric Drag	Satellite Cube Edge Length	60	cm
Atmospheric Drag	Satellite Geometric Center Coordinates w.r.t. Body Frame	$\begin{bmatrix} 2 \\ 3 \\ -5 \end{bmatrix}$	cm
Reaction Wheel	Angular Momentum Capacity	100	$mN.m.s$
Reaction Wheel	Torque Limit	6	$mN.m.s$
Reaction Wheel	PT1 Delay Time Constant	10	ms
Reaction Wheel	Noise Standard Deviation	0	$N.m$

Table 5.2.: Nominal operation modes common block parameters

The LQR controller Q and R matrix tuning could be started from either identical matrices or the matrices resulted from Bryson's rule. Bryson's Rule suggests that the tuning process of Q_{ii} and R_{ii} could be started from employing Equations 5.15 and 5.16 for each state and output variable, respectively [50].

$$Q_{ii} = \frac{1}{max(x_i)^2} \tag{5.15}$$

$$R_{ii} = \frac{1}{max(u_i)^2} \tag{5.16}$$

The initial trial Q and R matrices could be determined via Equation 5.15 and 5.16 to all three nominal operation mode controllers, taking the entry conditions from Table 5.1. From Equation 2.17b to 2.17d, the maximum attitude quaternion values could be obtained, as given in Equation 5.17a. The calculated initial Q and R matrices for these three modes are given in Equation 5.17b-5.17h.

$$max(q_i) = \sin\left(\frac{\phi}{2}\right) = \sqrt{1 - \cos^2\left(\frac{\phi}{2}\right)}, \text{ where } i \in \{1,2,3\} \tag{5.17a}$$

$$Q_{iiSAFE} = \frac{1}{\sin^2\left(\frac{10^\circ}{2}\right)} = 131.646, \text{ where } i \in \{1,2,3\} \tag{5.17b}$$

$$Q_{iiSAFE} = \frac{1}{(3.49 \times 10^{-3} rad)^2} = 82070.158, \text{ where } i \in \{4,5,6\} \tag{5.17c}$$

$$Q_{iiSCAN} = \frac{1}{\sin^2\left(\frac{2^\circ}{2}\right)} = 3283.139, \text{ where } i \in \{1,2,3\} \tag{5.17d}$$

$$Q_{iiSCAN} = \frac{1}{(1.74 \times 10^{-3} rad)^2} = 328280.635, \text{ where } i \in \{4,5,6\} \tag{5.17e}$$

$$Q_{iiIPM} = \frac{1}{\sin^2\left(\frac{0.2^\circ}{2}\right)} = 82070.492, \text{ where } i \in \{1,2,3\} \tag{5.17f}$$

$$Q_{iiIPM} = \frac{1}{(3.49 \times 10^{-4} rad)^2} = 8207015.875, \text{ where } i \in \{4,5,6\} \tag{5.17g}$$

$$R_{jjSAFE} = R_{jjSCAN} = R_{jjIPM} = \frac{1}{(6 \times 10^{-3})^2} = 27777.777, \text{ where } j \in \{1,2,3\} \tag{5.17h}$$

5.3.1. Safe Mode

Table 5.3 was formed for explaining SAFE mode specific parameters used in the tuning simulation. During the parametrization, the mission start date was selected arbitrarily, not one of the dates given in Table 4.5, because the controller for SAFE mode is not supposed to be optimal and aggressive, like IPM, and the disturbance along the orbit would not change the controller behavior. After selecting the optimal Q and R matrices, the robustness of the selected controller will be examined in Monte Carlo simulations extensively.

Initial attitude and angular rate parameters for Rigid Body block in Table 5.3 were set according to the ECI position of the satellite, which brings LVLH frame into action. From Figure 2.2, it might be seen that the Z axis of LVLH frame shows Nadir direction, and therefore no additional rotation matrix multiplication is required to the initial condition of the satellite attitude. For the purpose of adding errors, 10 deg around BF X axis was introduced for each case, which is the entry condition of SAFE mode, as shown in Table 4.3. The initial angular rate was selected by including the angular rate vector found in Equation 5.7 into Equation 5.18. Since LVLH rotates around its Y axis, the value will be updated throughout the simulation and will be set as the target angular velocity vector for ACS.

$$\boldsymbol{\omega_0^{B/I}} = C^{B/I} C^{I/L} \boldsymbol{\omega_0^{L/I}} \tag{5.18}$$

The magnitude of the residual magnetic dipole moment of the satellite might be at most $1 A.m^2$, according to Table 4.2. Since the satellite orbits around the Earth near the Polar region due to being Sun Synchronous, the magnetic field vector should have approximately X axis line with respect to the LVLH frame, alternating in between positive and negative X axes. Since the magnitude of the cross product of two vectors is equal to the multiplication of the magnitude of these two with the sinus of the angle in between them, having 90 deg angle in between then should give the maximum magnitude. Therefore, having the magnetic dipole moment of the satellite perpendicular to the magnetic field vector would give the maximum magnetic disturbance torque, which is possible by giving all the magnitude to the Z axis. Therefore, in Table 5.3, the residual magnetic dipole moment of the satellite was assigned as $\begin{bmatrix} 0 & 0 & 1 \end{bmatrix}^T$. Y axis would be another alternative and nevertheless, the Y axis would be rotating throughout the orbit period causing deviation from the maximum disturbance torque.

Block Name	Parameter Name	Value	Unit
-	Mission Start Time	1st Jan 2028 00:00:01	UTC+00
Rigid Body	Initial Attitude w.r.t. BF	$\begin{bmatrix}-0.0466127 & 0.6936885 & 0.1370993 & 0.7055687\end{bmatrix}^T$ + 10 deg rotation around BF X axis	Quaternion Real First
Rigid Body	Initial Angular Velocity w.r.t. BF	$\begin{bmatrix}-0.000287 & 0.0010765 & -0.0001447\end{bmatrix}^T$	rad/sec
Residual Magnetic	Satellite Residual Magnetic Dipole Moment w.r.t. BF	$\begin{bmatrix}0 & 0 & 1\end{bmatrix}^T$	$A.m^2$
Case 1	LQR Q Matrix LQR R Matrix Attitude Error Integral Gain	$\text{diag}(40, 40, 40, 10000, 10000, 10000)$ $\text{diag}(35000, 35000, 35000)$ $\begin{bmatrix}0 & 0 & 0\end{bmatrix}^T$	-
Case 2	LQR Q Matrix LQR R Matrix Attitude Error Integral Gain	$\text{diag}(40, 40, 40, 10000, 10000, 10000)$ $\text{diag}(60000, 60000, 60000)$ $\begin{bmatrix}0 & 0 & 0\end{bmatrix}^T$	-
Case 3	LQR Q Matrix LQR R Matrix Attitude Error Integral Gain	$\text{diag}(20, 20, 20, 10000, 10000, 10000)$ $\text{diag}(50000, 50000, 50000)$ $\begin{bmatrix}0 & 0 & 0\end{bmatrix}^T$	-
Case 4	LQR Q Matrix LQR R Matrix Attitude Error Integral Gain	$\text{diag}(5, 5, 5, 10000, 10000, 10000)$ $\text{diag}(50000, 50000, 50000)$ $\begin{bmatrix}0 & 0 & 0\end{bmatrix}^T$	-
Case 5	LQR Q Matrix LQR R Matrix Attitude Error Integral Gain	$\text{diag}(2, 2, 2, 10000, 10000, 10000)$ $\text{diag}(50000, 50000, 50000)$ $\begin{bmatrix}0 & 0 & 0\end{bmatrix}^T$	-

Table 5.3.: SAFE mode specific parameters and tuning matrices for each case

SAFE mode tuning process results are given in Figure 5.4. In this figure, the deviation from the target attitude is calculated by taking the inverse of Equation 2.17a and the angular rate error is to be calculated via subtraction of the target angular rate vector found in Equation 5.18, and taking the Euclidian norm of the resultant vector. From these results, it may be seen that the controller first tries to reduce the attitude error by increasing the angular rate. Then, it goes steady state for both attitude and angular rate. From Table 4.3, the entry condition for SAFE mode is $0.2\,\text{deg}/s = 3.49 \times 10^{-3} rad/s$ and hence, the cases exceeding $3.49 \times 10^{-3} rad/s$, Case (1-3) were eliminated from the selection. Among Case 4-5, **Case 4** was selected since it has less steady-state error than Case 5. The activation of the integrator would optimize the controller, however, the controller is not supposed to be that aggressive, and Case 4 reaches steady state error around 1 deg, which is below 5 deg. Moreover, the addition of an integrator would increase the angular rate overshoot causing the excess of the controller angular rate threshold.

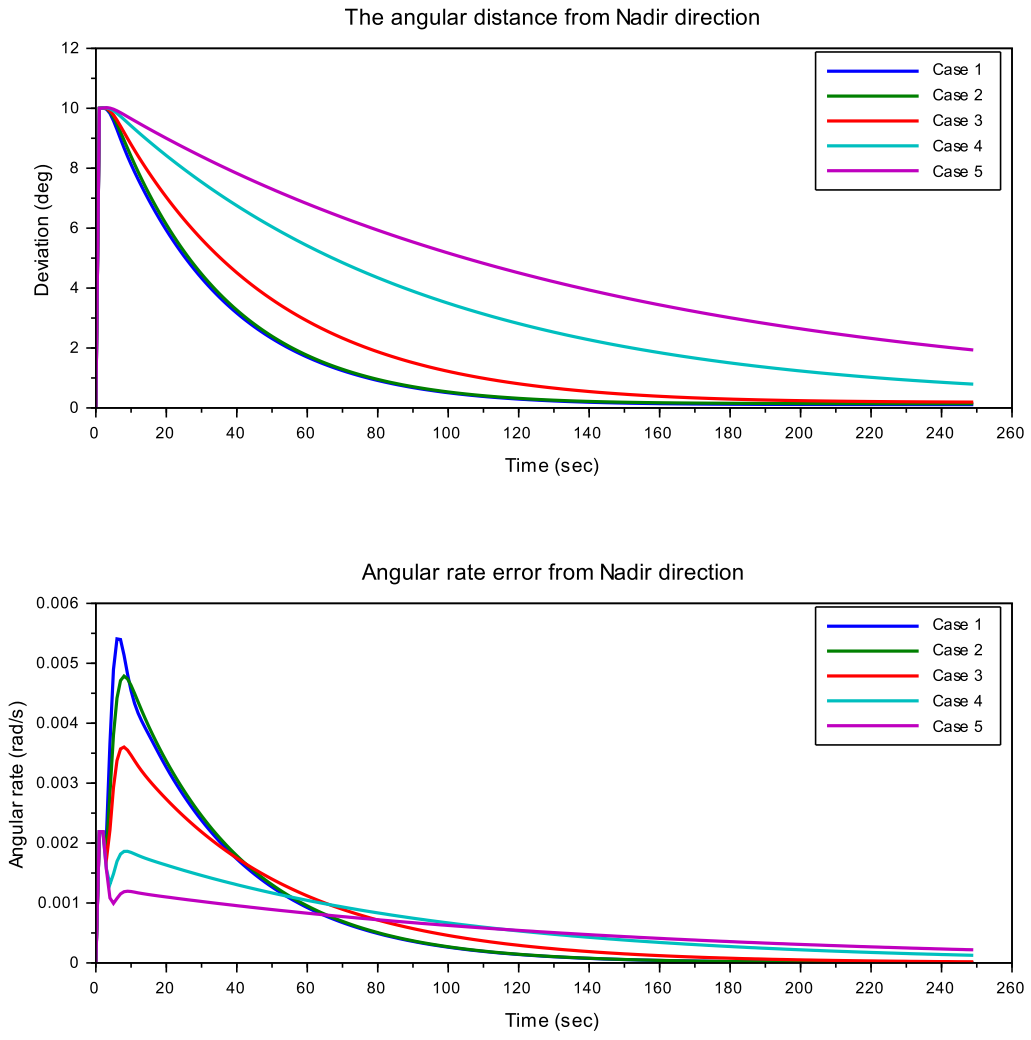

Figure 5.4.: SAFE mode LQR tuning process attitude and angular rate errors vs. simulated cases

As Section 2.4.2 states, in order to analyze the global asymptotically stability of the controller, eigenvalues of the close loop system should be calculated. Scilab *lqr* function outputs the optimal gain matrix while taking Q, R, and all of the plant matrices as inputs. The optimal gain matrix of SAFE mode was given in Equation 5.19. From this matrix, with the help of Scilab *spec* function, eigenvalues of the close loop system could be obtained. The resultant eigenvalues are shown in Equation 5.20. According to Section 2.4.2, since all eigenvalues have negative real parts and imaginary values are non-repetitive, it might be deduced that the SAFE mode controller with Q and R matrices from Case 4 is local asymptotically and Lyapunov stable.

$$K_{SAFE} = \begin{bmatrix} 0.0099996 & 3.588 \times 10^{-11} & 0.0000413 & 0.4655097 & -6.640 \times 10^{-11} & -1.811 \times 10^{-9} \\ -4.550 \times 10^{-16} & 0.0099992 & -9.602 \times 10^{-15} & 8.868 \times 10^{-16} & 0.4647566 & 1.285 \times 10^{-14} \\ -0.0000413 & 5.619 \times 10^{-12} & 0.0100001 & -1.927 \times 10^{-9} & -9.701 \times 10^{-12} & 0.4644353 \end{bmatrix} \quad (5.19)$$

$$\lambda_{SAFE} = \begin{bmatrix} -0.2676412 \\ -0.2845469 \\ -0.2792835 \\ -0.0111894 + 0.0000019i \\ -0.0111894 - 0.0000019i \\ -0.0111893 \end{bmatrix} \tag{5.20}$$

Provided that Q and R matrices in Case 4 were selected for SAFE mode controller, Monte-Carlo simulations were executed, for the purpose of verification of selected control parameters in means of robustness. Due to the fact that Xcos simulations take time, two different Monte Carlo simulations were run. The first one executes 1080 test cases with 250 seconds duration, while the second executes 4 test cases with 6000 seconds duration (more than an orbital period), to check the long-term stability of the controller. In order to generate randomized test cases, the magnitude ranges of input parameters are collected in Table 5.4, taking Table 5.1 into account. Figure 5.5 shows the short-duration Monte Carlo simulation results and Figure 5.6 displays results in the long run.

In Figure 5.5a, it is observed that the attitude error starts from 14 deg instead of 10 deg. This situation was sourced from missing normalization operation during the calculation of initial parameters. Since Figure 5.5 shows stable behavior in every condition, without causing a saturation error on star trackers and gyroscopes due to high angular rate, short-run Monte Carlo simulation was not repeated with corrected parameters. As for the long Monte Carlo run, in Figure 5.6, the steady state attitude error is below 0.5 deg, the angular rate error is negligibly small, and the maximum angular momentum accumulated on reaction wheels lays below $0.03 N.m.s$, which is less than the half of the capacity. As a conclusion, the controller selected after the tuning process (Case 4) was proven to be stable for the rest of this thesis work.

Parameter Name	Minimum Value	Maximum Value	Unit
The difference from target attitude	0	10	deg
The difference from target angular rate	0	0.2	deg
Moment of Inertia matrix Off-Diagonal elements	0	0.167	$kg.m^2$

Table 5.4.: SAFE mode Monte Carlo simulation input ranges in magnitude

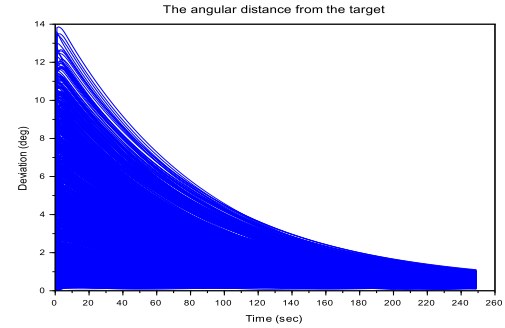

(a) Attitude error

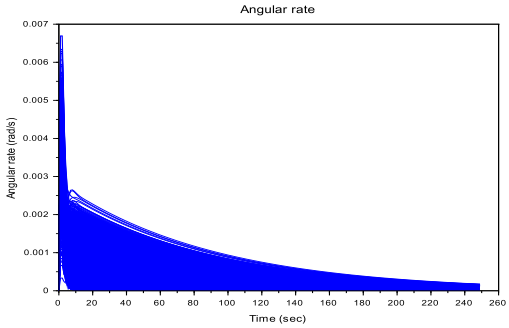

(b) Angular rate error

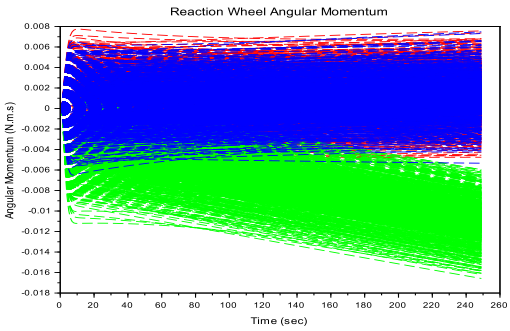

(c) Angular momentum accumulated on reaction wheels

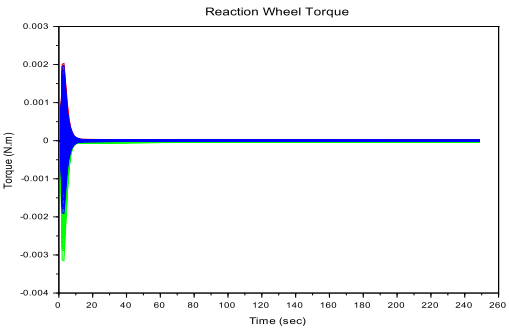

(d) Torque applied by reaction wheels

Figure 5.5.: SAFE mode Monte Carlo short term simulation results

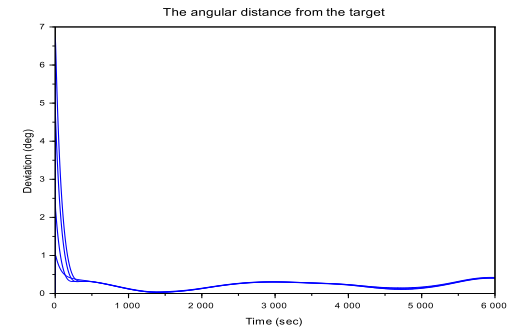

(a) Attitude error

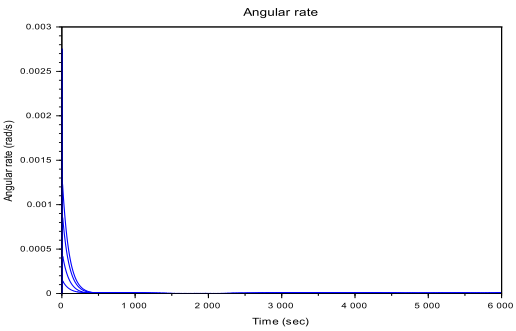

(b) Angular rate error

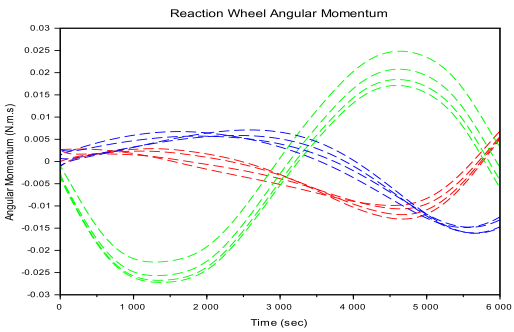

(c) Angular momentum accumulated on reaction wheels

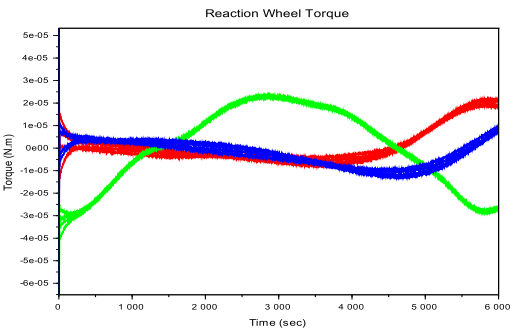

(d) Torque applied by reaction wheels

Figure 5.6.: SAFE mode Monte Carlo long term simulation results

5.3.2. Scan Mode

For SCAN mode controller implementation, a similar methodology with SAFE mode controller from Section 5.3.1 was followed, since the target attitude and angular rate dynamics of these modes are the same. The only difference is, in order to have Body Frame +Z axis pointing Zenith direction, the target attitude should be LVLH frame with respect to the ECI, but with additional rotation by 180 deg around X or Y axis. Such rotation was arbitrarily made on the X-axis. As seen from Table 5.5, the initial condition of these values is selected regarding this rotation. The mission start date and satellite residual magnetic dipole moment values are the same as these values in Table 5.3. LQR tuning process was started from the selected Q and R matrices of SAFE controller, Case 4 of Table 5.3.

Block Name	Parameter Name	Value	Unit
-	Mission Start Time	1st Jan 2028 00:00:01	UTC+00
Rigid Body	Initial Attitude w.r.t. BF	$\begin{bmatrix}-0.6936885 & -0.0466127 & 0.7055687 & -0.1370993\end{bmatrix}^T$ + 2 deg rotation around BF X axis	Quaternion Real First
Rigid Body	Initial Angular Velocity w.r.t. BF	$\begin{bmatrix}0.0001453 & -0.0011045 & -0.0001466\end{bmatrix}^T$	rad/sec
Residual Magnetic	Satellite Residual Magnetic Dipole Moment w.r.t. BF	$\begin{bmatrix}0 & 0 & 1\end{bmatrix}^T$	$A.m^2$
Case 1	LQR Q Matrix LQR R Matrix Attitude Error Integral Gain	$\text{diag}(5,5,5,10000,10000,10000)$ $\text{diag}(50000,50000,50000)$ $\begin{bmatrix}0 & 0 & 0\end{bmatrix}^T$	-
Case 2	LQR Q Matrix LQR R Matrix Attitude Error Integral Gain	$\text{diag}(20,20,20,10000,10000,10000)$ $\text{diag}(50000,50000,50000)$ $\begin{bmatrix}0 & 0 & 0\end{bmatrix}^T$	-
Case 3	LQR Q Matrix LQR R Matrix Attitude Error Integral Gain	$\text{diag}(120,120,120,10000,10000,10000)$ $\text{diag}(50000,50000,50000)$ $\begin{bmatrix}0 & 0 & 0\end{bmatrix}^T$	-
Case 4	LQR Q Matrix LQR R Matrix Attitude Error Integral Gain	$\text{diag}(120,120,120,50000,50000,50000)$ $\text{diag}(50000,50000,50000)$ $\begin{bmatrix}0 & 0 & 0\end{bmatrix}^T$	-
Case 5	LQR Q Matrix LQR R Matrix Attitude Error Integral Gain	$\text{diag}(120,120,120,50000,50000,50000)$ $\text{diag}(100000,100000,100000)$ $\begin{bmatrix}0 & 0 & 0\end{bmatrix}^T$	-

Table 5.5.: SCAN mode specific parameters and tuning matrices for each case

Figure 5.7 depicts SCAN mode tuning process results. The calculation method of attitude and angular rate error are the same with the Section 5.3.1, except the fact that initial attitude error was set to 2 deg, as Table 5.1 suggests, and 180 deg rotation from LVLH frame. Like Figure 5.4, the controller first attempts to reduce the attitude error, and then the angular rate error decays. From Table 5.1, the angular rate of entry condition of SCAN mode is $0.1\,\text{deg}/s = 1.745 \times 10^{-3} rad/s$. Therefore, by looking at Figure 5.7, the controller having the smallest steady state time was selected, while taking into account the angular rate overshoot should stay below $1.745 \times 10^{-3} rad/s$. As a result, **Case 5** was selected for SCAN mode LQR controller.

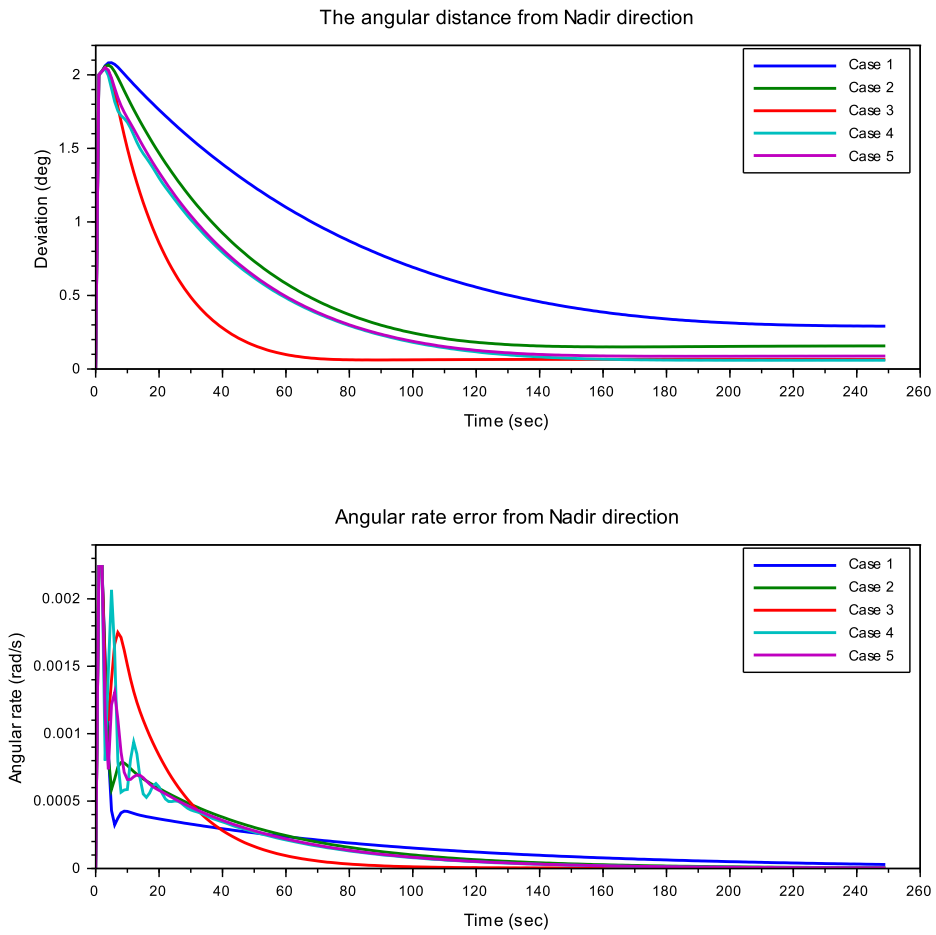

Figure 5.7.: SCAN mode LQR tuning process attitude and angular rate errors vs. simulated cases

SCAN mode optimal gain matrix, calculated by the help of Scilab *lqr* function and by using Q and R matrices of Case 5, is given in Equation 5.21. By executing the *spec* function over the closed loop system in Equation 2.38, eigenvalues in Equation 5.22 were achieved. Section 2.4.2 states that these eigenvalues refer to a local asymptotically and Lyapunov stable system since all eigenvalues have negative real parts and non-repetitive imaginary parts.

$$K_{SCAN} = \begin{bmatrix} 0.0346406 & 3.558D-10 & 0.0000891 & 0.7468934 & -3.398D-10 & -3.470D-10 \\ -2.806D-15 & 0.0346402 & 6.488D-13 & 1.199D-15 & 0.7452679 & -7.367D-13 \\ -0.0000891 & -2.257D-11 & 0.0346411 & -7.493D-10 & 2.903D-11 & 0.7445714 \end{bmatrix} \tag{5.21}$$

$$\lambda_{SCAN} = \begin{bmatrix} -0.4227579 \\ -0.4496656 \\ -0.0245336 + 0.0000029i \\ -0.0245336 - 0.0000029i \\ -0.0245328 \\ -0.4412597 \end{bmatrix} \tag{5.22}$$

SCAN mode Monte Carlo simulations with controller parameters from Case 5 were conducted. The ranges of the magnitude of attitude and angular rate errors are determined by using Table 5.1 and 4.2. As a result, 1080 short-duration, and 4 long-duration Monte Carlo simulation cases were randomly generated. by using values in Table 5.6. Since SCAN mode magnetic disturbance is at its maximum when the satellite residual dipole moment is selected as $\begin{bmatrix} 0 & 0 & 1 \end{bmatrix}^T$. Figure 5.8 depicts the short-duration Monte Carlo simulation results, while Figure 5.9 illustrates the long-term results. From both figures, it might be concluded that the SCAN mode controller with Case 5 was confirmed to be stable and satisfies the control requirements defined in Table 5.1. In addition, Figure 5.9b and 5.9d imply that SCAN mode controller works at the noise level. In other words, it might be expressed that the controller works close to its optimal point.

Parameter Name	Minimum Value	Maximum Value	Unit
The difference from target attitude	0	2	deg
The difference from target angular rate	0	0.1	deg
Moment of Inertia matrix Off-Diagonal elements	0	0.167	$kg.m^2$

Table 5.6.: SCAN mode Monte Carlo simulation input ranges in magnitude

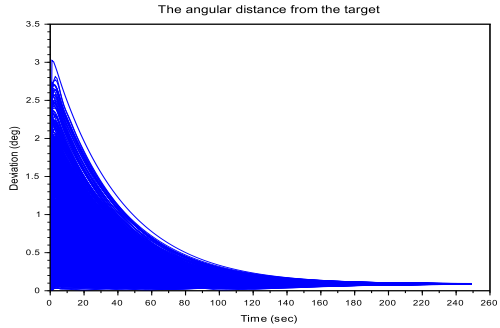

(a) Attitude error

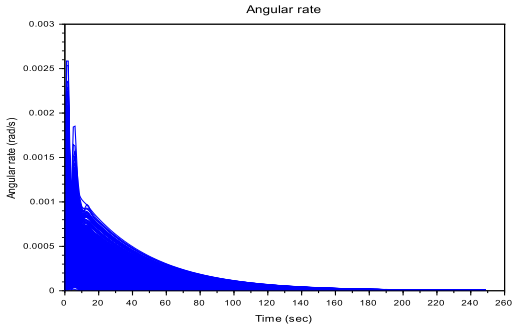

(b) Angular rate error

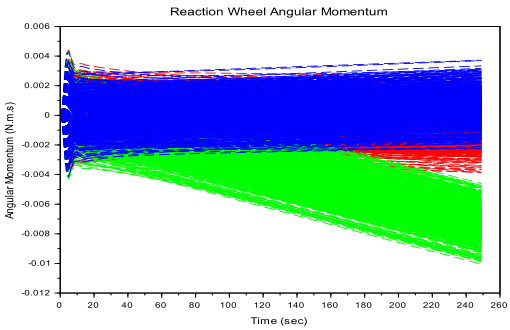

(c) Angular momentum accumulated on reaction wheels

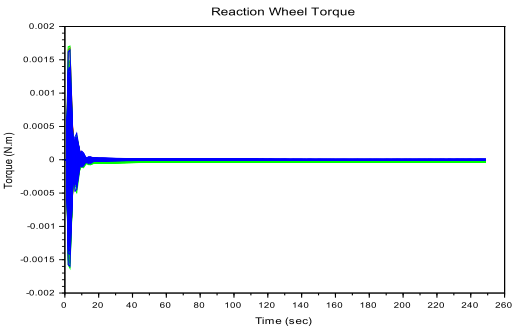

(d) Torque applied by reaction wheels

Figure 5.8.: SCAN mode Monte Carlo short duration simulation results

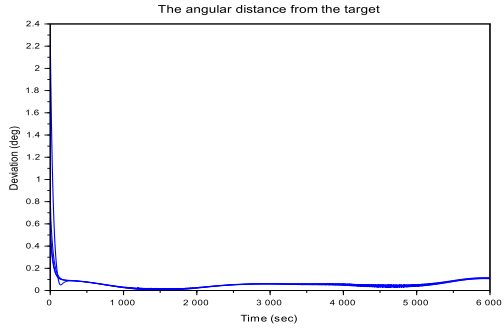

(a) Attitude error

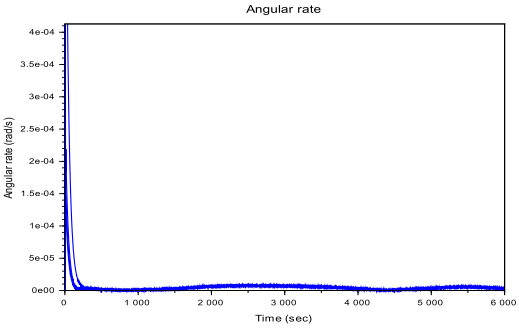

(b) Angular rate error

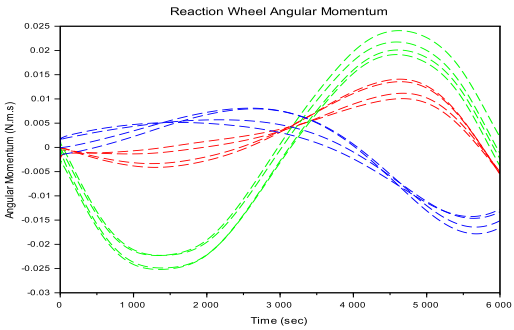

(c) Angular momentum accumulated on reaction wheels

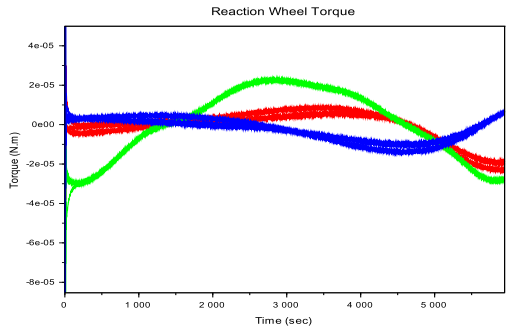

(d) Torque applied by reaction wheels

Figure 5.9.: SCAN mode Monte Carlo long duration simulation results

5.3.3. Inertial Pointing Mode

As Section 4.2 suggests, at IPM mode, the satellite should maintain its orientation with respect to the ECI frame, for the purpose of making observations of predefined space objects. As a result, unlike SAFE and SCAN modes, the target attitude of the controller should be constant, until the next Telecommand and the target angular velocity should be kept zero. From Table 5.1, it can be implied that IPM mode controller should be the most aggressive controller among others, in order to keep its responsiveness towards disturbances and noises while keeping it in quite narrow control requirements.

Table 5.7 contains the IPM mode controller tuning specific parameters with trial process of Q, R matrices and integral gain. In order to study the worst-case scenario in the context of disturbances, the mission start time was taken from Table 4.5 and the inertial mode initial and target orientations were taken from 4.4 and filled in Table 5.7 as quaternions. The residual satellite magnetic dipole moment parameter is the same with 4.6, since the magnetic field vector displays cyclic behavior on constant attitudes related to inertial frame and therefore, the magnetic dipole moment vector will not have a significant effect on the resultant disturbance torque.

As it may be seen from Table 5.7, the first six cases were allocated for the tuning of LQR controllers, while the last three cases analyze the controller with attitude error integral augmentation. Such augmentation is required, since LQR controller depicted in 5.6 only propagates proportional and derivative control over the attitude error, which results in a non-zero steady-state error due to disturbances [17]. For SAFE and SCAN modes, robustness and having high acceptance prevailed optimality of the controller, and therefore the integral augmentation was not considered for them.

Block Name	Parameter Name	Value	Unit
-	Mission Start Time	9th Apr 2028 08:00:00	UTC+00
Rigid Body	Initial Attitude w.r.t. BF	$\begin{bmatrix}0.8159672 & -0.4068262 & -0.3675664 & 0.1832619\end{bmatrix}^T$ + 0.2 deg rotation around BF X axis	Quaternion Real First
Rigid Body	Initial Angular Velocity w.r.t. BF	$\begin{bmatrix}0.0002015 & 0.0002015 & 0.0002015\end{bmatrix}^T$	rad/sec
-	Target Attitude w.r.t. BF	$\begin{bmatrix}0.8159672 & -0.4068262 & -0.3675664 & 0.1832619\end{bmatrix}^T$	Quaternion Real First
Residual Magnetic	Satellite Residual Magnetic Dipole Moment w.r.t. BF	$\begin{bmatrix}0 & 0 & 1\end{bmatrix}^T$	$A.m^2$
Case 1	LQR Q Matrix LQR R Matrix Attitude Error Integral Gain	$\text{diag}(200, 200, 200, 50000, 50000, 50000)$ $\text{diag}(100000, 100000, 100000)$ $\begin{bmatrix}0 & 0 & 0\end{bmatrix}^T$	-
Case 2	LQR Q Matrix LQR R Matrix Attitude Error Integral Gain	$\text{diag}(500, 500, 500, 50000, 50000, 50000)$ $\text{diag}(100000, 100000, 100000)$ $\begin{bmatrix}0 & 0 & 0\end{bmatrix}^T$	-
Case 3	LQR Q Matrix LQR R Matrix Attitude Error Integral Gain	$\text{diag}(2000, 2000, 2000, 50000, 50000, 50000)$ $\text{diag}(100000, 100000, 100000)$ $\begin{bmatrix}0 & 0 & 0\end{bmatrix}^T$	-
Case 4	LQR Q Matrix LQR R Matrix Attitude Error Integral Gain	$\text{diag}(10000, 10000, 10000, 50000, 50000, 50000)$ $\text{diag}(100000, 100000, 100000)$ $\begin{bmatrix}0 & 0 & 0\end{bmatrix}^T$	-
Case 5	LQR Q Matrix LQR R Matrix Attitude Error Integral Gain	$\text{diag}(1000, 1000, 1000, 50000, 50000, 50000)$ $\text{diag}(100000, 100000, 100000)$ $\begin{bmatrix}0 & 0 & 0\end{bmatrix}^T$	-
Case 6	LQR Q Matrix LQR R Matrix Attitude Error Integral Gain	$\text{diag}(2000, 2000, 2000, 50000, 50000, 50000)$ $\text{diag}(150000, 150000, 150000)$ $\begin{bmatrix}0 & 0 & 0\end{bmatrix}^T$	-
Case 7	LQR Q Matrix LQR R Matrix Attitude Error Integral Gain	$\text{diag}(2000, 2000, 2000, 50000, 50000, 50000)$ $\text{diag}(150000, 150000, 150000)$ $\begin{bmatrix}10^{-3} & 10^{-3} & 10^{-3}\end{bmatrix}^T$	-
Case 8	LQR Q Matrix LQR R Matrix Attitude Error Integral Gain	$\text{diag}(2000, 2000, 2000, 50000, 50000, 50000)$ $\text{diag}(150000, 150000, 150000)$ $\begin{bmatrix}2 \times 10^{-3} & 2 \times 10^{-3} & 2 \times 10^{-3}\end{bmatrix}^T$	-
Case 9	LQR Q Matrix LQR R Matrix Attitude Error Integral Gain	$\text{diag}(2000, 2000, 2000, 50000, 50000, 50000)$ $\text{diag}(150000, 150000, 150000)$ $\begin{bmatrix}1.25 \times 10^{-3} & 1.25 \times 10^{-3} & 1.25 \times 10^{-3}\end{bmatrix}^T$	-

Table 5.7.: IPM mode specific parameters and tuning matrices for each case

Figure 5.10 shows the IPM mode tuning process results. In this figure, the dotted markers show pure LQR controller attempts, dashed lines show the integral controller attempts, and the solid line shows the selected controller case. For the first six cases, the main goal was reaching the controller having the least steady state error, while having the least angular rate overshoot. After reaching the goal at Case 6, the integral gain selection process was begun. Among Case 7,8, and 9, the controller having no overshoot was selected, which is **Case 7**.

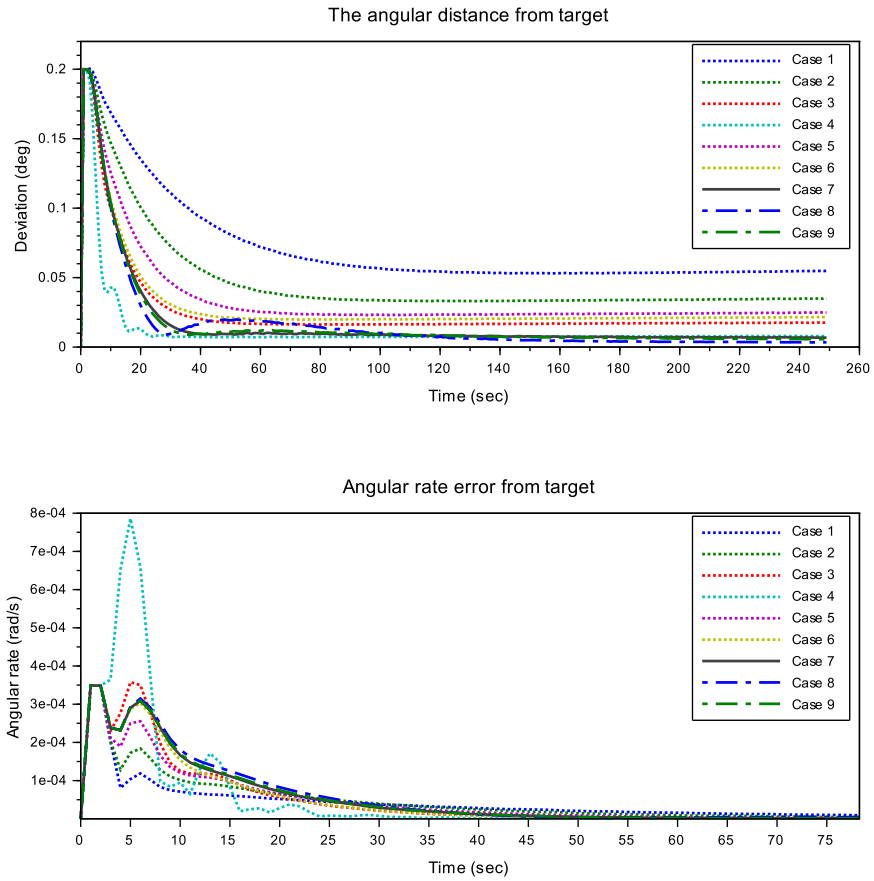

Figure 5.10.: IPM mode LQR tuning process attitude and angular rate errors vs. simulated cases

Scilab *lqr* function generates the optimal gain matrix for the IPM, as it may be seen in Equation 5.23. Nonetheless, integral action causes an augmentation to system matrices, mentioned in Equation 5.14 and the integral gain matrix will be augmented to the optimal gain matrix, in order to obtain eigenvalues of the system. Equation 5.24 gives the optimal gain matrix with the augmentation of integral action. The eigenvalues of the augmented system are given in Equation 5.25. According to the givings in Section 2.4.2, eigenvalues of Equation 5.25 provide Lyapunov and local stability of the selected IPM mode controller, Case 7.

$$K_{IPM} = \begin{bmatrix} 0.1154693 & 5.720 \times 10^{-11} & 0.0003071 & 0.7253738 & -1.103 \times 10^{-10} & 9.657 \times 10^{-10} \\ -6.004 \times 10^{-16} & 0.1154692 & 9.059 \times 10^{-12} & -3.161 \times 10^{-14} & 0.7197806 & -1.094 \times 10^{-11} \\ -0.0003071 & -8.322 \times 10^{-11} & 0.1154698 & -8.008 \times 10^{-10} & 1.099 \times 10^{-10} & 0.7173709 \end{bmatrix} \tag{5.23}$$

$$K_{IPM_{AUG}} = \begin{bmatrix} 10^{-3} & 0 & 0 & 0.1154693 & 5.720 \times 10^{-11} & 0.0003071 & 0.7253738 & -1.103 \times 10^{-10} & 9.657 \times 10^{-10} \\ 0 & 10^{-3} & 0 & -6.004 \times 10^{-16} & 0.1154692. & 9.059 \times 10^{-12} & -3.161 \times 10^{-14} & 0.7197806 & -1.094 \times 10^{-11} \\ 0 & 0 & 10^{-3} & -0.0003071 & -8.322 \times 10^{-11} & 0.1154698 & -8.008 \times 10^{-10} & 1.099 \times 10^{-10} & 0.7173709 \end{bmatrix} \tag{5.24}$$

$$\lambda_{IPM_{AUG}} = \begin{bmatrix} -0.3334071 \\ -0.3561225 \\ -0.3490485 \\ -0.0911548 \\ -0.0909067 \\ -0.0909731 \\ -0.0098443 + 0.0000291i \\ -0.0098443 - 0.0000291i \\ -0.0098413 \end{bmatrix} \tag{5.25}$$

The Monte Carlo campaign was started after selecting the controller parameters from Case 7. Table 5.8 shows the magnitude range of controller parameters to be used in 1080 short, 4 long time duration Monte Carlo simulations. The attitude and angular rate error values were taken from Table 5.1 and the maximum moment of inertia matrix off-diagonal element magnitude was taken from Table 4.2. In order to have maximum magnetic disturbance, the magnitude of magnetic dipole moment is given as the maximum value only, $1 A.m^2$, according to Table 4.2. According to the simulation results given in Figure 5.10, controller parameters from Case 7 were proven to meet controller requirements of Table 5.1 and display stabilizing behavior in all cases. By looking at Figure 5.12a, 5.12b, and 5.12d, it might be inferred that IPM controller works close to its optimal point because the controller reaches noise level at steady state.

Parameter Name	Minimum Value	Maximum Value	Unit
The difference from target attitude	0	0.2	deg
The difference from target angular rate	0	0.02	deg
Moment of Inertia matrix Off-Diagonal elements	0	0.167	$kg.m^2$
Residual magnetic dipole moment	1	1	$A.m^2$

Table 5.8.: IPM mode Monte Carlo simulation input ranges in magnitude

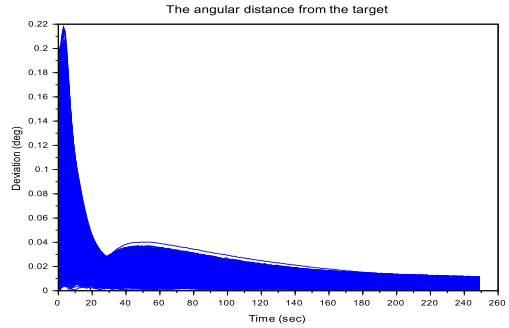

(a) Attitude error

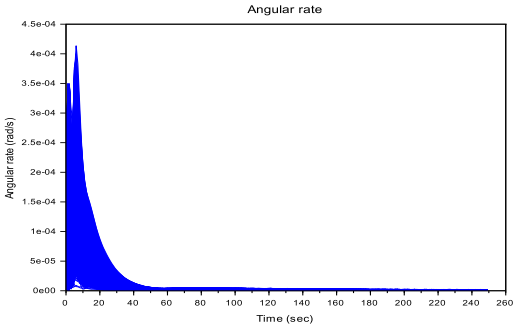

(b) Angular rate error

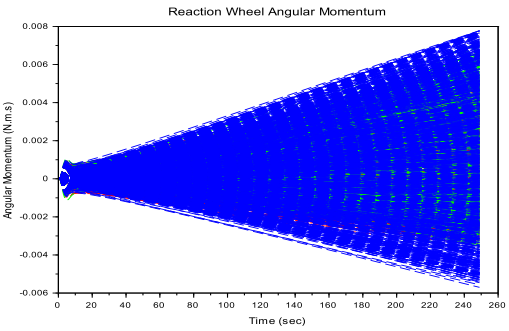

(c) Accumulated angular momentum on reaction wheels

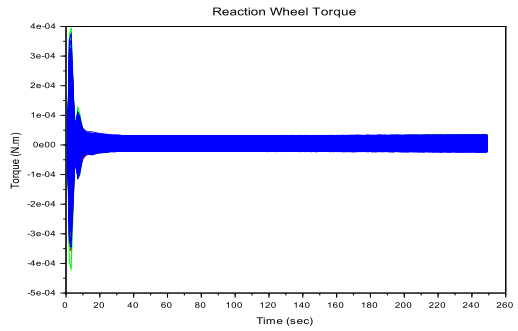

(d) Torque applied by reaction wheels

Figure 5.11.: IPM mode Monte Carlo short term simulation results

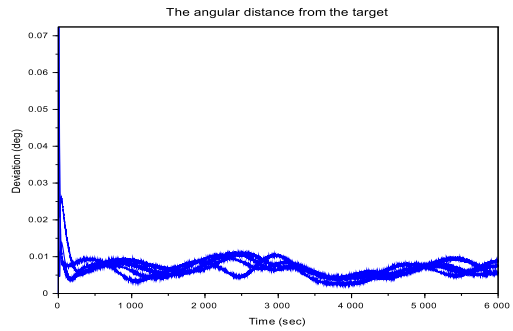

(a) Attitude error

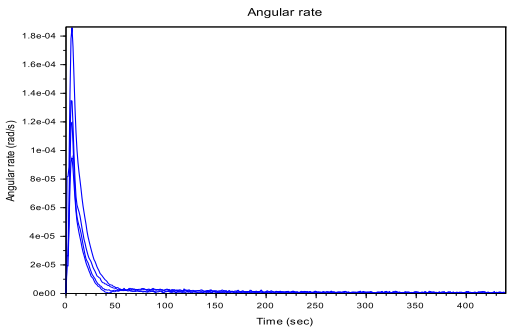

(b) Angular rate error

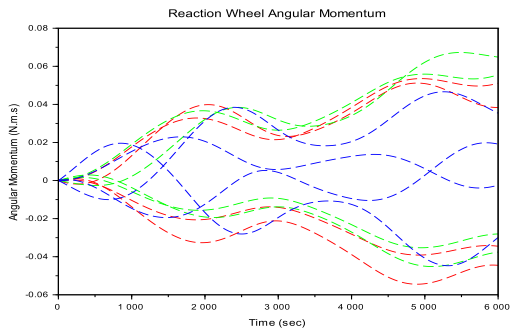

(c) Accumulated angular momentum on reaction wheels

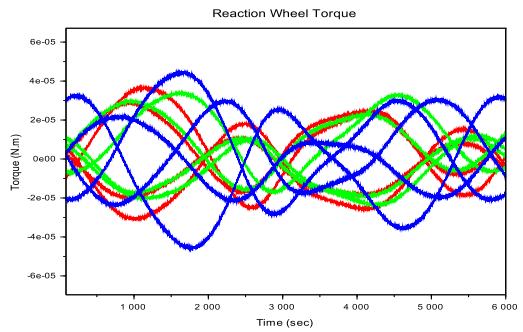

(d) Torque applied by reaction wheels

Figure 5.12.: IPM mode Monte Carlo long term simulation results

5.4. Coarse and Fine Acquisition Mode

According to Section 4.2, under CAM mode, the satellite makes the transition from any attitude to SAFE mode. FAM mode operates the transition from any nominal mode to another nominal mode. According to Table 5.1, SCAN and IPM modes require more accuracy and effort than SAFE mode, and therefore, CAM mode is supposed to be more robust and require less effort than FAM mode. Wie suggests a quaternion feedback controller, which was proven to be globally asymptotically stable, for the execution of rotational maneuvers, which is shown in Equation 5.26 [17]. ACS utilizes Equation 5.26 in CAM mode and the usage of the same algorithm will be tried on FAM mode also, in order to keep the generality. Notice that, the utilization of LQR controllers on linearized systems, like nominal operation modes, is not possible, since the initial attitude might be the exact opposite to the target attitude. In other words, the initial attitude error could be larger than the level that the small angle approximation applies, which may result in deviation from the equilibrium point of linearization.

$$\boldsymbol{u} = -K\boldsymbol{q} - C\boldsymbol{\omega}, \text{ where} \tag{5.26}$$

$$K = ksgn(q_1)I \text{ and } C = diag(c_1, c_2, c_3) \tag{5.27}$$

CAM and FAM tuning simulation block parameters were taken from Table 5.2 and 5.9. The initial attitude and angular velocities for CAM were selected arbitrarily, however, the target attitude should be the exact inverse of the initial attitude with respect to the Body Frame, for the purpose of testing the worst case. The same applies to FAM, nevertheless, the norm of the angular velocity was deliberately set to $0.2\,\text{deg}/s$, in order to test the worst case, given in Table 5.1. The satellite residual magnetic dipole moment was selected arbitrarily as well. Since robustness has more significance than optimality in CAM mode, there was no need for any integrators. The addition of integrals would make steady-state error converge to zero while reducing the stability of the controller. As for FAM controller, because IPM mode requires high accuracy in attitude and angular rate, it should contain integrators. In this thesis work, for the verification of CAM and FAM controllers, tests imposing mode transitions were included in Section 5.6.

Block Name	Parameter Name	Value	Unit
-	Mission Start Time	1st Jan 2028 00:00:01	UTC+00
Rigid Body	Target Attitude w.r.t. BF	$\begin{bmatrix}-0.0466127 & 0.6936885 & 0.1370993 & 0.7055687\end{bmatrix}^T$	Quaternion Real First
Rigid Body	Initial Attitude w.r.t. BF	Inverse of $\begin{bmatrix}-0.0466127 & 0.6936885 & 0.1370993 & 0.7055687\end{bmatrix}^T$	Quaternion Real First
Rigid Body	CAM Initial Angular Velocity w.r.t. BF	$\begin{bmatrix}-0.000287 & 0.0010765 & -0.0001447\end{bmatrix}^T$ (Nadir Pointing)	rad/sec
Rigid Body	FAM Initial Angular Velocity w.r.t. BF	$\begin{bmatrix}-0.0008935 & 0.0033443 & -0.0004495\end{bmatrix}^T$ (Nadir Pointing)	rad/sec
Residual Magnetic	Satellite Residual Magnetic Dipole Moment w.r.t. BF	$\begin{bmatrix}0 & 0 & 1\end{bmatrix}^T$	$A.m^2$
CAM Case 1	K_q K_ω K_Q	$\text{diag}(10^{-4}, 10^{-4}, 10^{-4})$ $\text{diag}(10^{-1}, 10^{-1}, 10^{-1})$ 0	-
CAM Case 2	K_q K_ω K_Q	$\text{diag}(5\times10^{-4}, 5\times10^{-4}, 5\times10^{-4})$ $\text{diag}(10^{-1}, 10^{-1}, 10^{-1})$ 0	-
CAM Case 3	K_q K_ω K_Q	$\text{diag}(7\times10^{-4}, 7\times10^{-4}, 7\times10^{-4})$ $\text{diag}(10^{-1}, 10^{-1}, 10^{-1})$ 0	-
CAM Case 4	K_q K_ω K_Q	$\text{diag}(10^{-3}, 10^{-3}, 10^{-3})$ $\text{diag}(3\times10^{-1}, 3\times10^{-1}, 3\times10^{-1})$ 0	-
CAM Case 5	K_q K_ω K_Q	$\text{diag}(1.25\times10^{-3}, 1.25\times10^{-3}, 1.25\times10^{-3})$ $\text{diag}(3\times10^{-1}, 3\times10^{-1}, 3\times10^{-1})$ 0	-
FAM Case 1	K_q K_ω K_Q	$\text{diag}(1.25\times10^{-3}, 1.25\times10^{-3}, 1.25\times10^{-3})$ $\text{diag}(3\times10^{-1}, 3\times10^{-1}, 3\times10^{-1})$ $\text{diag}(10^{-4}, 10^{-4}, 10^{-4})$	-
FAM Case 2	K_q K_ω K_Q	$\text{diag}(1.25\times10^{-3}, 1.25\times10^{-3}, 1.25\times10^{-3})$ $\text{diag}(3\times10^{-1}, 3\times10^{-1}, 3\times10^{-1})$ $2\times\text{diag}(10^{-5}, 2\times10^{-5}, 2\times10^{-5})$	-
FAM Case 3	K_q K_ω K_Q	$\text{diag}(1.25\times10^{-3}, 1.25\times10^{-3}, 1.25\times10^{-3})$ $\text{diag}(3\times10^{-1}, 3\times10^{-1}, 3\times10^{-1})$ $4\times\text{diag}(10^{-5}, 4\times10^{-5}, 4\times10^{-5})$	-
FAM Case 4	K_q K_ω K_Q	$\text{diag}(1.25\times10^{-3}, 1.25\times10^{-3}, 1.25\times10^{-3})$ $\text{diag}(3\times10^{-1}, 3\times10^{-1}, 3\times10^{-1})$ $\text{diag}(5\times10^{-5}, 5\times10^{-5}, 5\times10^{-5})$	-

Table 5.9.: CAM and FAM mode specific parameters and tuning matrices for each case

The tuning simulation results for CAM mode are shown in Figure 5.13. Examining the figure, the spiky behavior in Case 3 takes attention. The reason for those spikes is having the angular rate that goes beyond CAM mode and ACS enters in DTM mode until reducing the angular rate to the CAM mode acceptance level, which occurs at approximately $t = 1400sec$. Due to such spiky behavior, Case 3 was descoped from the selection. Case 1 displays a slow approximation to the target while requiring larger reaction wheel angular momentum accumulation than the remaining three cases. Thus, Case 1 was eliminated from the selection. Among the remaining cases, **Case 5** was selected since it reaches a steady state sooner than others. In 3000 seconds, Case 5 has the steady state error less than 3 deg and 5.73 deg $/s$, which is quite below SAFE mode entry condition, according to Table 5.1.

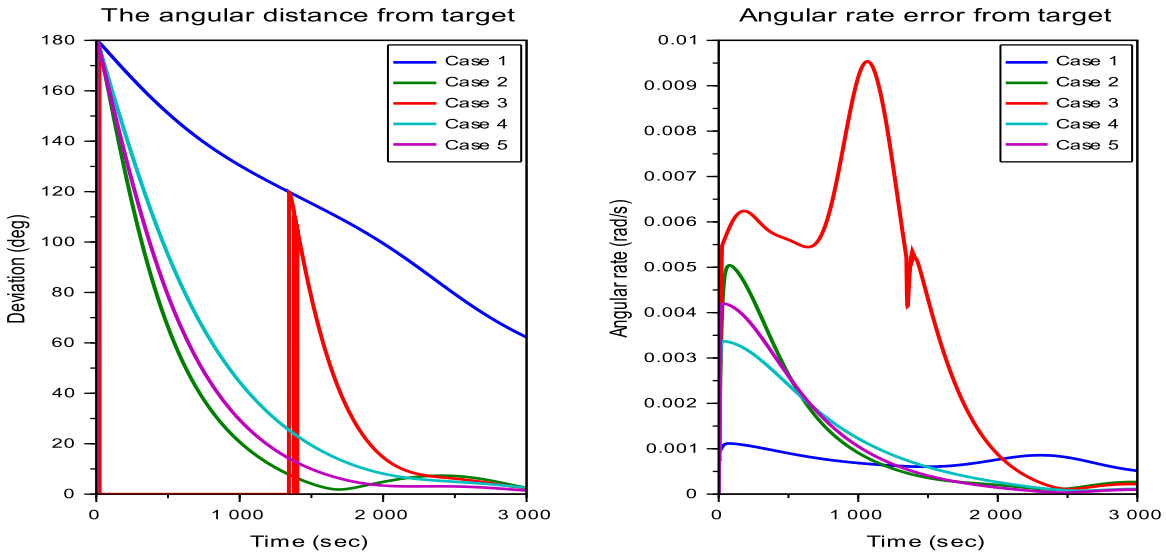

(a) Attitude and angular rate errors

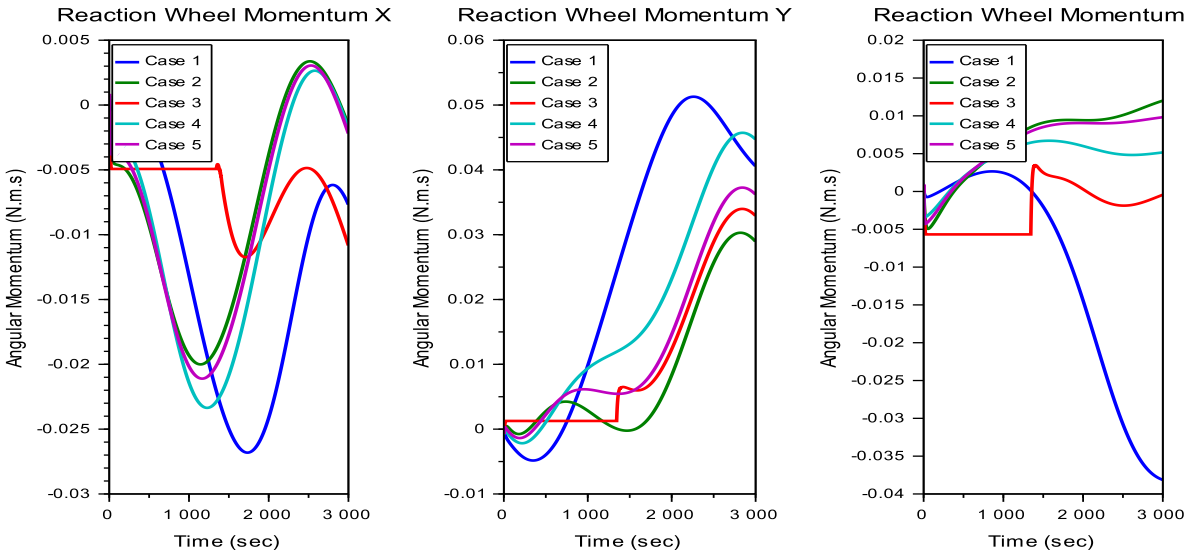

(b) Accumulated angular momentum on reaction wheels

Figure 5.13.: CAM mode controller tuning simulation results

Figure 5.14 illustrates the FAM mode controller parameter tuning results. As seen from Table 5.9, the K_q and K_ω parameters of these four cases were the same with the CAM mode selected controller parameters, Case 5. During the tuning process, only the coefficient of the integrator was varied. From Figure 5.14, it can be deduced that Case 1 displays more oscillating behavior than others and therefore, it is removed from the selection. Among the others, **Case 4** was selected since it reaches the steady state earlier than others and its steady state error is around 0.1 deg, which is below the SCAN and IPM mode entry conditions, according to Table 5.1.

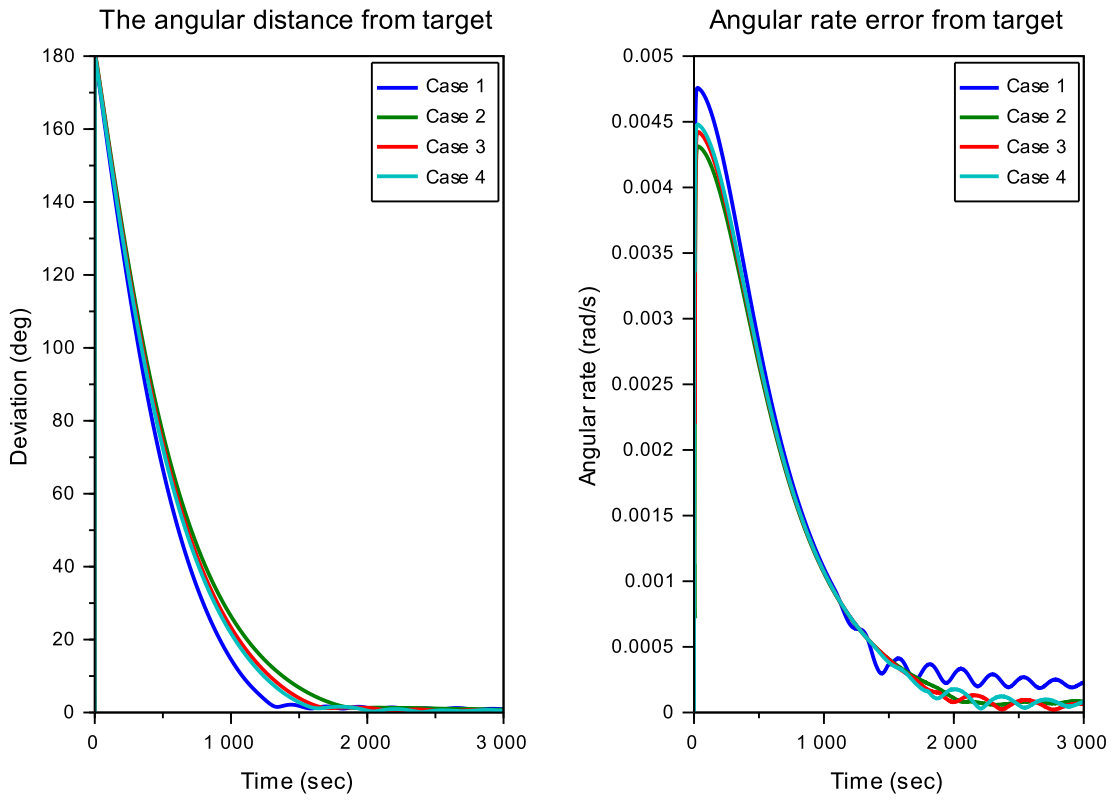

(a) Attitude and angular rate errors

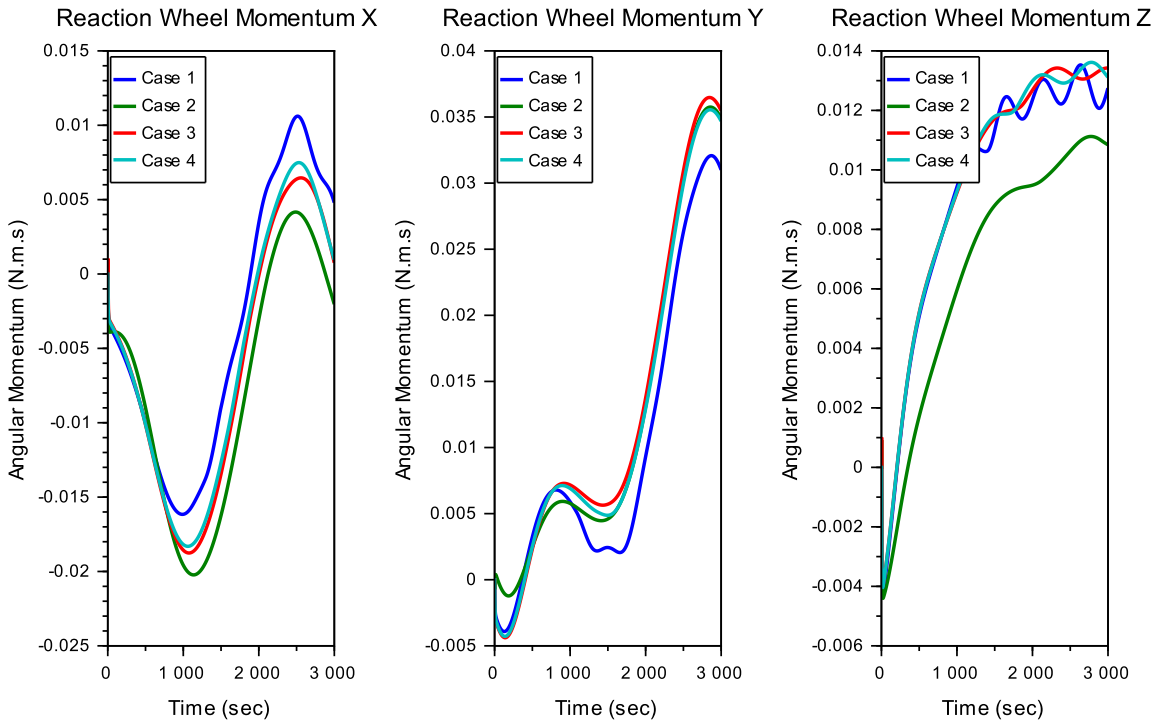

(b) Accumulated angular momentum on reaction wheels

Figure 5.14.: FAM mode controller tuning simulation results

5.5. Momentum Dumping

In this thesis work, ACS utilizes magnetorquers, in order to extract angular momentum deposited, because of executing attitude maneuvers or stabilizing the satellite against disturbances by reaction wheels. When magnetorquers apply counter-acting torque against the overall reaction wheels' angular momentum vector, reaction wheels will try to compensate such torque, which results in momentum dumping. Thus, Equation 3.31 might be rewritten to reach counter-acting magnetic torque against reaction wheels overall momentum vector, by Cross Product Law [51]. Equation 5.29 shows the required counter-acting torque, according to Chen [51]. This equation may be simplified more to Equation 5.30, since the desired orbit is close to the circular orbit, that means the magnitude of magnetic field vector is not expected to display huge variations.

$$\boldsymbol{T_{mt}^{B}} = \boldsymbol{m_{mt}^{B}} \times \boldsymbol{B^{B}} \tag{5.28}$$

$$\boldsymbol{m_{mt}^{B}} = -K\frac{\left(\boldsymbol{H_{rw}^{B}} \times \boldsymbol{B^{B}}\right)}{B^{B}} \tag{5.29}$$

$$\boldsymbol{m_{mt}^{B}} = -K_{md}\left(\boldsymbol{H_{rw}^{B}} \times \boldsymbol{B^{B}}\right) \tag{5.30}$$

The Xcos simulation diagram for momentum dumping demonstration is given in Figure A.14. Between magnetometer output and magnetorquer input in the diagram, Equation 5.30 was implemented. In Chen's opinion [51], more efficient Momentum Dumping methodologies might be used for the purpose of saving energy, such as LQR Controller and Minimum-Energy Controller (MEC). In Section 4.3.4, the magnetic field disturbance torque was found to be dominant over aerodynamic and gravitational torques, and in Section 5.2, the maximum dipole moment of selected magnetorquers is $1.6 A.m^2$, which is 1.6 times the satellite residual magnetic dipole moment. Thus, these magnetorquers are more than capable of counter-acting the dominant disturbance torques, which highly reduces angular momentum accumulation over time. To conclude, if the energy consumption of magnetorquers is not a significant factor for the design, Cross Product law might be employed safely.

The simulation was executed in IPM mode and its input parameters are selected from Table 5.7 with Case 7, in order to have the most reaction wheel accumulation and disturbance torques. The gain values for the tuning were 10^9, 5×10^8, 0, 10^8, and 2.5×10^7. The reason for the values over 10^7 is the simplification made in Equation 5.30, the attempted gain values should contain $\frac{1}{B^B}$, which is approximately 10^5.

Figure A.9 implies that having the gain value of 10^9 and 5×10^8 causes a substantial fluctuations in attitude and angular rate error values and hence, they are eliminated from the selection. The remaining candidates display similar behavior except accumulated reaction wheel momentum values shown in Figure 5.15b. The gain value of 2.5×10^7 does not cause decay of the angular momentum values of reaction wheels in all three axes, like 10^8. As a result, 10^8 was selected as the momentum dumping proportional controller gain.

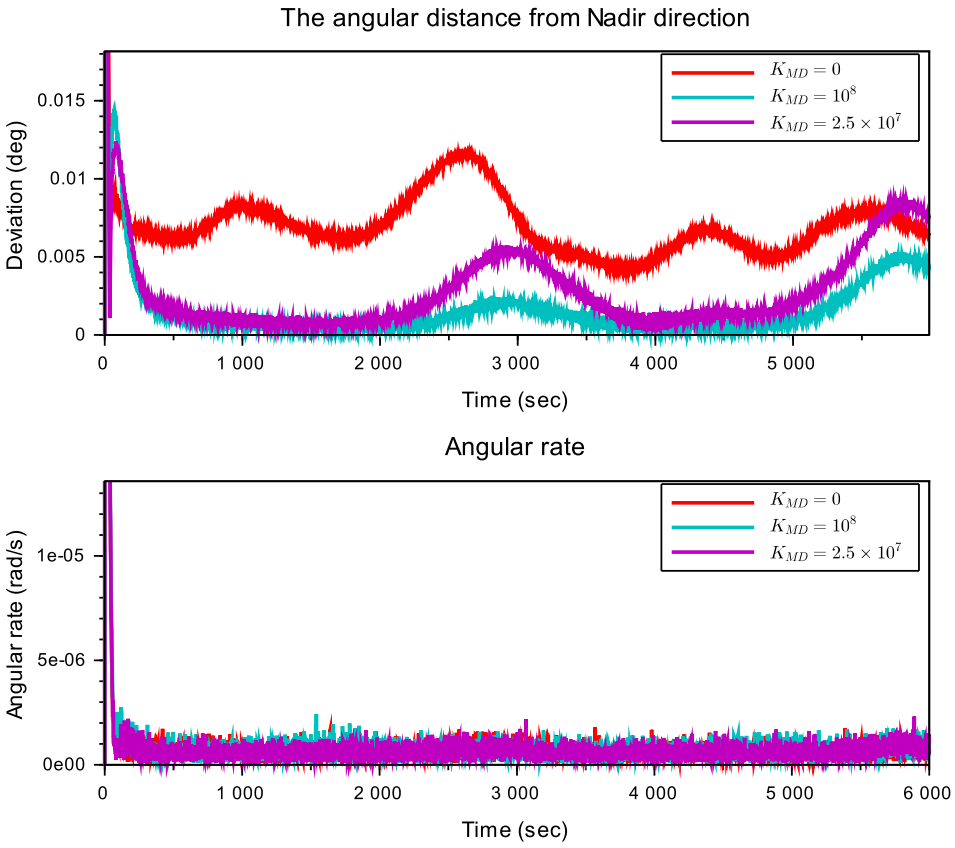

(a) More detailed attitude and angular rate errors

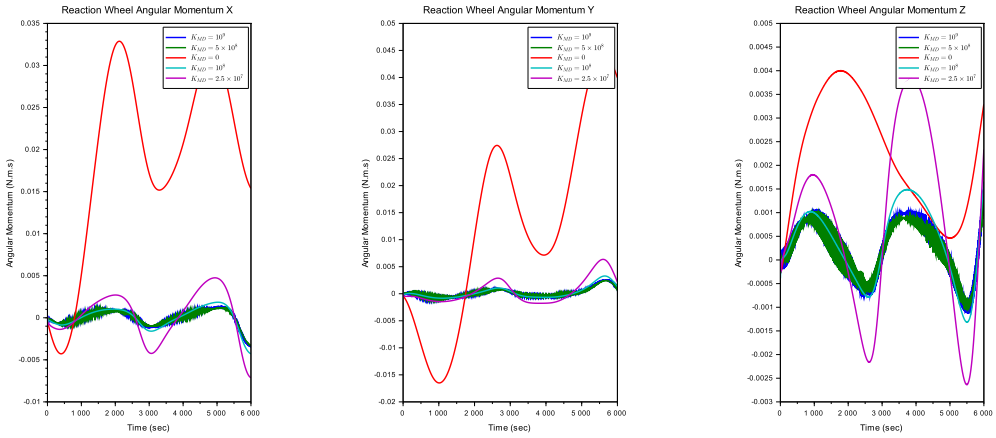

(b) Accumulated angular momentum on reaction wheels

Figure 5.15.: Momentum dumping simulation results

5.6. Multi Mode Experiments

From Section 5.1 to 5.5 all the required controllers in Table 5.1 were designed and validated via Monte Carlo simulations or worst-case analysis. All of the designed controllers in this section are collected under Table 5.10. Although they all worked well in single mode tests, in practice, ACS will make mode transitions automatically or after a Telecommand or any error incidence. As an additional verification method for the overall design and transitional modes (CAM and FAM), multi-mode experiments are carried out.

Mode Name	Controller Type	Parameter Name	Value
DTM	Cross Product	K_ω	$\text{diag}(0.5, 0.5, 0.5)$
CAM	Quaternion PD	K_q	$\text{diag}(1.25 \times 10^{-3}, 1.25 \times 10^{-3}, 1.25 \times 10^{-3})$
		K_ω	$\text{diag}(3 \times 10^{-1}, 3 \times 10^{-1}, 3 \times 10^{-1})$
FAM	Quaternion PID	K_q	$\text{diag}(1.25 \times 10^{-3}, 1.25 \times 10^{-3}, 1.25 \times 10^{-3})$
		K_ω	$\text{diag}(3 \times 10^{-1}, 3 \times 10^{-1}, 3 \times 10^{-1})$
		K_Q	$\text{diag}(5 \times 10^{-5}, 5 \times 10^{-5}, 5 \times 10^{-5})$
SAFE	LQR	Q Matrix	$\text{diag}(5, 5, 5, 10000, 10000, 10000)$
		R Matrix	$\text{diag}(50000, 50000, 50000)$
SCAN	LQR	Q Matrix	$\text{diag}(120, 120, 120, 50000, 50000, 50000)$
		R Matrix	$\text{diag}(100000, 100000, 100000)$
IPM	LQRI	Q Matrix	$\text{diag}(2000, 2000, 2000, 50000, 50000, 50000)$
		R Matrix	$\text{diag}(150000, 150000, 150000)$
		K_Q	$\text{diag}(10^{-3}, 10^{-3}, 10^{-3})$
Momentum Dumping	Angular Momentum P	K_{md}	$\text{diag}(10^8, 10^8, 10^8)$

Table 5.10.: Overview of implemented controllers for all modes

By using block parameters stated in Table 5.10, 5.2, and 5.7, Xcos simulation diagram in Figure A.15 was formed. In the diagram, it might be seen that the momentum dumping algorithm was activated due to the fact that those tests are supposed to undergo a slew maneuver and counteract the disturbances throughout at least half an orbit, which increases the risk of saturation on reaction wheels. At the right bottom of Figure A.15, the integrator mechanism can be shown. This mechanism simply handles the quaternion error integral feedback operation. The edge trigger at the top of integrators is placed, in order to trigger the re-initiation of all the integral values, in the cases of state change. Otherwise, the integral value instantaneously rises to enormous values in mode transitions. Since those integrators are integrating quaternion, they saturate at -1 and 1 and they take $\begin{bmatrix}1 & 0 & 0 & 0\end{bmatrix}^T$ at every re-initiation.

The test scenarios were defined, so that all the possibilities of mode transitions possible throughout the mission could be tested. Since OBC block has no state variables and no input of previous modes, if the attitude and angular rate error is above the required control accuracy level of the mode, ACS enters either CAM or FAM mode, depending on the target mode. If the angular rate of the satellite goes above the DTM mode threshold, ACS automatically switches to DTM mode to reduce the angular rate. Proposed mode change scenarios are visually given in Figure 5.16. Scenarios 1-7 were simulated for 4000 seconds, which is more than half-orbit period, and the target mode change was triggered at 500 seconds later than the start time. Scenario 1 executes the change at the change of target attitude in IPM mode, instead of executing mode change like other scenarios. At Scenario 8, the target mode was set as SAFE mode, throughout the orbit. The mode name-number mapping table is given in Table 5.11.

Mode Name	SAFE	SCAN	IPM	CAM/FAM	DTM
Number	1	2	3	4	5

Table 5.11.: Control mode vs. simulation number mapping

The simulation results are visualized in Figure 5.17. In this figure, except Scenario 8, the mode transition trigger at $t = 500sec$ might be observed. At Scenario 8, the controller managed to do the automatic switch to CAM mode. According to the attitude and angular rate error plots, controllers work as expected and the mode transition had no effect on their operation. In all scenarios, ACS decays to zero angular rate and attitude error and all mode transitions were operated successfully.

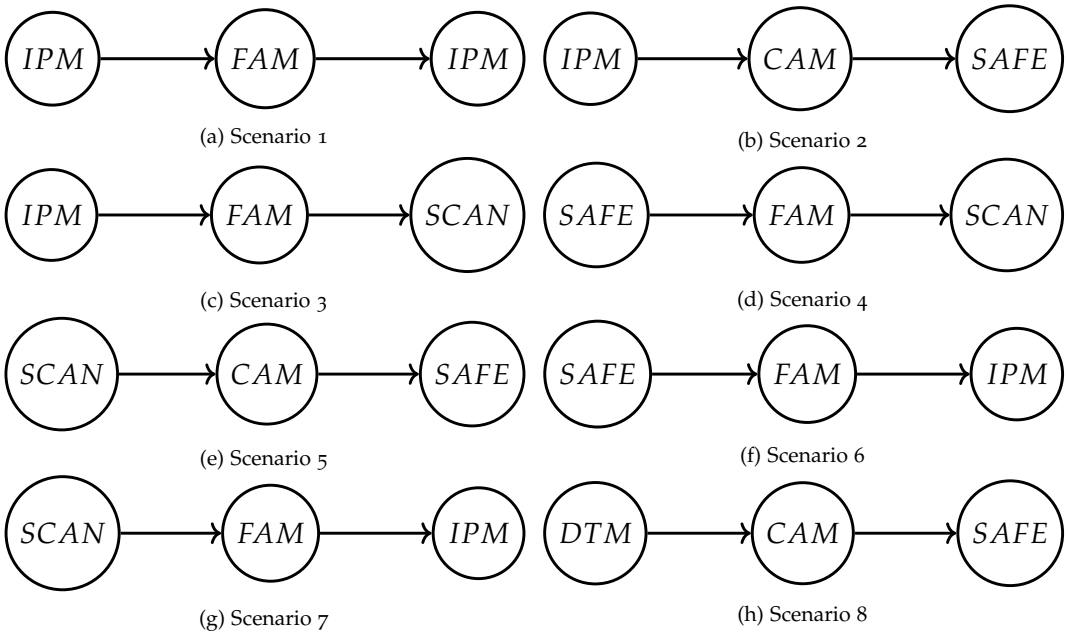

Figure 5.16.: Mode transition scenarios

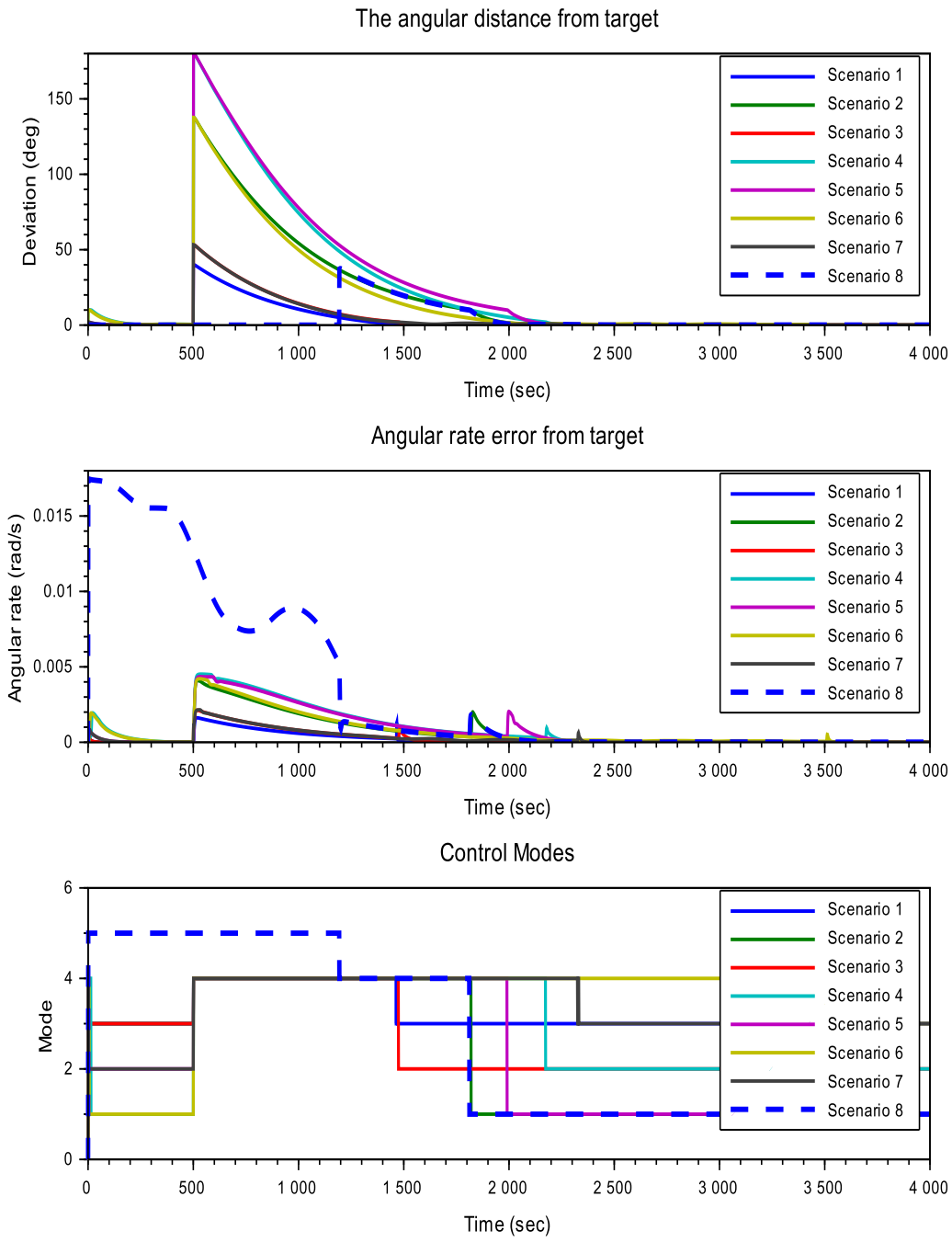

Figure 5.17.: Mode transition plots of Scenarios 1-8

6. Discussion

This thesis work comprises the design of AOCS controllers to be implemented with Scilab programming language and to be simulated in Xcos environment. From desired mission attitude control parameters from Section 4.1 and 4.2, all operational modes required for the autonomy and competence of the AOCS were created. Regarding these controller modes, adequate controller mode transition schemes and their conditions were introduced. The worst-case initial and environmental conditions were determined in Section 4.3, after a detailed analysis. Taking the controller requirements and disturbances into account, AOCS hardware was selected, as it may be seen in Table 4.13. Then, desired controllers for both nominal and transitional modes were designed in Section 5, and all of the resultant controller parameters are gathered into Table 5.10. These controllers were extensively tested, for the verification of their functionality and robustness against environmental and internal variations.

Observing Figure 5.6c, 5.9c, and 5.12c, one may infer that the accumulated angular momentum, after an orbital period, on reaction wheels were the highest at IPM mode. This is the proof of sanity of disturbance analysis made in Section 4.3, since the date and initial attitude parameters of IPM mode simulations were taken from the results of Tables 4.4 and 4.5.

De-Tumbling Mode controller designed in Section 5.2 was simulated in the worst environmental conditions possible, in means of disturbance torques. In the beginning, the choice in between three de-tumbling strategies mentioned in Section 5.2 had to be made. Since angular momentum storage during the de-tumbling phase was not the desired situation for reaction wheels and therefore B-Dot and Cross Product methods, which are rather slower than actuating reaction wheels, remained. Nevertheless, by looking at the plot of the result of Cross Product method in Figure 5.3, AOCS managed to damp the angular velocity of the satellite to $0.05\,\mathrm{deg}/s$, before 4000 seconds passed. Table 5.1 states that CAM mode, which always comes after DTM mode, accepts the angular rate magnitude lower than $0.2\,\mathrm{deg}/s$. Hence, one may conclude that this is the indication of DTM controller success.

Nominal operational mode controllers (SAFE, SCAN, IPM) were designed under Section 5.3. Table 4.3 points out that SAFE mode controller is the most robust and IPM mode controller is the most accurate among them. Therefore, LQR controller was sufficient for SAFE and SCAN modes, while LQR controller for IPM mode was claimed and proven to be adequate. As indicated in Section 2.4.4, the inclusion of an integrator eventually makes the steady-state error zero. However, there was no integrator controller for SAFE

and SCAN modes, and therefore, the non-zero steady-state error was expected. For this reason, during the tuning process of all modes, by using mode entry condition parameters from Table 5.1, the maximum attitude deviation from the target attitude was provided to observe the maximum steady-state error from these controllers. In Equations 5.17b-5.17h, Bryson's Rule was applied in the selection for initial tuning parameters for all controllers [50]. The final Q and R matrices collected in Table 5.10 prove the sanity of initial tuning parameters determined by Bryson's Rule.

The robustness of nominal mode controllers was examined by Monte Carlo simulations. 1080 short-duration and four long-duration simulation cases were randomly generated for each mode, under the limits defined in Table 5.1. Randomly generated variations include moment of inertia, residual magnetic dipole moment vector, initial attitude, and initial angular rate with respect to the inertial frame. It might be remarked that, Figure 5.5a-5.5b and Figure 5.8a-5.8b display similar behavior since they are affected by disturbances in similar ways and they produce non-zero steady-state error. From these figures, one might conclude that no Monte-Carlo case resulted in unstable behavior, and hence, SAFE and SCAN mode controllers were proven to be robust. Furthermore, the angular momentum Z-axis reaction wheel plots from Figures 5.6c and 5.9c are the opposite of each other, which is sourced from having the opposite attitudes. A similar behavior appears in Figures 5.6d and 5.9d, for the same reason.

As for IPM mode, the implementation of LQR had a positive effect on results. From Figure 5.12a, it might be implied that the controller almost works at the noise level, which means the controller is optimized for steady-state error. Figure 5.11a and 5.11b are the proof of the robustness and stability of this controller and LQR implementation.

Considering CAM and FAM modes, like DTM, simulation parameters were selected in a way that maximum external disturbances occur in the simulation time. Moreover, the initial and target attitude of the simulation were selected, so that the satellite would make the maximal rotation, 180 deg. CAM mode controller should be more loose than FAM, since CAM mode aims only for SAFE mode. Table 5.1 implies SAFE mode has the widest entry conditions among other nominal operation modes, while FAM mode targets more precise modes. Therefore, remembering Table 5.1, CAM mode controller uses Quaternion PD controller, while Quaternion PID controller was found suitable for FAM mode. From Case 5 plots of Figure 5.13, it might be inferred that the selected controller could reduce the angular error down to 1.5 deg and the angular rate error to 0.0057 deg $/s$. Remembering that this simulation was run under the worst environmental and internal parameters possible, and having the steady state error in Figure 5.13 lower than the entry parameters of SAFE mode, the controller was found to be capable of doing the attitude maneuver from any attitude to SAFE mode.

FAM mode requires more accuracy than CAM mode and CAM mode was found to be capable of reducing the attitude error down to 1.5 deg maximum. In order to have more accuracy for FAM mode, as a first approach, integral controllers were added, without changing parameters found for CAM mode. In Case 4 plots of Figure 5.14, this approach was proven to be correct because the attitude error was decreased to 0.1 deg

and the angular velocity error to 0.0017 deg. According to Table 5.1, these error values are sufficient conditions to enter the IPM mode, which requires the most pointing accuracy.

Most AOCS systems implement their momentum dumping algorithm, which should be run besides all the modes except DTM, in order to dampen the angular momentum accumulated on reaction wheels. Figure 5.12c indicates such necessity since one complete orbiting around the Earth results in angular momentum accumulation on the Y-axis by $0.075 N.m.s$, which is 75 percent of the selected reaction wheel angular momentum capacity, as Table 4.13 expresses. Figure 5.15b became the evidence of this common practice. This figure performs the clear comparison between momentum-dumped AOCS and not momentum-dumped one. Activating momentum damping with the gain of $K_{MD} = 10^8$ decreased the angular momentum allocation by approximately 93.75 percent on the X-axis reaction wheel, 93.18 percent on the Y-axis, and 75 percent on the Z-axis. From Table 4.11, the selected reaction wheel has the angular momentum capacity of $0.1 N.m.s$. In other words, without the momentum dumping, by having a look at Figure 5.15b Y axis plot, the reaction wheel on the Y axis would saturate in at most two or three orbits. The addition of momentum dumping increased this number to 34 orbits. This itself proves the effectiveness of the current momentum-dumping algorithm. In addition, Figure 5.15a implies that the implementation of momentum-dumping algorithm helps AOCS to have more attitude and angular rate accuracy to the noise level, which may be counted as a side-improvement of momentum dumping algorithm.

In Section 5.6, mode transitions were analyzed, in order to test the practicality of ACS control accuracy definitions in Table 5.1 and controllers designed in Table 5.10. All these tests were carried out in the worst environmental conditions. As it can be seen in Figure 5.16, all possible mode transition scenarios in nominal operation were tested. Figure 5.17 reflects that all mode transitions were handled in half-orbit duration successfully. In OBC, the automatic switch to DTM mode was implemented to dampen the instantaneous angular velocities exceeding the damping threshold. Not switching to DTM mode during acquisition modes or after reaching target modes indicates that all modes work atomic, which means they do not interfere with other modes in their nominal operations.

Conclusion

The main objective of this thesis work is to investigate whether and to which extent ACS system design was possible under Scilab/Xcos framework. After creating *Spacecraft GNC Toolbox* on Scilab, all of the simulation blocks in Chapter 3 were implemented from scratch, under the toolbox. As of 2024, since Scilab is open-source and has a recently growing community, minor discrepancies, bugs, and performance drops occurred during the development of these blocks and simulation diagrams. However, these discrepancies did not cause any delay/block to the development phases. Just as enhancements were undergone on Scilab side, so the *Spacecraft GNC Toolbox* was regularly developed and improved.

At the beginning, of March 2023, the project was set up in Scilab 5.5.2 since CelestLab library could be installed in it and Aerospace Toolbox was working in harmony only with this version and the toolbox has supportive blocks such as Keplerian orbit propagators with J_2, US76 atmospheric density propagator, IGRF12 magnetic field propagator, and so forth. After the successful integration of Fortran codes into Xcos blocks, the atmospheric density and magnetic field blocks of Aerospace Toolbox were deprecated, since:

- By nature, Fortran codes work much faster than Scilab scripts (and most programming languages).
- US76 was replaced with NRLMSISE-00, and IGRF12 was replaced with IGRF13, which are more accurate models, as discussed in Section 3.
- Fortran codes of these models were directly downloaded from the model provider's website, which means these code blocks are not error-prone.
- The project would have less dependency on Aerospace Toolbox, and so Scilab 5.5.2.

During the development phase of the toolbox, migration to Scilab 2023.1.0 was a breaking point. In comparison with simulations run under Scilab 5.5.2, the time elapsed after a single simulation was reduced to one-tenth, which increased the pace of the development process. Only the Keplerian propagators of Aerospace Toolbox were not replaced. Instead after determining the simulation dates causing the worst environmental disturbances, which were detected in Section 4.3 and collected under Table 4.5, the PVT data were created under Scilab 5.5.2 environment and used in simulations with Scilab 2023.1.0. As a result, writing version-free code helped the development process a lot, since the migration process did not cause any fatal errors/discrepancies and the

migration was carried out in a short time.

Scilab/Xcos environment enabled the disturbance analysis in Section 4.3, extensively and comprehensively. It could run the yearly simulations, expressed in Section 4.3.3, without any bugs or errors. As for orientation analysis in Section 4.3.2, after a small modification, the gravity gradient and atmospheric drag blocks could handle 180×90 inputs at the same time and the simulation worked without giving any errors. As expressed in Section 6, the controller design for all modes has resulted in success, and therefore, one can conclude that all of the analysis made under Section 4.3 was accurate and helpful in the selection of adequate hardware.

As *Discussion* section indicates, all of the developed controllers worked accurately, independently, and atomic. These controllers were extensively tested, in means of robustness. Therefore, the designed AOCS is claimed to be ready for further developments and design phases. This thesis work reveals that any kind of attitude control system can be developed with Spacecraft GNC Toolbox under Scilab/Xcos environment. Since Scilab is an open-source software, it is always open to further developments and features.

Future Work

This thesis work accomplished all of its main objectives in a year of work. The main aim of the project was a simulation of the AOCS as close to the real-world system as possible. However, some minor features could not be added to Spacecraft GNC Toolbox. This section aims to be a guideline for further developments.

About simulation block development, the first enhancement would be converting the code language of the most frequently used blocks or blocks inducing high computational costs from Scilab to C/C++ or Fortran. Scilab has the capability of interfacing C/C++ and Fortran functions for a long time and newer versions of Scilab provide an Application Programming Interface (API) for such conversion. In the very early phases of the project, the implementation of blocks written in C language was attempted. In the end, at that time these blocks could not be extensively tested and therefore, this method could not be followed.

Spacecraft GNC Toolbox is found to be capable of simulating ACS in this thesis work. However, the main functionalities of the blocks were simulated and more features can be added to the blocks. For example, the satellite was assumed to be Rigid Body and it contains only a single rigid structure, which can be summarized in a single moment of inertia matrix. Nevertheless, slosh movement, multi-element dynamics, and structural dynamics were ignored in this thesis work. As for sensors and actuators, more error sources could be added and they can have their internal state variables for having more functionalities, like drift errors. As of January 2024, the star tracker block only returns the attitude information with some transformations and noise addition. The Field of View, star catalogs, and lost-in-space situations can be included in Star Trackers. Reaction wheel block does not calculate any friction inside the wheel, which can be included as a feature. Moreover, different sensors and actuators commonly used in AOCS systems, like Sun sensors, Earth sensors, Control Moment Gyroscopes, momentum wheels, and attitude thrusters, might be added to the toolbox.

The toolbox has three sources of disturbances: magnetic, aerodynamic, and gravitational. However, solar radiation torque could be also added, especially for Medium and High Earth Orbit missions. As of January 2023, aerodynamic drag block is only capable of calculating the atmospheric drag on a cube. More sophisticated closed shapes and the utilization of solar panels could be considered while improving atmospheric drag torque block. In addition, the Fortran code of more precise and advanced atmospheric density and gravitational models can be downloaded and imported into the toolbox.

As indicated in Table 5.1, Quaternion feedback and LQR controllers were used in this thesis work. The implementation of robust control methods, like H-infinity or μ-Synthesis controllers, might be considered as further development. Notice that, Scilab 2023 has built-in H infinity functions.

For the simulation, there is an urgent need for Keplerian orbit propagator blocks, as it was in Aerospace Toolbox of Scilab 5.5.2. During the controller development, there was an attempt to implement it, nonetheless, it resulted in error and this attempt was no longer carried on. After that, an orbital control mechanism could be implemented.

As indicated in Section 5.1, there was no attitude observer block, and therefore, synchronized sensor inputs were assumed. The addition of attitude observers could make the simulation closer to reality.

Appendices

A. Appendix

A.1. Solar Cycles

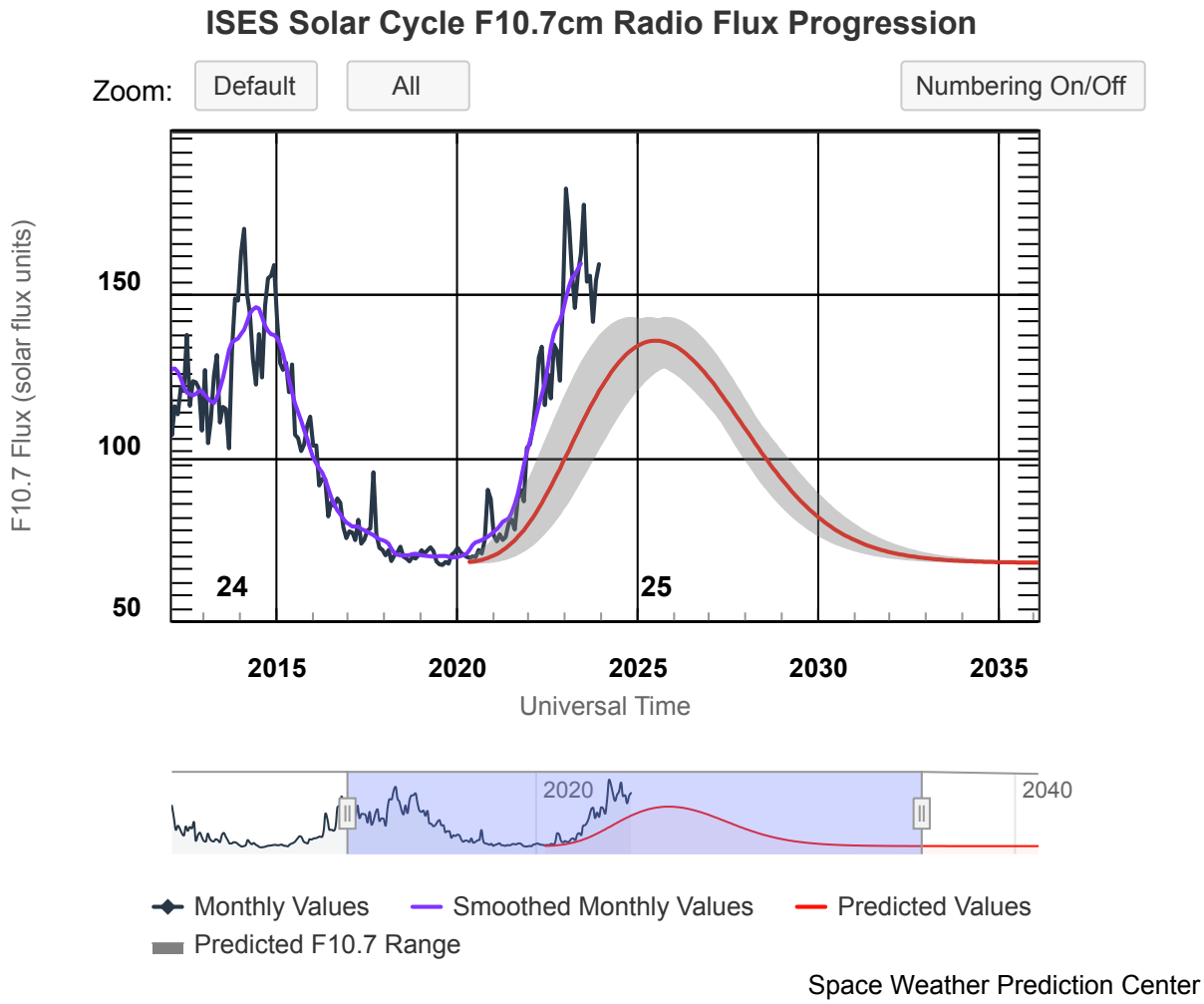

Source: https://www.swpc.noaa.gov/products/solar-cycle-progression

Figure A.1.: F107 Parameter over Solar Cycles

A.2. Spacecraft GNC Toolbox Palette

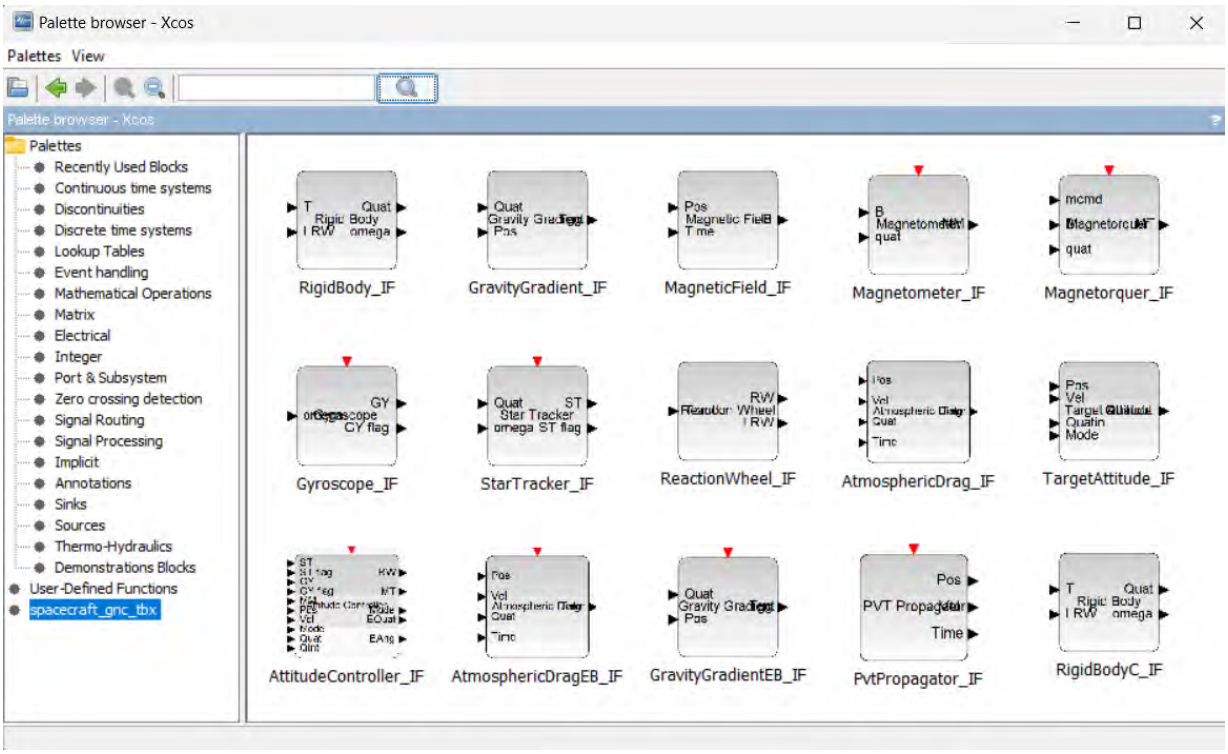

Figure A.2.: Spacecraft GNC Toolbox blocks implemented under Scilab

A.3. Additional Plots for Controllers

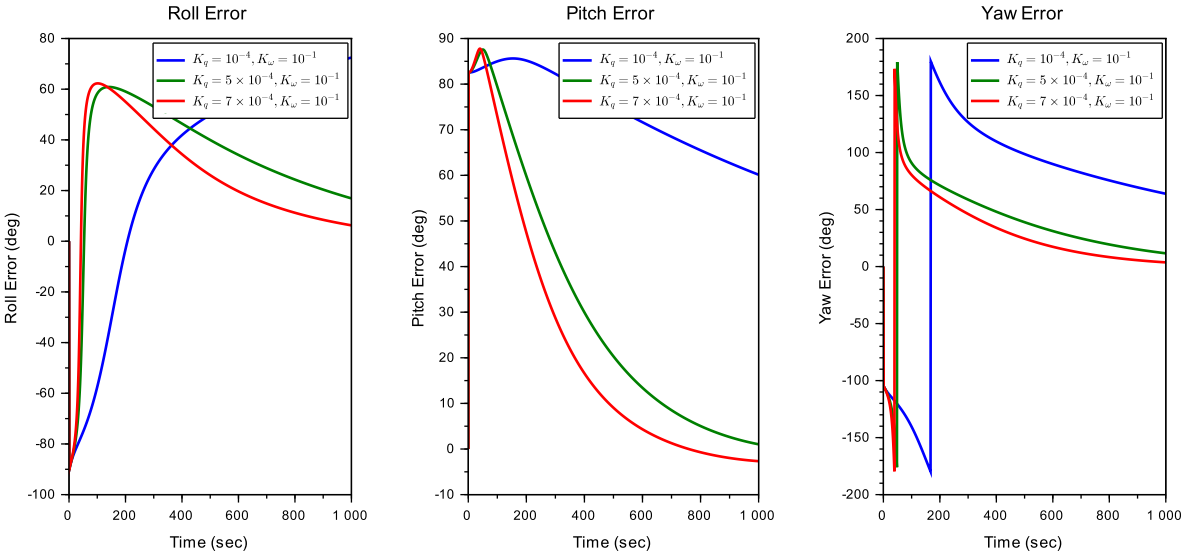

Figure A.3.: Acquisition mode state feedback gain tuning process Roll-Pitch-Yaw angle errors

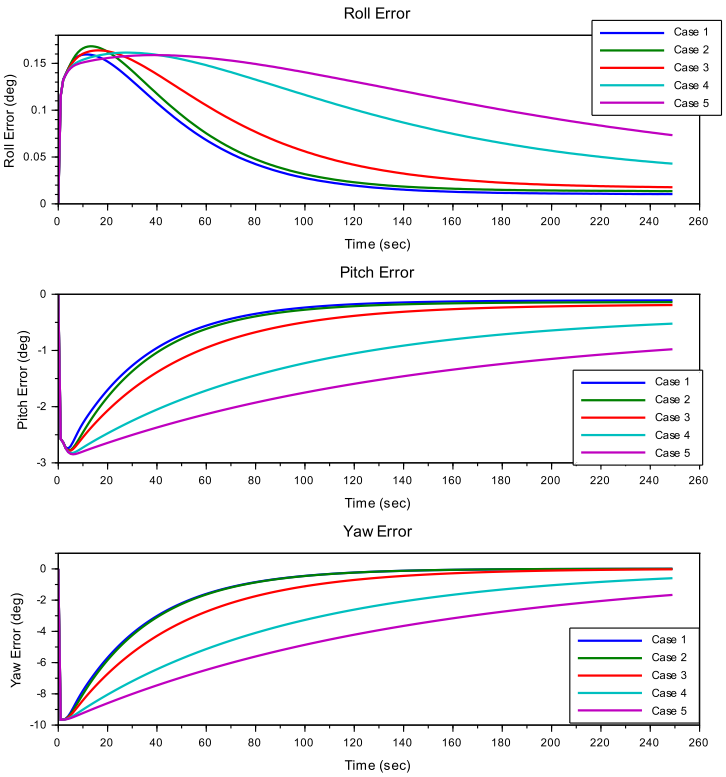

Figure A.4.: SAFE mode LQR tuning process Roll-Pitch-Yaw errors vs. time

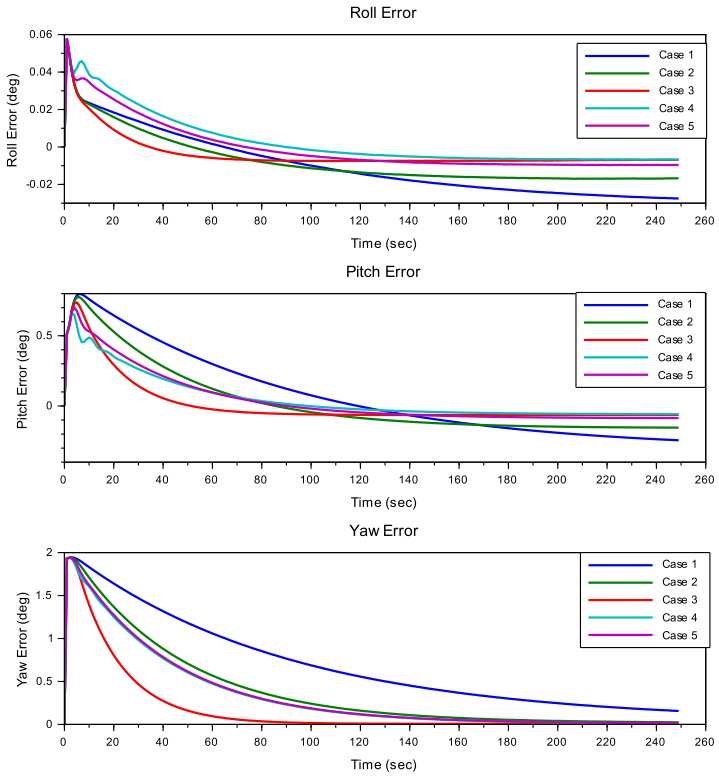

Figure A.5.: SCAN mode LQR tuning process Roll-Pitch-Yaw errors vs. time

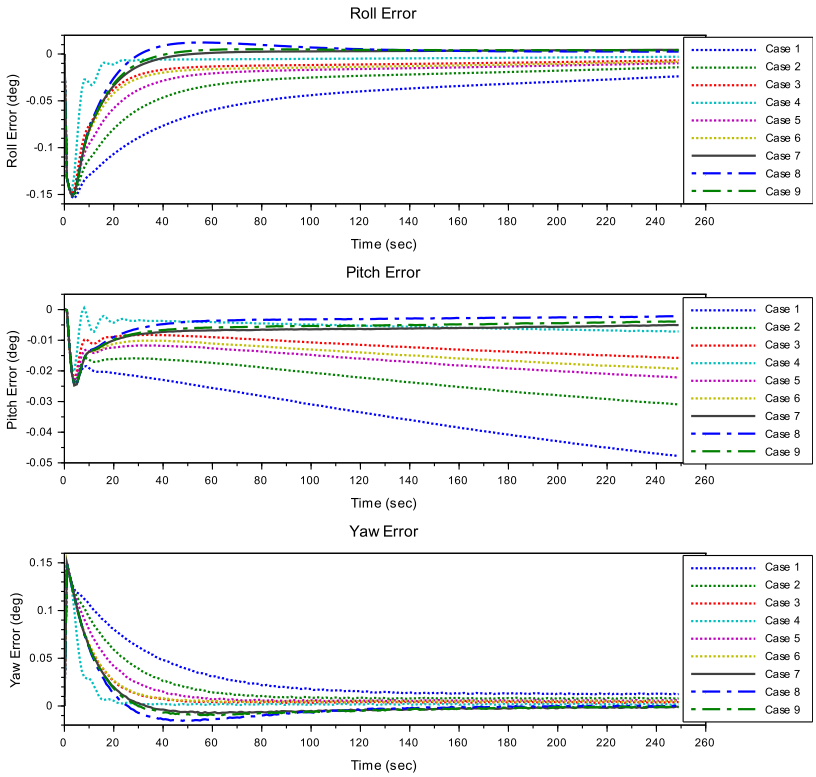

Figure A.6.: IPM mode LQR tuning process Roll-Pitch-Yaw errors vs. time

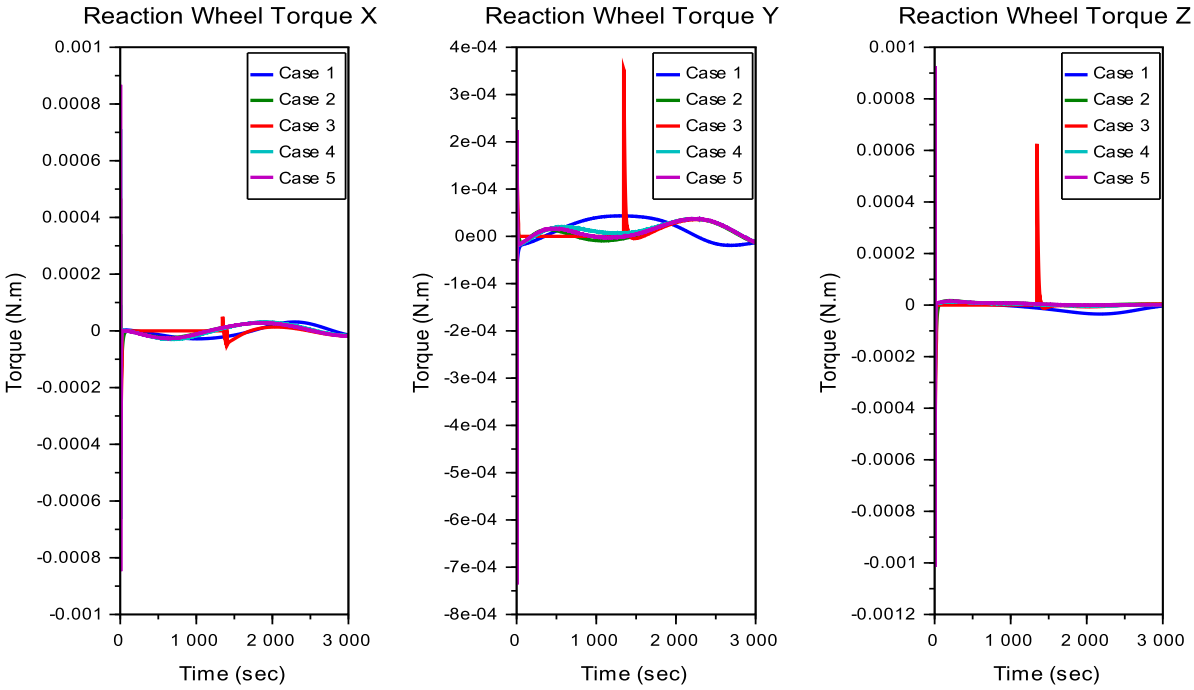

Figure A.7.: CAM mode reaction wheel torque applied

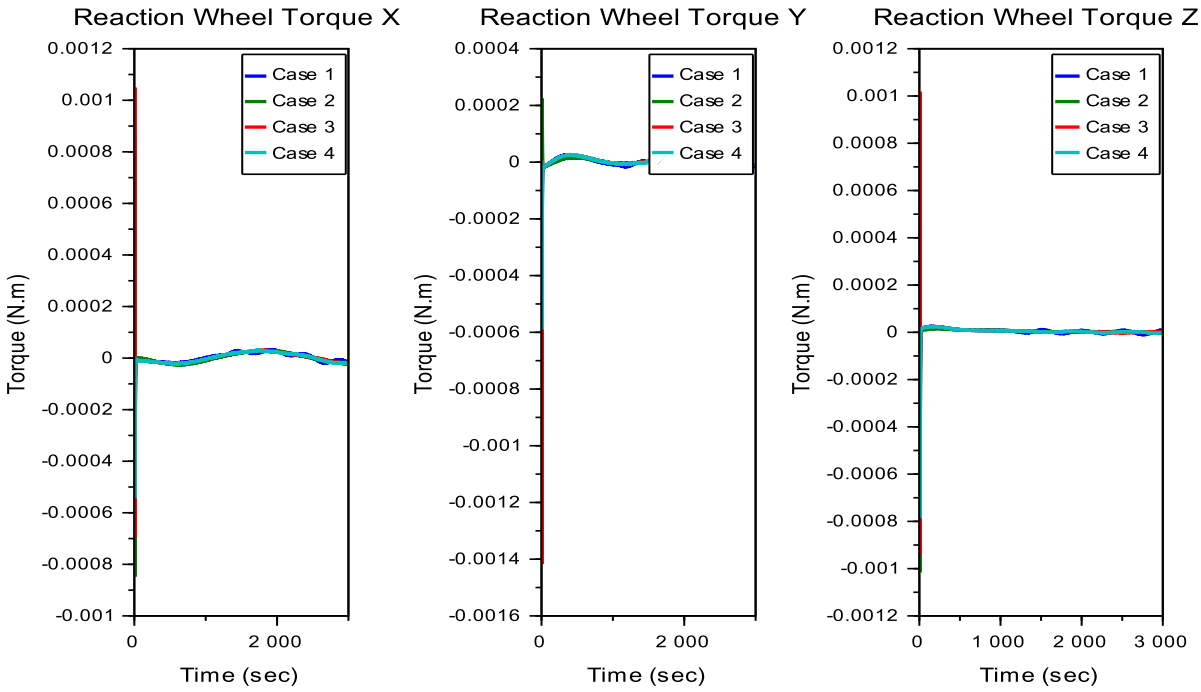

Figure A.8.: FAM mode reaction wheel torque applied

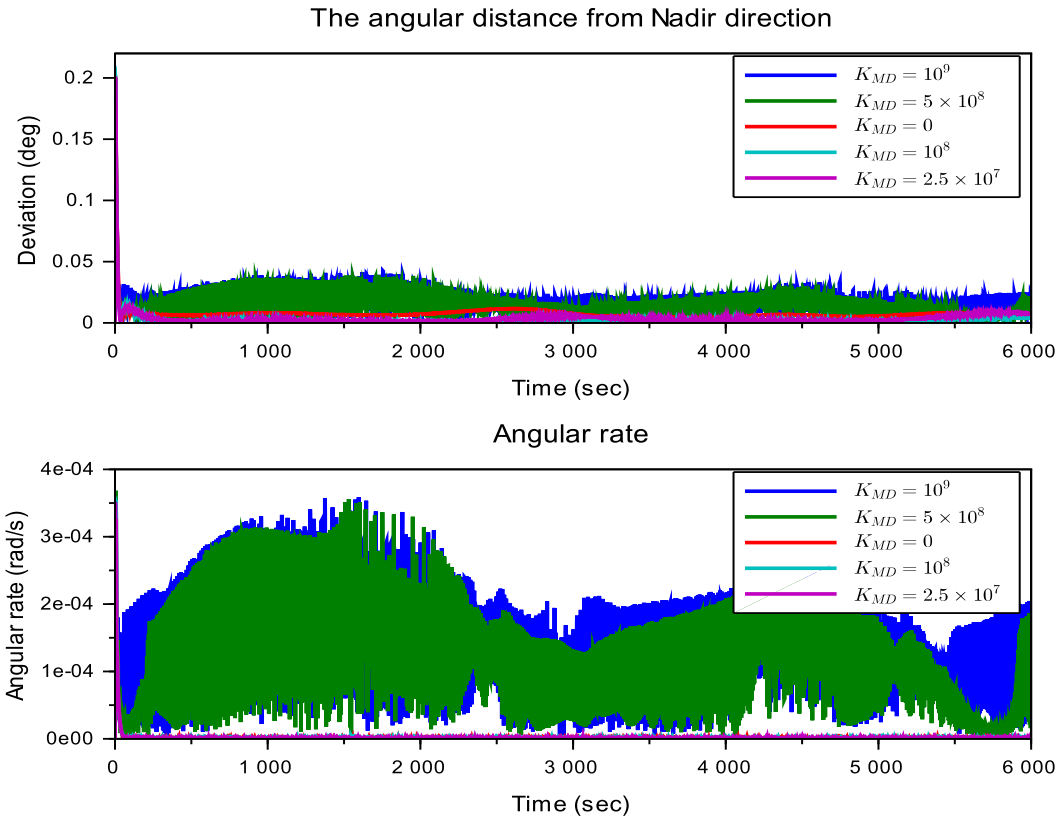

Figure A.9.: IPM mode with momentum dumping attitude and angular rate errors

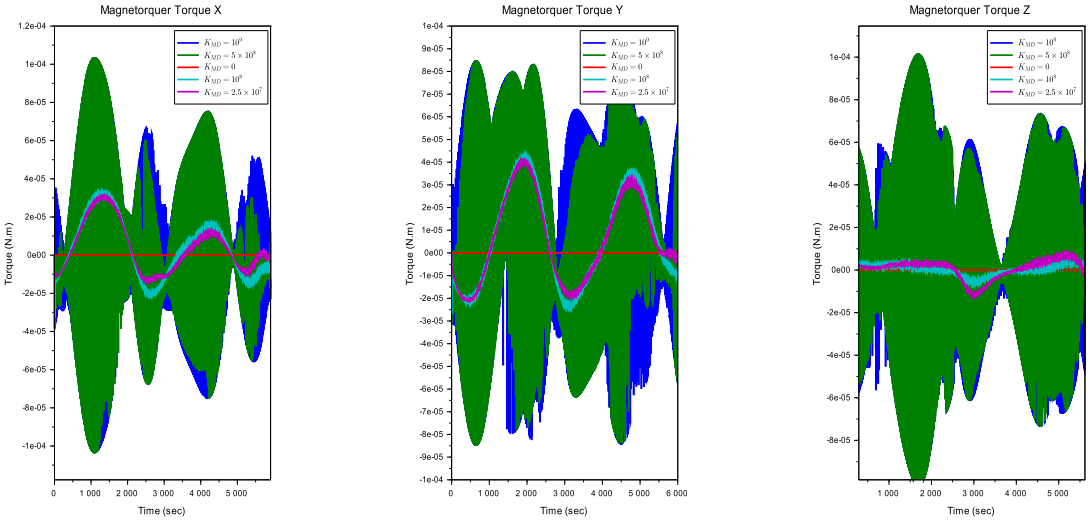

Figure A.10.: IPM mode with momentum dumping applied magnetorquer torque

A.4. Simulation Diagrams

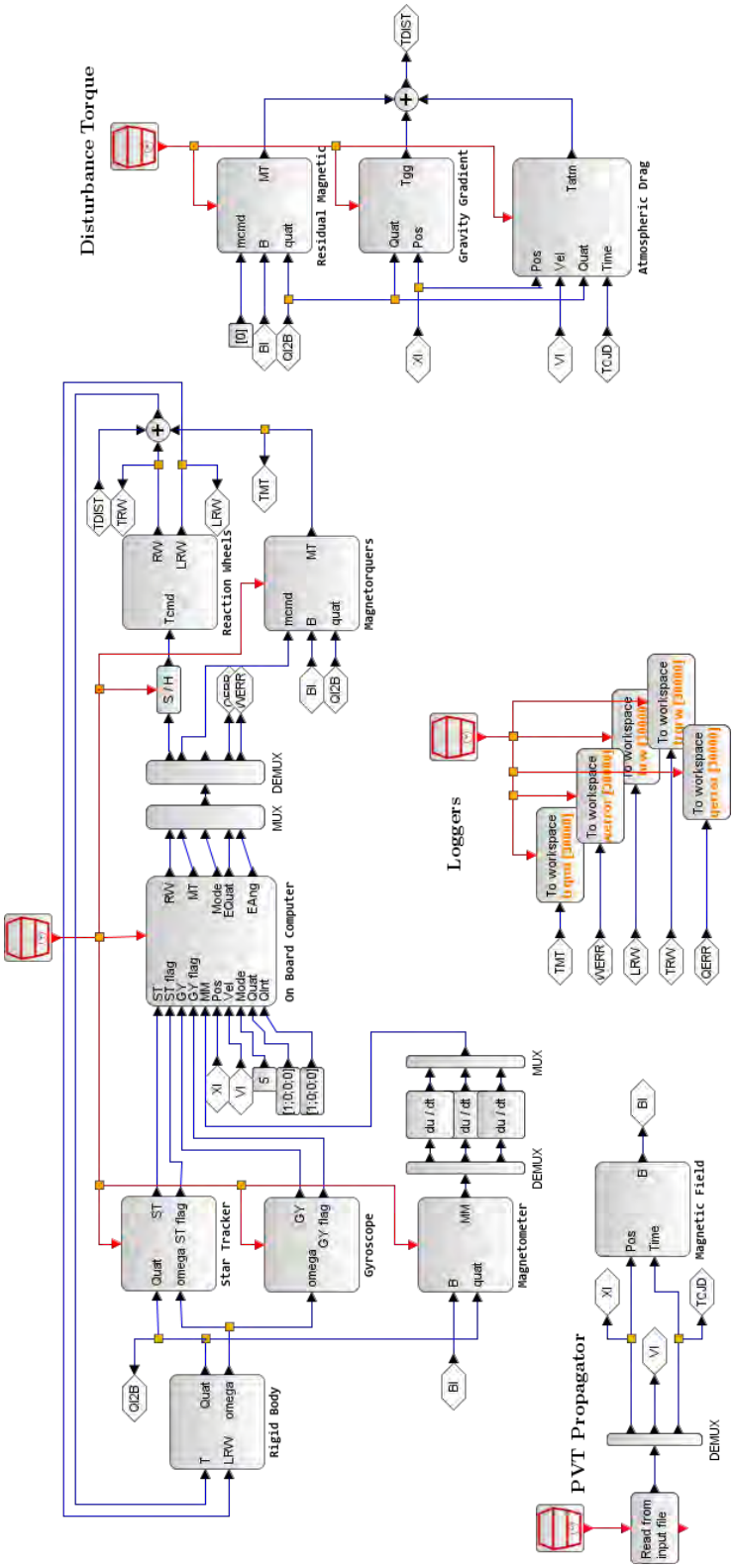

Figure A.11.: De-Tumbling Mode Simulation Diagram for B-Dot method

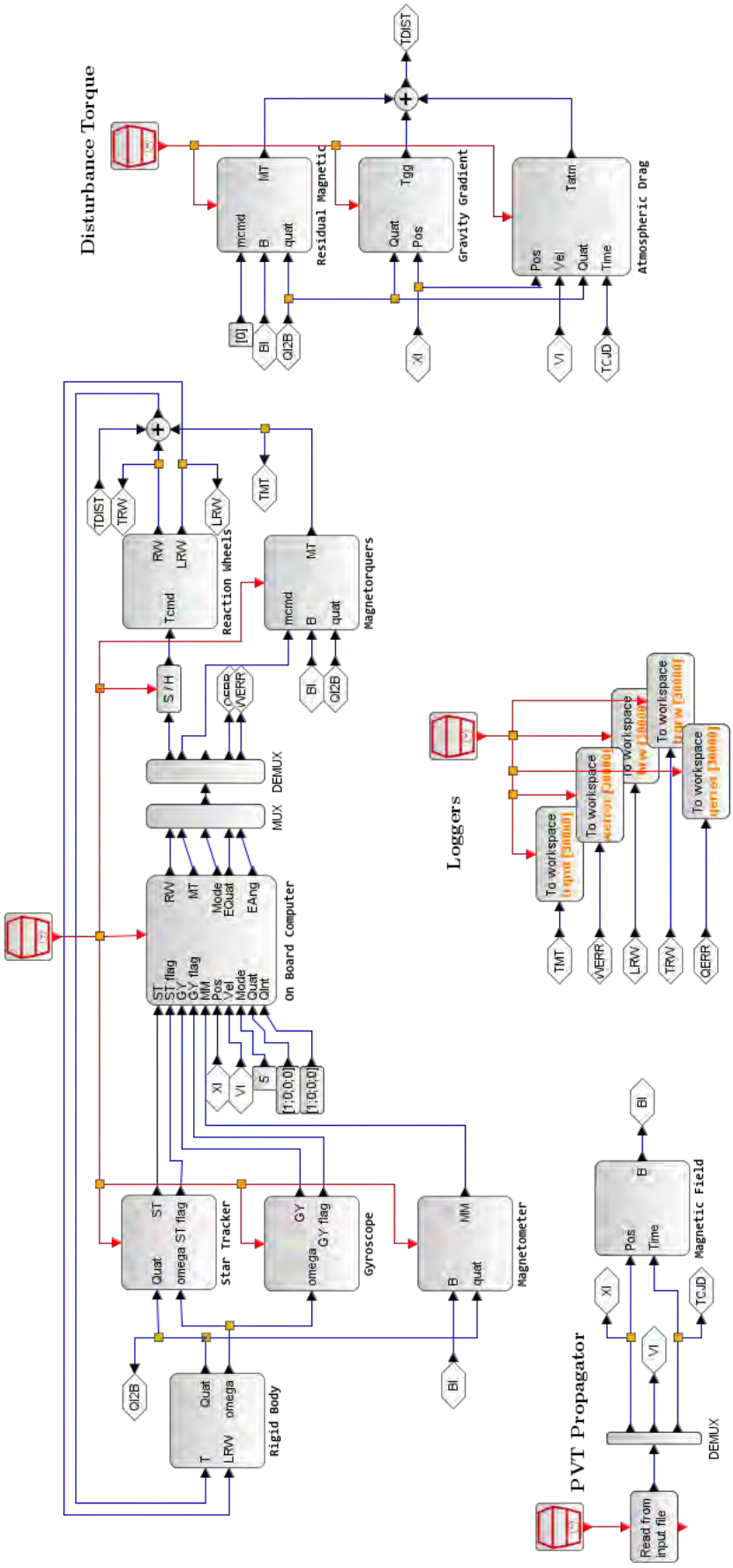

Figure A.12.: De-Tumbling Mode simulation diagram for Cross Product method

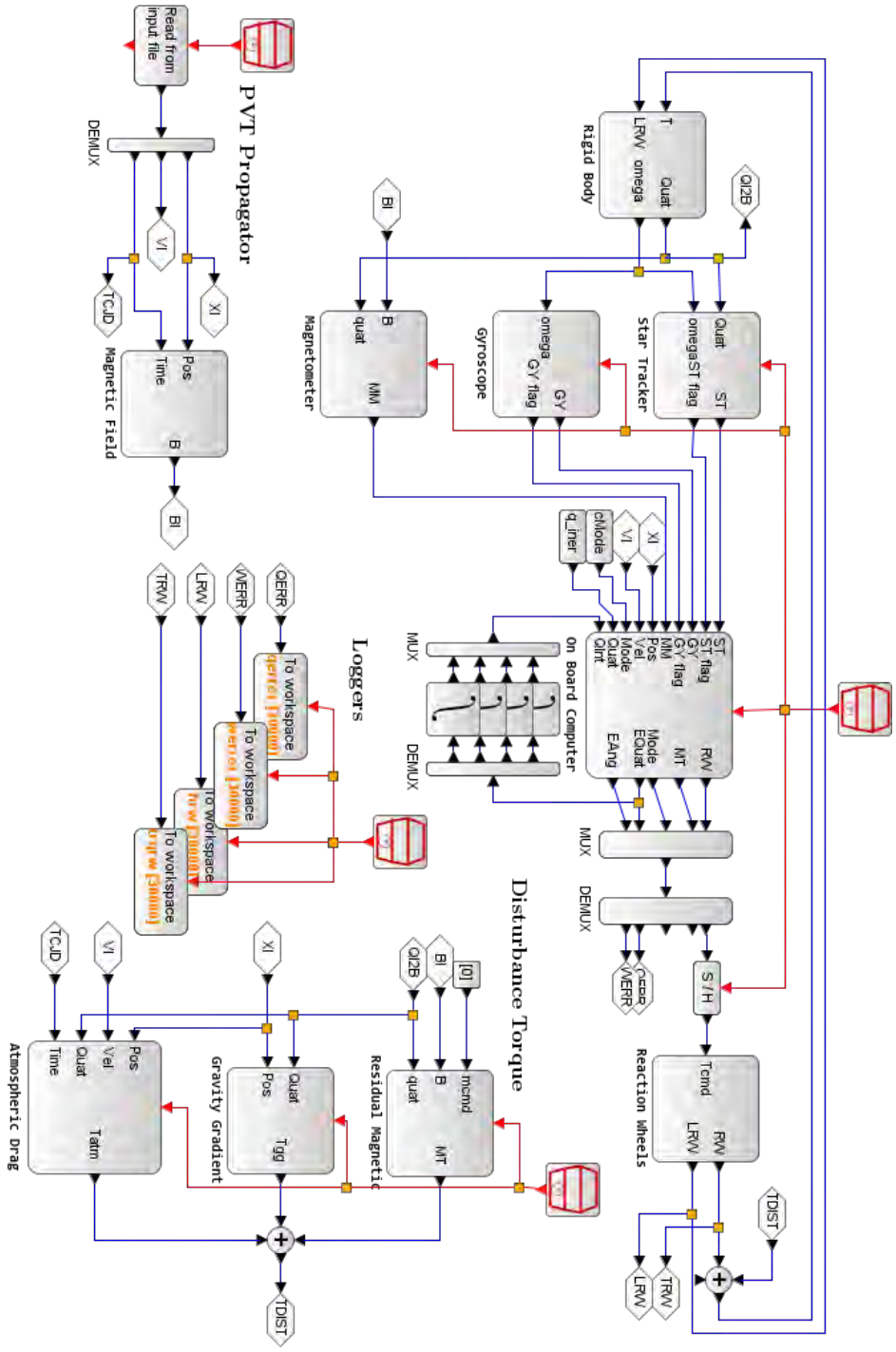

Figure A.13.: Xcos Simulation diagram for SAFE, SCAN, and IPM mode controller tuning and Monte Carlo simulations

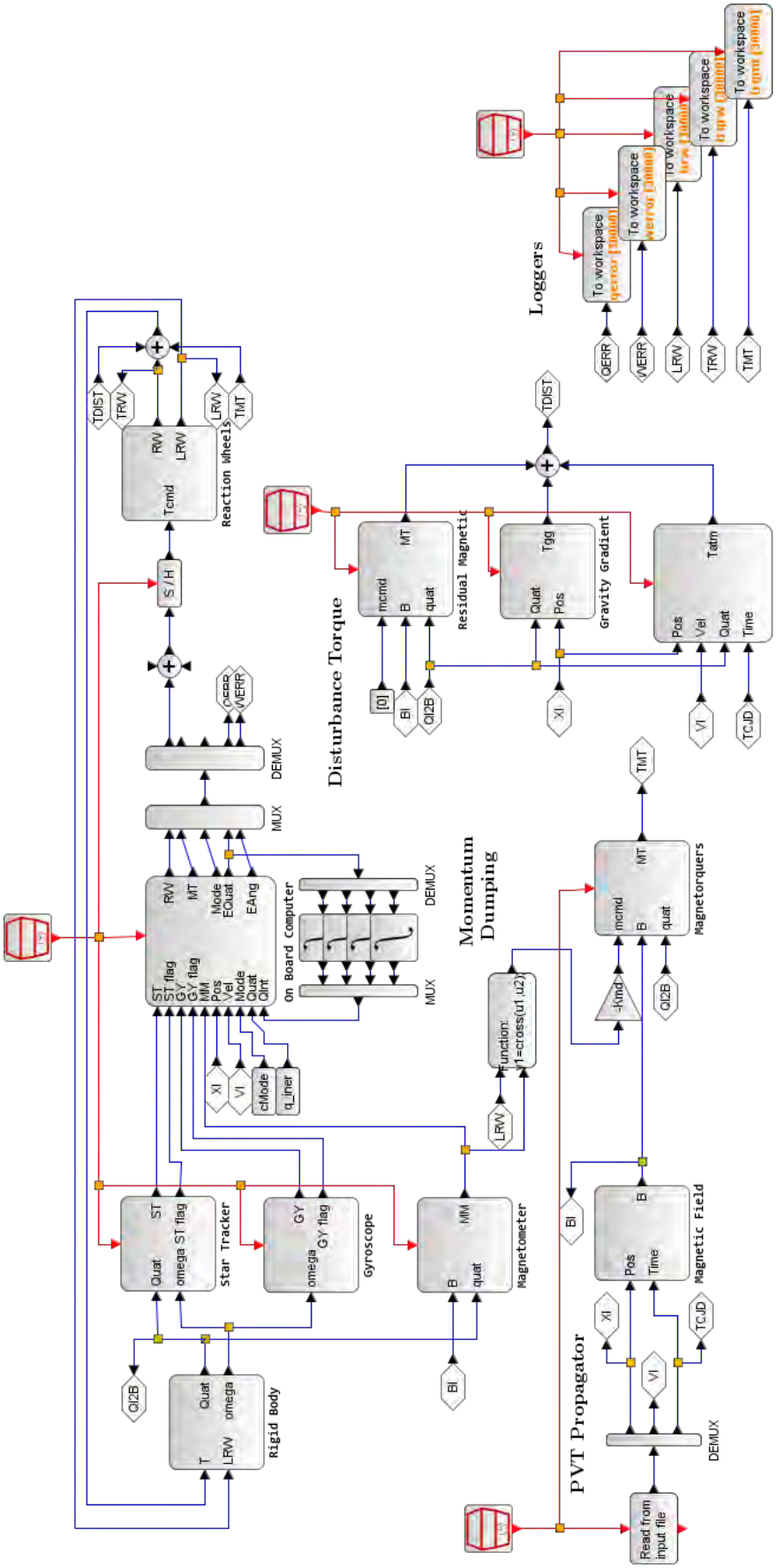

Figure A.14.: Xcos Simulation diagram for reaction wheel momentum dumping through magnetorquers

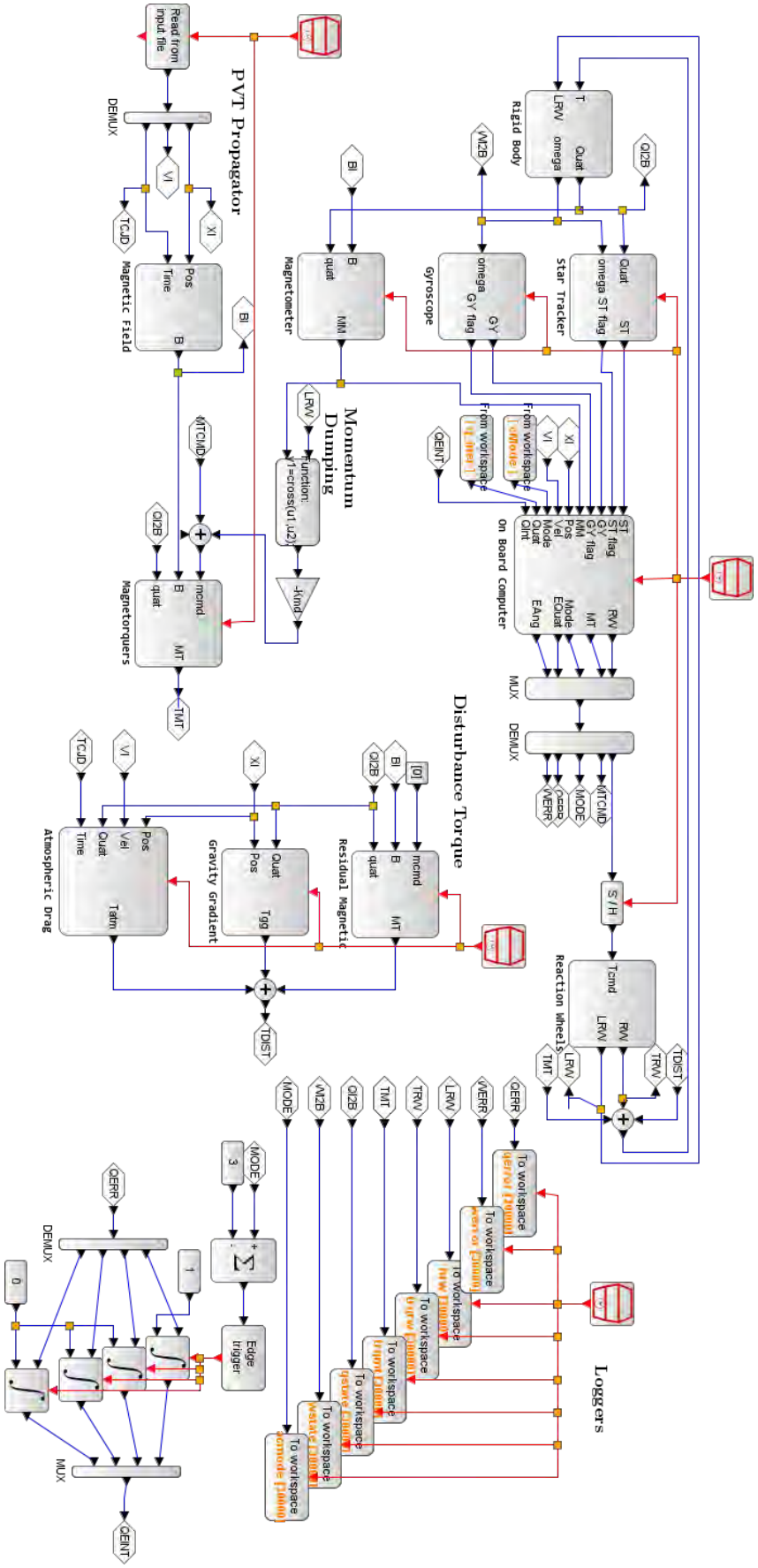

Figure A.15:: Multi mode transition simulation diagram

Bibliography

[1] *The space race*, [Online; accessed 16-January-2024], 2020. [Online]. Available: https://www.history.com/topics/cold-war/space-race (cit. on p. 1).

[2] Q. Zhou, *A shared frontier? collaboration and competition in the space domain*, [Online; accessed 16-January-2024], 2022. [Online]. Available: https://hir.harvard.edu/a-shared-frontier-collaboration-and-competition-in-the-space-domain/ (cit. on p. 1).

[3] *Online index of objects launched into outer space*, [Online; accessed 17-January-2024], 2024. [Online]. Available: https://www.unoosa.org/oosa/osoindex/search-ng.jspx (cit. on p. 1).

[4] C. Moler, *A brief history of matlab*, [Online; accessed 17-January-2024], 2018. [Online]. Available: https://www.mathworks.com/company/technical-articles/a-brief-history-of-matlab.html (cit. on p. 1).

[5] *The 90's, birth of scilab*, [Online; accessed 17-January-2024]. [Online]. Available: https://www.scilab.org/about/company/history (cit. on p. 1).

[6] S. C. Frautschi, R. P. Olenick, T. M. Apostol, and D. L. Goodstein, *The Mechanical Universe: Mechanics and Heat, Advanced Edition*. Cambridge University Press, 1986 (cit. on p. 5).

[7] K. F. Wakker, Ed., *Fundamentals of Astrodynamics*. Institutional Repository Library Delft University of Technology, 2015 (cit. on p. 5).

[8] G. H. Kaplan, *The iau resolutions on astronomical reference systems, time scales, and earth rotation models*, 2006. arXiv: astro-ph/0602086 [astro-ph] (cit. on p. 5).

[9] P. K. Seidelmann and S. E. Urban, "Explanatory Supplement to the Astronomical Almanac, Third Edition," in *American Astronomical Society Meeting Abstracts #215*, ser. American Astronomical Society Meeting Abstracts, vol. 215, Jan. 2010, 475.03, p. 475.03 (cit. on p. 5).

[10] Robert Heinkelmann, *International celestial reference system and frame (icrs/icrf)*, [Online; accessed 04-December-2023], 2019. [Online]. Available: https://www.sirgas.org/fileadmin/docs/GGRF_Wksp/20_Heinkelmann_2019_ICRS-ICRF_overview.pdf (cit. on p. 6).

[11] Contrubitors from NASA NAIF, *Icrf vs j2000*, [Online; accessed 04-December-2023]. [Online]. Available: https://naif.jpl.nasa.gov/pub/naif/toolkit_docs/FORTRAN/index.html (cit. on p. 6).

[12] J. Wertz, Ed., *Spacecraft Attitude Determination and Control*. Dordrecht, The Netherlands: Kluwer Academic Publishers, 1978 (cit. on pp. 6, 7, 10, 11, 22, 27, 32, 38, 66, 73).

[13] H. D. Curtis, *Chapter 4 - Orbits in Three Dimensions*, Third Edition, H. D. Curtis, Ed. Boston: Butterworth-Heinemann, 2014, pp. 189–199, ISBN: 978-0-08-097747-8. DOI: https://doi.org/10.1016/B978-0-08-097747-8.00012-8. [Online]. Available: https://www.sciencedirect.com/science/article/pii/B9780080977478000128 (cit. on p. 8).

[14] H. D. Curtis, *Chapter 12 - Introduction to Orbital Perturbations*, Third Edition, H. D. Curtis, Ed. Boston: Butterworth-Heinemann, 2014, pp. 651–720, ISBN: 978-0-08-097747-8. DOI: https://doi.org/10.1016/B978-0-08-097747-8.00012-8. [Online]. Available: https://www.sciencedirect.com/science/article/pii/B9780080977478000128 (cit. on p. 10).

[15] *Long Term Mean Local Time of the Ascending Node Prediction*, 2007 (cit. on p. 11).

[16] SBG, *Orientation rotations representation*. [Online]. Available: https://support.sbg-systems.com/sc/kb/latest/underlying-maths-conventions/orientation-rotations-representation (cit. on p. 12).

[17] B. Wie, *Space Vehicle Dynamics and Control*, ser. AIAA Education Series. American Institue of Astronautics and Aeronautics, 1998 (cit. on pp. 12, 13, 15, 16, 20, 92, 97).

[18] J. Taylor, *Classical Mechanics*, ser. G - Reference,Information and Interdisciplinary Subjects Series. University Science Books, 2005, ISBN: 9781891389221 (cit. on pp. 13, 14).

[19] K. A. W. Eugene Lavretsky, *Robust and Adaptive Control* (cit. on p. 16).

[20] C. Jaen, J. Pou, R. Pindado, V. Sala, and J. Zaragoza, "A linear-quadratic regulator with integral action applied to pwm dc-dc converters," Dec. 2006, pp. 2280 –2285. DOI: 10.1109/IECON.2006.347726 (cit. on p. 17).

[21] T. Netter, *Scicos: Block diagram modeler/simulator*, 2016. [Online]. Available: http://www.scicos.org (cit. on p. 19).

[22] S. Campbell, J.-P. Chancelier, and R. Nikoukhah, "Modeling and simulation in scilab/scicos," in Springer Science+Business Media Inc., 2006, pp. 196–199, ISBN: 978-0387278025. DOI: 10.1007/978-1-4419-5527-2_3 (cit. on p. 19).

[23] P. C. Hughes, *Spacecraft Attitude Dynamics*. John Wiley and Sons, New York, 1986 (cit. on pp. 19, 22, 25).

[24] J. Meriam and L. Kraige, *Engineering Mechanics: Dynamics*, ser. Engineering Mechanics. Wiley, 2012, ISBN: 9780470614815. [Online]. Available: https://books.google.com.tr/books?id=Lvr61msQz2oC (cit. on p. 19).

[25] I. Pelivan and S. Theil, "Higher accuracy modelling of gravity-gradient induced forces and torques," in *AIAA/AAS Astrodynamics Specialist Conference and Exhibit*. DOI: 10.2514/6.2006-6656. eprint: https://arc.aiaa.org/doi/pdf/10.2514/6.2006-6656. [Online]. Available: https://arc.aiaa.org/doi/abs/10.2514/6.2006-6656 (cit. on p. 23).

[26] F. L. Markley and J. L. Crassidis, *Fundamentals of Spacecraft Attitude Determination and Control*. New York, NY: Springer New York, 2014, ISBN: 978-1-4939-0802-8. DOI: 10.1007/978-1-4939-0802-8_13. [Online]. Available: https://doi.org/10.1007/978-1-4939-0802-8_13 (cit. on pp. 25, 30, 31, 76).

[27] Y. Yang *et al.*, "Comparison of atmospheric mass density models using a new data source: Cosmic satellite ephemerides," *IEEE Aerospace and Electronic Systems Magazine*, vol. 37, no. 2, pp. 6–22, 2022. DOI: 10.1109/MAES.2021.3125101 (cit. on p. 26).

[28] G. Gyatt, *The standard atmosphere*, 2006. [Online]. Available: https://nebula.wsimg.com/ab321c1edd4fa69eaa94b5e8e769b113?AccessKeyId=AF1D67CEBF3A194F66A3&disposition=0 (cit. on p. 26).

[29] *Nrlmsis oo*, [Online; accessed 12-January-2024], Mar. 2023. [Online]. Available: https://ccmc.gsfc.nasa.gov/models/NRLMSIS~00 (cit. on p. 26).

[30] *Scilab help - call*, 2023. [Online]. Available: https://help.scilab.org/call (cit. on p. 26).

[31] P. A. et. al., "International geomagnetic reference field: The thirteenth generation," *Earth, Planets and Space*, vol. 73, no. 49, p. 1, 2021. DOI: 10.1186/s40623-020-01288-x. [Online]. Available: https://doi.org/10.1186/s40623-020-01288-x (cit. on p. 27).

[32] *International geomagnetic reference field*, Dec. 2019. [Online]. Available: https://www.ngdc.noaa.gov/IAGA/vmod/igrf.html (cit. on p. 27).

[33] M. J. Sidi, Ed., *Spacecraft Dynamics and Control, A Practical Engineering Approach*. Cambridge University Press, 1997 (cit. on pp. 29, 33, 34, 37).

[34] J. G. Aboelmagd Noureldin Tashfeen B. Karamat, *Fundamentals of Inertial Navigation, Satellite-based Positioning and their Integration*. Springer Berlin, Heidelberg, 2013, ISBN: 978-3-642-30465-1. DOI: 10.1007/978-3-642-30466-8. [Online]. Available: https://doi.org/10.1007/978-3-642-30466-8 (cit. on p. 31).

[35] P. Brown *et al.*, "Space magnetometer based on an anisotropic magnetoresistive hybrid sensor," *Review of Scientific Instruments*, vol. 85, no. 12, p. 125 117, Dec. 2014, ISSN: 0034-6748. DOI: 10.1063/1.4904702. eprint: https://pubs.aip.org/aip/rsi/article-pdf/doi/10.1063/1.4904702/15742295/125117_1_online.pdf. [Online]. Available: https://doi.org/10.1063/1.4904702 (cit. on p. 32).

[36] J. Lenz and A. Edelstein, "Magnetic sensors and their applications," *Sensors Journal, IEEE*, vol. 6, pp. 631 –649, Jul. 2006. DOI: 10.1109/JSEN.2006.874493 (cit. on p. 33).

[37] H. Unbehauen, *Regelungstechnik I*, ser. Studium Technik. Vieweg+Teubner Verlag Wiesbaden, 2008, pp. 91–92, ISBN: 978-3-8348-0497-6. DOI: https://doi.org/10.1007/978-3-8348-9491-5 (cit. on p. 34).

[38] "Satellite attitude and orbit control system (aocs) requirements," ESA Requirements and Standards Division, Noordwijk, Netherlands, Standard, 2013 (cit. on p. 45).

[39] T. M. Inc. [Online]. Available: https://www.mathworks.com/help/aerobl ks/nrlmsise00atmospheremodel.html (cit. on p. 58).

[40] *Carbonix user manual*, Rev. 2.0, Exolaunch, Sep. 2022 (cit. on p. 62).

[41] *Magnetometers for s/c attitude determination*, Zarm Technik AG, 2009 (cit. on p. 63).

[42] Vectornav, *Educational material - imu specification*. [Online]. Available: https : //www.vectornav.com/resources/inertial-navigation-primer/ specifications--and--error-budgets/specs-imuspecs (cit. on p. 64).

[43] *Crho3 series technical datasheet*, Rev 2.0, Silicon Sensing, 2021 (cit. on p. 64).

[44] *Stim277h datasheet*, Safran Sensing Technologies Norway AS, 2009 (cit. on p. 64).

[45] *Attitude determination st400 star tracker*, AAC Clyde Space, 2021 (cit. on p. 65).

[46] *Reaction wheels datasheet*, Blue Canyon Technologies, 2023 (cit. on p. 68).

[47] *Cubetorquer gen 2 product description*, CubeSpace Satellite Systems, 2023 (cit. on p. 70).

[48] K. Gordon, "A flexible attitude control system for three-axis stabilized nanosatellites," *Institute of Aeronautics and Astronautics: Scientific Series*, vol. 2, p. 107, Jul. 2018. DOI: 10.14279/depositonce-6415 (cit. on p. 77).

[49] Y. Yang, "Spacecraft attitude determination and control: Quaternion based method," *Annual Reviews in Control*, vol. 36, no. 2, pp. 198–219, 2012, ISSN: 1367-5788. DOI: https : //doi.org/10.1016/j.arcontrol.2012.09.003. [Online]. Available: https : //www.sciencedirect.com/science/article/pii/ S1367578812000387 (cit. on p. 80).

[50] A. Bryson and Y. C Ho, *Applied Optimal Control*. Blaisdell Publishing Company, 1969 (cit. on pp. 82, 108).

[51] X. Chen, Y. Hashida, S. Hodgart, and W. Steyn, "Optimal combined reaction-wheel momentum management for earth-pointing satellites," *Journal of Guidance Control and Dynamics*, vol. 22, Jul. 1999. DOI: 10.2514/2.4431 (cit. on p. 101).